Midterm project made at DTU Spring 2004

Simulation, Fabrication and Characterization of Magnetophoretic Microfluid Systems

Anders Ebro Christensen, s001679
Henrik Gert Hassager, s974029
Daniel Evan Nielsen, s001399

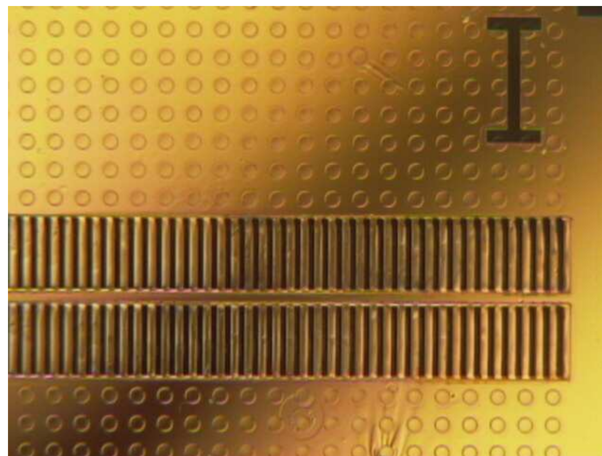

Supervisors: Henrik Bruus, Mikkel Fougt Hansen

MIC – Institute of Micro and Nanotechnology
Technical University of Denmark

June 10, 2004

Contents

1 Introduction **1**
1.1 Basic Design . . . 1

2 Theory **3**
2.1 Magnetizable Element . . . 3
2.2 Magnetizable Sphere . . . 4
2.3 Magnetic Saturation . . . 5
2.4 Fluid Theory . . . 6
2.4.1 Fluids in Motion . . . 6
2.4.2 Reynolds Number . . . 7
2.4.3 Flow between parallel plates . . . 7
2.4.4 Flow through square cross-section . . . 8
2.5 Beads in Fluid . . . 11
2.5.1 Acceleration of Bead . . . 12
2.5.2 Effect of Gravity . . . 13
2.5.3 Percentage of captured beads . . . 14
2.5.4 Trajectories of the beads . . . 15

3 Simulations **17**
3.1 First Model . . . 17
3.1.1 Simulation Setup . . . 17
3.1.2 Measure of Quality . . . 18
3.1.3 Analytical considerations . . . 19
3.1.4 Simulation Results . . . 21
3.1.5 Summary . . . 22
3.2 Second Model . . . 23
3.2.1 Relation between parameters . . . 24
3.2.2 Analytic Estimate . . . 24
3.2.3 Simulation Setup . . . 26
3.2.4 Data Treatment . . . 27
3.2.5 Results . . . 27
3.2.6 Verification of analytic estimate) . . . 28
3.3 Summary . . . 29

4 Experimental work **39**
4.1 Introduction 39

5 The "SU-8 Test Mask" **41**
5.1 Ideas leading to the "SU-8 Test Mask" 41
5.2 Mask design 41
5.2.1 The channel 42
5.2.2 Pull test squares 43
5.2.3 Different size squares 43
5.2.4 Triangles 44
5.2.5 Text 44
5.3 Fabrication 46
5.3.1 Process Sequence 46
5.4 Tests 47
5.5 Batch "SU-8 2002 visual" 47
5.6 Batch "SU-8 2050 Visual" 48
5.7 Batch "SU-8 2002 Pull Test" 50
5.8 Batch "SU-8 2050 Pull Test" 52
5.9 SU-8 tests and their results 52
5.9.1 Pull tests 52
5.9.2 Plasma ash versus 250°C oven 54
5.9.3 Soft-bake 55
5.9.4 Exposure 55
5.9.5 Development 55
5.9.6 Structures 56
5.10 Two layers of SU-8 58
5.11 Summary 59

6 Magnetophoretic Chip Fabrication **61**
6.1 Introduction 61
6.2 Mask Design 61
6.2.1 The chip 61
6.2.2 Teststructures 63
6.3 Process sequence for Magnetophoretic Chip 65
6.4 Process tests and their results 66
6.4.1 Electroplating 66
6.4.2 Hotplate 72
6.4.3 KS aligner 73
6.4.4 Height measurement of SU-8 74
6.5 Summary 75

7 Conclusion **77**
7.1 Theory and Simulation 77
7.2 Fabrication and Process optimization 78

8 Outlook **81**

A Magnetizable Element **83**

B Magnetizable sphere **89**

C Fluid Theory **93**
C.1 Two planes 93
C.1.1 The volume flow 94
C.2 Flow structure through a square cross-section 94

D Cleanroom Processes **97**
D.1 Photo Lithography 97
D.2 Deposition of Metal 99
D.3 SU-8 Processing 100
D.4 Electroplating 100

E Additional test structures on the SU-8 tests mask **103**
E.0.1 Magnetic structures 103
E.0.2 Edge angle testing devices 104

F Detailed process sequense for SU-8 test batches **105**
F.1 First batch of SU-8 2002 for visuel inspection 105
F.2 First batch of SU-8 2050 for visuel inspection 107
F.3 SU-8 2002 Test wafers Pull test 109
F.4 SU-8 2050 Test wafers Pull test 111

G Detailed process sequence for magnetophoretic chips **115**

H Mathematica 5.0 code **119**

List of Figures

1.1 Basic chip design 2

2.1 Element beside fluid channel 4
2.2 Magnetizable sphere in magnetic field 5
2.3 Magnetization curve for soft magnetic materials 6
2.4 The normal vector $\boldsymbol{n}$ to the surface element dA and a given velocity $\boldsymbol{u}$ through the surface element. 7
2.5 A flow between two parallel plates. 8
2.6 The velocity field through a square cross-section. 9
2.7 The velocity field between two parallel planes, solved in MAPLE. 9
2.8 A flow through a square cross section, solved in MAPLE. 10
2.9 The difference between a parabel flow and the square solution 10
2.10 The parabolic flow between two plates (green) and the flow through a square cross-section (red) for $z = \frac{h}{2}$ 11
2.11 The drag force $\boldsymbol{F}_{\mathrm{drag}}$ on a sphere of radius R moving with a relative velocity $\boldsymbol{v}$. 12
2.12 The velocity as a function of time for start velocities different from the equillbrium velocity. 13
2.13 The x and y components. 14
2.14 The percentage of captured beads. 15
2.15 The trajectory of a captured bead. 16

3.1 FEMLAB simulation setup 19
3.2 Setup to test FEMLAB simulations 20
3.3 Magnetic $\boldsymbol{H}$-field outside single magnetized element 21
3.4 Graph of results from FEMLAB simulations 23
3.5 Lineplots of the y-component of the magnetic force in channel from a single element. The figure is not drawn to scale. 25
3.6 Line plots of the y-component of the magnetic force in channel from a single element in the cross-section given in figure 3.5. In (a) at cross-scetion 1, (b) at cross-section 2, (c) at cross-section 3, (d) at cross-section 4, (e) at cross-section 5 and (f) at cross-section 6.The cross sections are shown in figure 3.5. 31

3.7 Different equations for the force from a single is element is plotted. Eq. (3.9) in red, Eq. (3.10) in purple and Eq. (3.11) in blue 32
3.8 The capture point as function of the position for a bead in the symmetric systems. 32
3.9 The capture point as function of the position for a bead in the symmetric systems, a zoom of figure 3.8. 33
3.10 The capture point as function of the position for a bead in the asymmetric systems. 33
3.11 The capture point as function of the position for a bead in the asymmetric systems, a zoom of figure 3.10. 34
3.12 The single and symmetric system for a bar spacing of 550μm. 34
3.13 The percentage captured beads as a function of the channel length for the symmetric systems. 35
3.14 The percentage captured beads as a function of the channel length for the asymmetric systems. 35
3.15 The percentage of captured beads as a function of the channel length for the symmetric 750μm and the asymmetric 450μm systems. 36
3.16 The y-composant of the force in the center of the channel from a single element with a bar width of 50μm and a bar spacing of 750μm. 37
3.17 The percentage of captured beads as a function of the channel length for a single with a bar width of 50μm and a with bar spacing of 750μm found analytically. 37
3.18 The percentage of captured beads as a function of the channel length for a single with a bar width of 50μm and a with bar spacing of 750μm found from the simulations. 38

5.1 Sketch of the original channel design 42
5.2 Sketch of walled channel. Wall thickness 100 μm wall 42
5.3 Sketch of the stress relieved channel. Holes have been made in the massive SU-8 structure to relieve built up stress. 43
5.4 Different size squares 44
5.5 Triangles of different sizes 44
5.6 Mask ID text 45
5.7 Triangle made in SU-8 2002. Sidelength 50 μm 48
5.8 Exposure test of SU-8 2002 49
5.9 Under exposure results in stress cracks everywhere 50
5.10 (A) The wafer has been exposed for 250 s, which closes the holes making elektroplating impossible. (B) This wafer has been exposed for 90 s giving a much better result. 51
5.11 Results of the pull tests of the SU-8 2050 54
5.12 On the left is the rounded 1 cm×1 cm square, on the right a square of the same size but without rounded edges. The right square has suffered adhesion failure 56

5.13 On the left is the original channel, which has suffered massive adhesion failure. The right is the stress relieved channel which has suffered some adhesion failure. The middle is the walled channel which seems to be the best candidate for making the channel and electroplating mould 57
5.14 Smaller squares with sidelength 1000 μm made in SU-8. There is no discerneble effect of rounding the edges. 57
5.15 Corner of rounded square from pull test wafer 2 left side. Notice the slight change in colour in the bottom left corner. 58
5.16 Side of square structure. Top right area: Both layers of SU-8 removed. Top left area: SU-8 2002 remains while SU-8 2050 has been removed. Bottom Area: Both layers of SU-8 remain. Notice how the vertical line seperating the top areas continues below. 59

6.1 The 3 layers in the chip design. The black center line marks where the figure has been squesed to make for a simpler sketch. The real chip is both longer and wider. 62
6.2 Sketch of the stress relieved channel 63
6.3 Thick single bar. The bar has a width of 3000 μm 64
6.4 Thick double bars. The bars have a width of 3000 μm 64
6.5 Test structure to make the electroplating electric field 65
6.6 SEM image of the first electroplating attempt. Note the overflow 67
6.7 X-ray diffraction of the structure shown in 6.6. The elements found are colourcoded 68
6.8 SEM image of electroplating destroying the SU-8. The electroplating actually pushes the SU-8 aside on top of each other. 69
6.9 The succesfull electroplating of the very large single bar test structure . . . 69
6.10 The succesfull electroplating of the very large double bar test structure . . . 70
6.11 Two chips are shown in which the electroplating has blocked the channels. . 70
6.12 A test structure from the same wafer as 6.11. Note that the channel has not been filled by the electroplating, and that the gold is not removed from the channel. 71
6.13 The letter J has been created by making a liftoff of the gold. Note how the SU-8 behaves differently around the letter. 72
6.14 The letter D has been created by making a liftoff of the gold. It is evident that where the gold has been removed there is an increased risk of unwanted electroplating 72
6.15 Hotplate. The darker gray circles marks where and how the wafers were positioned. The red color shows where there was massive adhesion failure. The green crosses shows where the temperature was measured. 73
6.16 KS aligner intensity measurement. The black circles marks the wafer, and the seven red circles mark the measuring points. On the right is shown the intensity measured. The intensity distribution is not uniform over the wafer area. 74

A.1 Magnetizable element beside fluid channel . . . 84
A.2 Cylindrical approximation . . . 85
A.3 Electrostatic analogy . . . 86
A.4 Electrostatic problem . . . 87

B.1 Magnetizable sphere in magnetic field . . . 89

E.1 Part of the electroplating mould structures. . . . 104
E.2 Angle testing devices . . . 104

List of Tables

2.1 Charateristic numbers for M-280 and MyOne bead type from Dynal. 12

3.1 Calculated and simulated $\boldsymbol{H}$-field 22
3.2 Results from FEMLAB simulations 30
3.3 The percentage captured beads for a channel length of $x = 0.05\,\mathrm{m}$. 36

5.1 Exposure times for "SU-8 2002 visual". (2x25 s) means that the exposure was split into two, first exposing for 25 s then waiting 30 s and then exposing 25 s again. 48
5.2 Exposure times for "SU-8 2050 visual" 50
5.3 Exposure times for "SU-8 2002 Pull Test" 51
5.4 Exposure times for "SU-8 2050 Pull Test" 52
5.5 Pull test results for SU-8 2002 53
5.6 Pull test results for SU-8 2050 53

6.1 List of the chips on the mask design 63

D.1 Parameters for the electroplating bath 101

Preface

The work presented in this report describes the work done by Anders Ebro Christensen (s001679), Henrik Gert Hassager (s974029) and Daniel Evan Nielsen (s001399) in a *Polytechnical Midterm Project* (PMP) in the spring semester year 2004 at The Technical University of Denmark (DTU). The project builds upon a three-weeks course done in january 2004 under the title "Microfluidics Theory and Simulation" (course number 33443), also at DTU.

In the three-weeks course the goal was to fabricate and characterize the magnetophoretic microfluidic systems we have worked with in present PMP. However the fabrication of the magnetophoretic microfluidic systems did not succeed in the three-weeks project. As a result the focus of the present PMP has been concentrated heavily upon simulation and fabrication of the magnetophoretic microfluidic systems.

It has proven complicated to work with the polymeric material *SU-8* we use to form the microfluidic systems. The main reason for this is that it is a fairly new technology; the process have not yet been adequately standardized. This means for example that different experts in the field of microprocessing have different – and sometimes conflicting – opinions about the proper treatment of SU-8 and SU-8 processes. Therefore we have needed to optimize alot of processing parameters and design features ourselves.

This has been a great and time-consuming task, which has forced us to make a sharp division of the work needed to be done in this PMP: Anders has worked primarily with the practical design and fabrication of the chips containing our systems. Henrik has worked primarily with the simulation part of the project. Daniel has developed some basic magnetostatic theory and assisted both Anders with the fabrication and Henrik with the simulations.

This PMP report is divided into three main parts: Theory, Simulation and Fabrication. The fabrication part is divided into smaller parts in order to ease its use as a work of reference for other people working in the field of SU-8 processing.

While working with the present PMP we have had a lot of help from researchers and students at DTU. We wish to express our sincere thanks to all the people who have helped us in this project. A special thanks goes to: Assistant Professor at MIC Anders Michael Jørgensen, Associate Professor at IPL Peter Torben Tang, Ph.D. Student at MIC Kristian Smistrup, Ph.D. Student at MIC Alicia Johansson, Ph.D. Student at MIC Maria Nordström, Ph.D. Student at MIC Laurits Højgaard Olesen, Master Student at MIC Torsten Lund Olesen, all the laboratory and process technicians at DANCHIP: Helle Vendelbo Jensen, Yvonne Gyrsting, Majken Becker, Christina Maj Jørgensen, Carsten Svensgaard,

Elena Khomtchenko, Fadil Karamehmedovic and Jonas Michael Jensen. Finally we wish to thank our supervisor and co-supervisor, Henrik Bruus and Mikkel Fougt Hansen.

Chapter 1

Introduction

When dealing with biological samples in liquid form, which often contain a vast amount of different substances (molecules, cells etc), it is of big importance to be able to isolate certain substances from the sample. This separation can be done in various ways. One way of separating a substance from a sample in liquid form is to tag the substance with a magnetic material and, by applying a magnet, capturing the substance. There exists commercially available magnetizable micro beads (small magnetizable spheres with diameter of a couple of micrometer). These can be coated with functional chemicals binding specifically to a certain substance, so by coating them and applying them to a sample, they will bind to that certain substance. If the sample is flowing in a fluid channel, then by placing magnets by the side walls of the channel, the substance taged with the magnetic micro beads can now be captured at the channel walls.

This principle is to be investigated in our project; using microfluid channels and magnetic structures placed at the side walls of these channels. Such a setup is called a *magnetophoretic microfluidic system*.

Utilizing micro-systems for this purpose imply several advantages; one is being able to analyze smaller samples than is needed in ordinary laboratory analysis. Using microfluid channels this way is also a step towards the concept of *lab-on-a-chip systems*, where various analytical systems are integrated on a single small chip, which supposedly eases the handling and reduces the cost of both production and use.

1.1 Basic Design

The microfluidic system consists of a fluid channel built in the polymeric material SU-8. Along the sides of this channel are situated structures of a soft magnetic material, a nickel-iron alloy, called Permalloy. See figure 1.1.

The basic idea is that by applying an external homogeneous magnetic field (which does not have to be very strong) over the system, the magnetic structures become strongly magnetized, creating a strongly inhomogeneous magnetic field. This way it should be possible to capture magnetic beads from the fluid flowing in the channel. According to classical electromagnetic theory the force, $\boldsymbol{F}$, exerted by a magnetic field, $\boldsymbol{B}$, on a magnetic

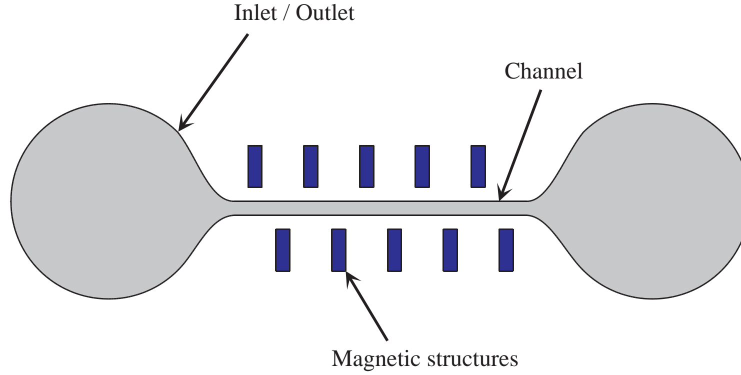

Figure 1.1: Simple sketch of the microfluidic system, not drawn to scale: In each end of a thin channel is a large inlet/outlet. Along the channel is placed magnetizable structures.

dipole, $\boldsymbol{m}$, is given by

$$\boldsymbol{F} = (\boldsymbol{m} \cdot \nabla)\boldsymbol{B} \tag{1.1}$$

This equation shows that a homogeneous magnetic field can not exert any force on a magnetic dipole, so an inhomogeneous field is indeed required.

The magnetic structures along the channels are made of a soft magnetic material; we aim to come as close to "Permalloy" as we can. Permalloy is one of the softest ferromagnetic material that can be produced. Permalloy consists of nickel and iron in the proportions Ni:Fe = 80:20 mass percent.

That a ferromagnetic material is soft means in layman terms that it is easy to magnetize by applying an external magnetic field, and that when the external field is removed, the material will lose its magnetization and have almost no residual magnetization. It is important for us to use soft magnetic structures because we want to be able to control the magnetizable structures on the chip as precisely as possible. In other words, we want to be able to 'turn them on and off' as we see fit.

Figure 1.1 shows a simple sketch of the system. We investigate how the magnetic structures should be placed in respect to each other, and what dimensions they should have, in order to yield the optimum capturing capability.

Chapter 2

Theory

In this chapter we derive and explain the basic theory of magnetostatics and fluid dynamics that will be the foundation of the simulations of the magnetophoretic microfluidic systems we will examine in this report.

We will first go through some very simple magnetostatic theory needed to understand how the magnetizable elements along the fluid channels will behave when subjected to an external homogeneous magnetic field. Then we will investigate how a magnetizable sphere will behave in an external magnetic field; what force will be exerted on it by the field. We conclude the magnetostatic theory with a brief explanation of *magnetic saturation*.

In the following only some important results about the behaviour of the magnetizable elements and the magnetizable sphere will be stated. To see the full derivation of these results we refer to the appendices A and B.

Next we derive some fluid theory. It will be investigated how fluids behave in motion. Two different geometries are examined: Fluid flowing between parallel planes, and fluid flowing through a square cross section.

Then we will introduce beads (tiny spherical balls) to the fluid and we will investigate how these beads behave in the fluid.

2.1 Magnetizable Element

In this section we briefly state an approximated expression for the size of the magnetic field, $\boldsymbol{H}_{\text{tot}}$, outside a magnetizable element placed in an external homogeneous magnetic field, $\boldsymbol{H}_{\text{ext}}$. The full derivation is done in appendix A. The situation is shown in figure 2.1, where we also have indicated the fluid channel. The x-axis is parallel to the direction of the fluid flow in the channel, the y-axis is parallel to the external homogeneous magnetic field, $\boldsymbol{H}_{\text{ext}}$, and perpendicular to the channel walls. The origo is placed on the center of the top surface of the element.

By approximating the element with a cylinder of the same length, L_{el}, and the same cross sectional area as the real element, A_{el}, and by using the concept of *magnetic charges*, an approximate solution to the problem can be found by using an analogy with electrostatic theory. All in all the size of the magnetic field on the y-axis, $H_{\text{tot}}(y)$, outside the element

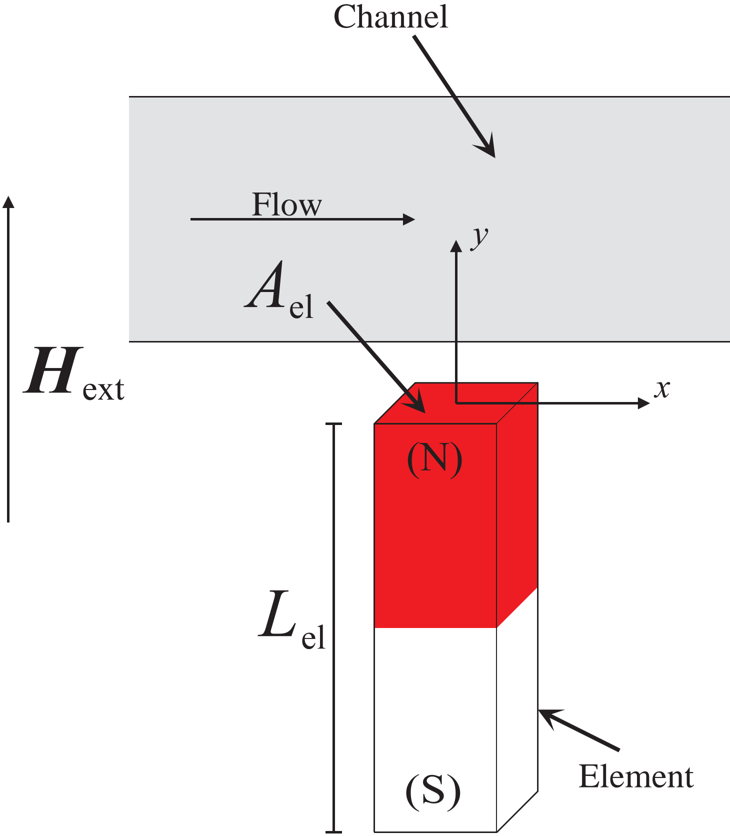

Figure 2.1: Sketch of a magnetizable element with length L_{el} and cross sectional area A_{el}. The element is situated beside the fluid channel and is magnetized by an external homogeneous magnetic field, $\boldsymbol{H}_{\text{ext}}$. The element behaves as a bar magnet.

is given by

$$H_{\text{tot}}(y) = H_{\text{ext}}\left[1 + \frac{A_{\text{el}}\chi_{\text{el}}}{4\pi(1 + N_{\text{cyl}}\chi_{\text{el}})}\left(\frac{1}{y^2} - \frac{1}{(y + L_{\text{el}})^2}\right)\right]. \tag{2.1}$$

Here χ_{el} is the *magnetic susceptibility* of the material the element is made of and N_{cyl} is the *demagnetization factor* for the cylinder.

2.2 Magnetizable Sphere

In this section we briefly state the expression for the force exerted by an external magnetic field on a magnetizable sphere. For the full derivation we refer to appendix B. The situation is sketched in figure 2.2. In this figure $\boldsymbol{H}_{\text{d}}$ is the *demagnetization field*, the effect of which is to reduce the internal $\boldsymbol{H}$-field inside the sphere.

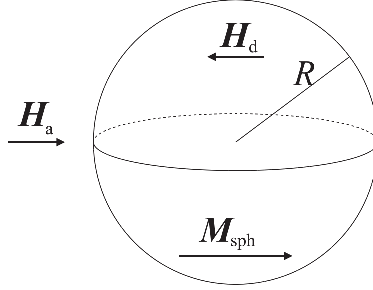

Figure 2.2: Sketch of a magnetizable sphere placed in an external magnetic field.

The force, $\boldsymbol{F}_{\mathrm{sph}}$, exerted on the sphere by the externally applied magnetic field, $\boldsymbol{H}_{\mathrm{a}}$, is given by:

$$\begin{aligned}\boldsymbol{F}_{\mathrm{sph}} &= 2\pi\mu_0 R^3 \frac{\chi_{\mathrm{sph}}}{\chi_{\mathrm{sph}}+3}\boldsymbol{\nabla} \mid \boldsymbol{H}_{\mathrm{a}} \mid^2 && (2.2)\\ &= 4\pi\mu_0 R^3 \frac{\chi_{\mathrm{sph}}}{\chi_{\mathrm{sph}}+3}\boldsymbol{H}_{\mathrm{a}} \cdot \boldsymbol{\nabla}\boldsymbol{H}_{\mathrm{a}} && (2.3)\\ &= 4\pi\mu_0 R^3 \frac{\chi_{\mathrm{sph}}}{\chi_{\mathrm{sph}}+3}\begin{pmatrix} V_{\mathrm{m}x}V_{\mathrm{m}xx} + V_{\mathrm{m}y}V_{\mathrm{m}yx} \\ V_{\mathrm{m}x}V_{\mathrm{m}xy} + V_{\mathrm{m}y}V_{\mathrm{m}yy}\end{pmatrix}, && (2.4)\end{aligned}$$

where R is the radius of the sphere, χ_{sph} is the magnetic susceptibility of the material the sphere is made of, μ_0 is the permeability of free space, $\boldsymbol{H}_{\mathrm{a}} = -\boldsymbol{\nabla} V_{\mathrm{m}} = -\binom{V_{\mathrm{m}x}}{V_{\mathrm{m}y}}$ where V_{m} is the *magnetic scalar potential* and $\frac{\partial}{\partial x}V_{\mathrm{m}x}$ is denoted by $V_{\mathrm{m}xx}$ and so forth.

Equation (2.4) is valid in two dimensions.

2.3 Magnetic Saturation

In the previous sections, it has been assumed that the magnetizable materials behave linearly, so that the magnetization of the materials are the product of the auxiliary field, $\boldsymbol{H}$, inside the material and the magnetic susceptibility, χ, of the material:

$$\boldsymbol{M} = \chi \boldsymbol{H} \quad (2.5)$$

In real materials, there exists a limit to how big an internal $\boldsymbol{H}$-field they can sustain and still be linear. This is shown in the *magnetization curve* in figure 2.3.

A soft magnetic material behaves linearly for sufficiently low $\boldsymbol{H}$-fields. For those low fields the slope of the magnetization curve is the magnetic susceptibility χ. For higher $\boldsymbol{H}$-fields in the material, the magnetization converges towards the *saturation magnetization*, M_{s}. To ensure that a material behaves linearly in a certain situation, one must ensure that the internal $\boldsymbol{H}$-field, $\boldsymbol{H}_{\mathrm{i}}$, satisfy the following:

$$M_{\mathrm{s}} \geq \chi H_{\mathrm{i}} \quad (2.6)$$

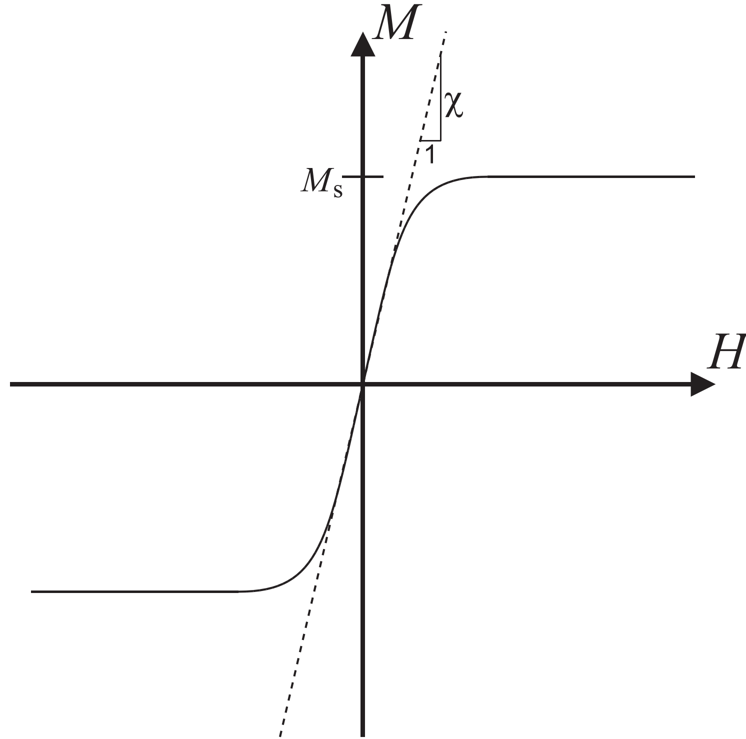

Figure 2.3: Sketch of the *magnetization curve* for a soft magnetic material. The material behaves linearly for sufficiently low $\boldsymbol{H}$-fields; here the slope is the magnetic susceptibility χ. For increasing $\boldsymbol{H}$-field the magnetization converges to the *saturation magnetization* M_s.

2.4 Fluid Theory

In this section we introduce the fluid mechanics we have used and describe the phenomena concerning beads in a fluid.

2.4.1 Fluids in Motion

The motion of a Newtonian fluid[1] is described by the Navier-Stokes equation,

$$\rho\left(\frac{\partial}{\partial t} + (\boldsymbol{u}\cdot\boldsymbol{\nabla})\right)\boldsymbol{u} = -\boldsymbol{\nabla}p + \eta\nabla^2\boldsymbol{u} + \boldsymbol{f}, \tag{2.7}$$

together with the continuity equation,

$$\frac{\partial\rho}{\partial t} = -\boldsymbol{\nabla}\cdot(\rho\boldsymbol{u}), \tag{2.8}$$

[1]Fluids with a linar relationship between stress and velocity gradients.

where ρ is the density of the fluid, η is the viscosity of the fluid, p is the pressure, and $\boldsymbol{f}$ is a body force. For an incompressible fluid ρ is constant, so $\boldsymbol{\nabla} \cdot \boldsymbol{u} = 0$.

The volume flow Q through a cross-section is given in skalar form as

$$Q = \int_A \boldsymbol{n} \cdot \boldsymbol{u} \, \mathrm{d}A, \tag{2.9}$$

see figure 2.4. For pressure driven flows there exists an analogy to Ohm's law for eletric

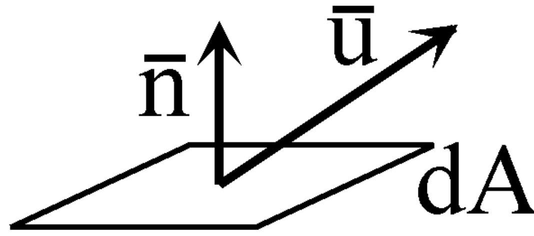

Figure 2.4: The normal vector $\boldsymbol{n}$ to the surface element $\mathrm{d}A$ and a given velocity $\boldsymbol{u}$ through the surface element.

circuits given as:

$$\Delta p = R_{\mathrm{hyd}} \, Q, \tag{2.10}$$

where R_{hyd} is defined as the *hydraulic resistance*.

2.4.2 Reynolds Number

To determine whether a flow is dominated by inertia or viscosity, the *Reynolds number* has been defined as the ratio between the advective term $\rho(\boldsymbol{v} \cdot \boldsymbol{\nabla})\boldsymbol{v}$ and the viscous term $\eta \nabla^2 \boldsymbol{v}$ in Navier-Stokes equation. As a rough estimate we set $|\boldsymbol{v}| \approx U$, $|\boldsymbol{\nabla} \boldsymbol{v}| \approx \frac{U}{L}$ and $|\nabla^2 \boldsymbol{v}| \approx \frac{U}{L^2}$ where U is a characteristic velocity and L the shortest distance of velocity changes,

$$Re = \frac{\rho U L}{\eta}. \tag{2.11}$$

For micro fluidic systems normally $Re \ll 1$ and the flow is then laminar.

2.4.3 Flow between parallel plates

If we have a stationary flow between two parallel plates in the xy-plane positioned at $z = 0$ and $z = h$, as shown in figure 2.5, the velocity field is $\boldsymbol{u} = (u(z), 0, 0)$ with

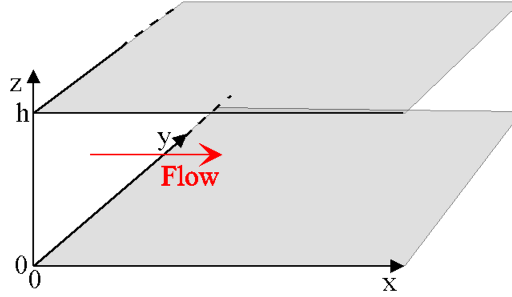

Figure 2.5: A flow between two parallel plates.

$$u(z) = \frac{1}{2}\frac{\Delta p}{\eta L} z(h-z), \tag{2.12}$$

and the corresponding volume flow is given by

$$Q = \frac{1}{12}\frac{\Delta p}{\eta L} wh^3 \tag{2.13}$$

where w is the width of the plates. The full derivation is done in appendix C.

We see that the hydraulic resistance is,

$$R_{\text{hyd}} = \frac{12L\eta}{wh^3}. \tag{2.14}$$

If we assume no-slip conditions on all of the planes, this model is a good approximation as long as $h \ll w$. When the ratio, $\frac{w}{h}$, becomes less than 10, it is no longer reasonable to assume a parallel plates flow.

2.4.4 Flow through square cross-section

The velocity profile through a square cross-section, as two plates in the xy-plane at $z = 0$ and $z = h$ and two plates in the xz-plane at $y = 0$ and $y = w$, see figure (2.6), can be found as:

$$u(y,z) = \frac{\Delta p}{\eta L}\frac{16}{\pi^4} \sum_{\text{odd } n}^{\infty} \sum_{\text{odd } m}^{\infty} \frac{1}{nm\left(\frac{n^2}{h^2} + \frac{m^2}{w^2}\right)} \sin\left(n\pi\frac{y}{h}\right) \sin\left(m\pi\frac{z}{w}\right) \tag{2.15}$$

where h is the height, w is the width and L is the length of the channel. The dereviation is done in appendix C. This solution can be solved numerical and the corresponding volume flow can be found. The velocity fields in equation (2.12) and equation (2.15) are for a ratio of $\frac{w}{h} = 2$ shown in figure 2.7 and 2.8 respectively.

The difference between the two normed velocity fields are shown in figure 2.9. In the cross-section for $z = \frac{w}{2}$ the two profiles are identical, but near the ends there is a large

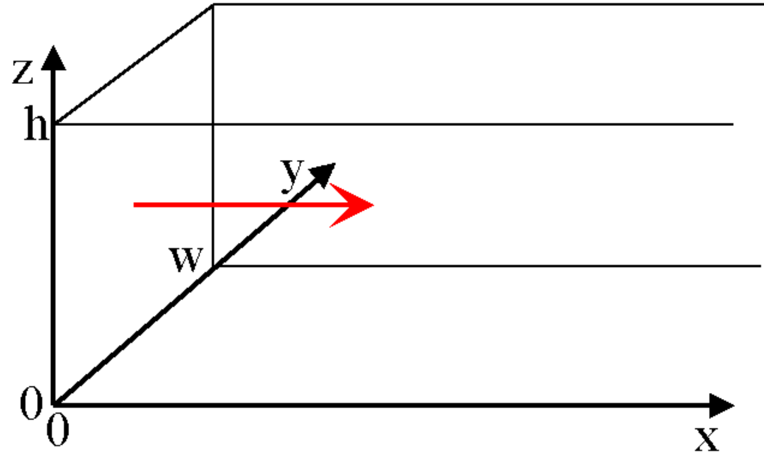

Figure 2.6: The velocity field through a square cross-section.

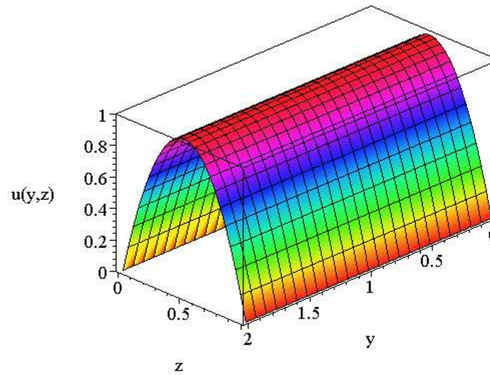

Figure 2.7: The velocity field between two parallel planes, solved in MAPLE.

difference. Therefore we need a correction of the hydraulic resistance $R_{\mathrm{hyd,c}}$. Making a series expansion of the velocity field in equation (2.15), and comparing this volume flow with the volume flow for two parallel plates will give us[2],

$$R_{\mathrm{hyd,c}} = \frac{12L\eta}{(w-0.63\,h)h^3}. \tag{2.16}$$

In our work we want to express the velocity as a function of the volume flow since it is a parameter we can control. From equation (2.12), (2.13) and (2.16) we get

$$u(z) = 6\frac{Q}{(w-0.63\,h)\,h^3}z(h-z). \tag{2.17}$$

[2]This formula was given by our supervisor Henrik Bruus

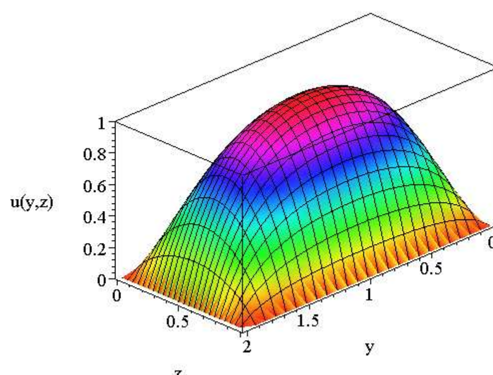

Figure 2.8: A flow through a square cross section, solved in MAPLE.

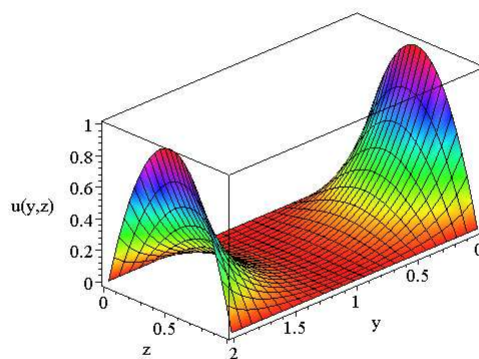

Figure 2.9: The difference between a parabel flow and the square solution

This is a good expression for the velocity field in the xz-plane at $y = \frac{w}{2}$.

In the case where we need an analytic expression for the velocity field in the xy-plane, our approximation of the velocity field as a parabolic flow between two plates will be even more inaccurate. The parabolic flow between two plates and the flow through a square cross-section for $z = \frac{h}{2}$ are shown in figure 2.10. We can see that there is a difference in the velocities, but since our magnetic elements are placed in the y-direction we will use this as an approximation for the velocity in the xy-plane. If we change the varible $z \rightarrow y$ and the boundary $h \rightarrow w$ in equation (2.12)

$$u(y) = \frac{1}{2} \frac{\Delta p}{\eta L} y(w - y) \tag{2.18}$$

and insert the corrected volume flow from equation (2.13) and (2.16) then $u(y)$ is

$$u(y) = 6 \frac{Q}{(w - 0.63\, h)\, h^3} y(w - y). \tag{2.19}$$

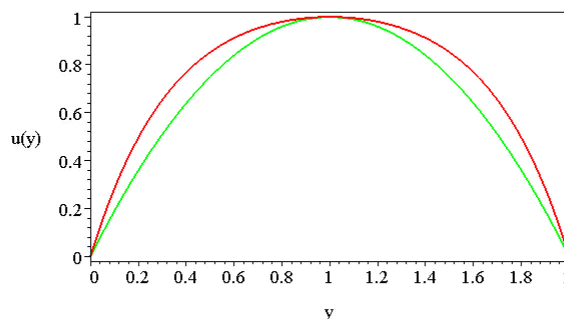

Figure 2.10: The parabolic flow between two plates (green) and the flow through a square cross-section (red) for $z = \frac{h}{2}$

As an estimate $u(y)$ might be in the same order of magnitude since the velocity at $z = \frac{h}{2}$ will dominate.

2.5 Beads in Fluid

There are various forces that affect beads in a fluid, e.g. a magnetic force F_{mag} due to the fact that the beads are magnetic dipole in an inhomogeneous field the gravitational force F_{g} and other forces including electrostatic interaction between the beads and the wall.

All these forces results in a viscous contact force F_{v} from the motion of the bead in the fluid. The total force can be split up into two components; *lift* and *drag*. The lift force acts orthogonal to the flow and the drag force acts in the direction of the flow.

The lift force is difficult to describe because it depends on many factors (e.g. the shape of the body, whether it is able to rotate or if it is surrounded by other elements). These phenomena are in pipe flows mentioned as *particle migration* in textbooks and papers, but models are still unfinshed, therefore we choose not to include these in our models.

The drag force is instead calculated as for a sphere in a laminar flow described by Stokes [5]. See figure 2.11.

The drag force is given as:

$$\boldsymbol{F}_{\mathrm{drag}} = -6\,\pi\,\eta\,R\,\boldsymbol{v} \tag{2.20}$$

where R is the radius of the sphere and $\boldsymbol{v}$ is the relative velocity between the bead and the fluid, so $\boldsymbol{v} = \boldsymbol{v}_{\mathrm{bead}} - \boldsymbol{v}_{\mathrm{fluid}}$. Stokes drag force is only valid for a laminar flow.

From now on we assume that water is the fluid in our system and that the bead used is MyOne from the Norwegian company Dynal, when we do calculations. The density and

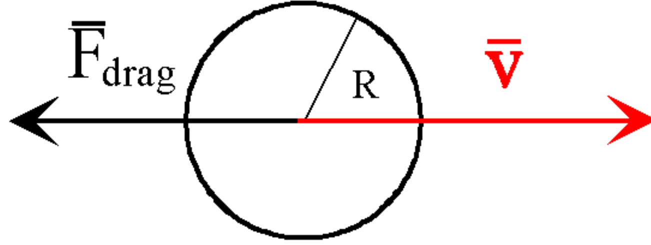

Figure 2.11: The drag force $\boldsymbol{F}_{\text{drag}}$ on a sphere of radius R moving with a relative velocity $\boldsymbol{v}$.

viscosity for water at 300K are

$$\rho_{\text{water}} \simeq 10^3 \frac{\text{kg}}{\text{m}^3} \quad \text{and} \quad \eta_{\text{water}} \simeq 10^{-3} \text{Pa s}. \tag{2.21}$$

The charateristic numbers for two bead types by Dynal [6] page 42 are shown in tabel 2.1. The dimensions of our channel in our microchip are $w = 100\mu\text{m}$ and $h = 50\mu\text{m}$

	M-280	**MyOne**
Radius (R) [μm]	1.4 $\pm$ 0.1	0.525 $\pm$0.05
Density (ρ) [$\frac{\text{kg}}{\text{m}^3}$]	1300	1800
Magnetic susceptibility (χ) [No unit]	0.13$\pm$0.3	1.49 $\pm$ 0.12

Table 2.1: Charateristic numbers for M-280 and MyOne bead type from Dynal.

2.5.1 Acceleration of Bead

If the bead, while in the fluid, is affected by external forces (e.g. gravity or magnetic force) a equlibrium velocity is reached almost instantaneously. We wish to calculate how fast. According to Newton's second law:

$$m\dot{\boldsymbol{v}} = -6\pi\eta R\boldsymbol{v} + \boldsymbol{F}_{\text{extern}} \tag{2.22}$$

The solution to this equation is

$$\boldsymbol{v} = \frac{\boldsymbol{F}_{\text{extern}}}{6\pi\eta R} + \boldsymbol{C} \exp\left(-\frac{6\pi\eta R}{m}t\right) \tag{2.23}$$

where $\boldsymbol{C} = \boldsymbol{v}(\text{t=0}) - \frac{\boldsymbol{F}_{\text{extern}}}{6\pi\eta R}$, $m = \frac{4}{3}\pi R^3(\rho_{\text{bead}} - \rho_{\text{fluid}})$ and the 'relaxation-time-constant' $\tau = \frac{m}{6\pi\eta R}$. The velocity as a function of time for start velocities different from $\boldsymbol{v}_{eq}$ is shown in figure (2.12). We can calculate the 'relaxation-time' τ for our system

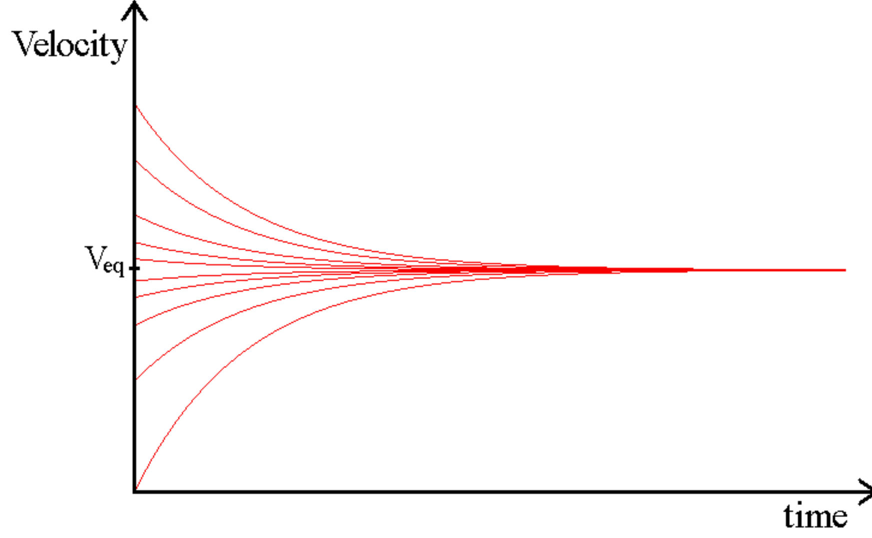

Figure 2.12: The velocity as a function of time for start velocities different from the equillbrium velocity.

$$\tau = \frac{\frac{4}{3}\pi R^3(\rho_{\text{bead}} - \rho_{\text{fluid}})}{6\pi\eta R} = \frac{2R^2(\rho_{\text{bead}} - \rho_{\text{fluid}})}{9\eta} \approx 5.0 \times 10^{-8}\text{s} \tag{2.24}$$

We then see that it is reasonable to assume that the beads at all time have the equilibrium velocity $\boldsymbol{v}_{\text{eq}}$ relative to the fluid velocity:

$$\boldsymbol{v}_{\text{eq}} = \frac{F_{\text{extern}}}{6\pi\eta R} \tag{2.25}$$

The velocity of the bead is then $\boldsymbol{v}_{\text{bead}} = \boldsymbol{v}_{\text{fluid}} + \boldsymbol{v}_{\text{eq}}$.

2.5.2 Effect of Gravity

Since we do not wish gravity to affect the outcome and stability of our chip, we wish to design it so gravity is negligible. The beads velocity v_{g} given from the gravitational force is

$$v_{\text{g}} = \frac{\frac{4}{3}\pi R^3(\rho_{\text{bead}} - \rho_{\text{liquid}})g}{6\pi\eta R} = \frac{2}{9}\frac{R^2(\rho_{\text{bead}} - \rho_{\text{liquid}})g}{\eta} \tag{2.26}$$

Δh is the distance the bead moves in z-direction caused by gravity in the time Δt and Δl is the distance the bead moves in the x-direction caused by the flow in the time Δt,

$$\Delta h = v_{\text{g}}\Delta t \quad \text{and} \quad \Delta l = v_{\text{fluid}}\Delta t = \frac{Q}{A}\Delta t \tag{2.27}$$

where A is the cross section of the channel. This is shown in figure 2.13 We can assume

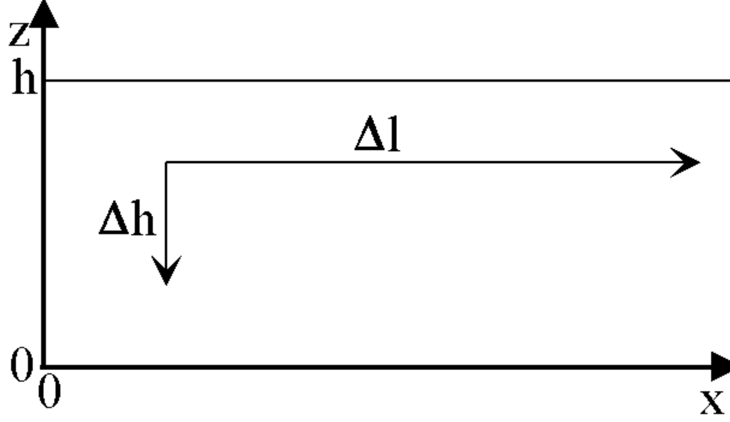

Figure 2.13: The x and y components.

the gravity to be negligible if

$$\frac{\Delta h}{h} < 0.01 \tag{2.28}$$

We then get

$$Q > 100 \frac{v_{\mathrm{g}} A \Delta l}{h} = 100 \frac{2}{9} \frac{R^2 A \Delta l (\rho_{\mathrm{bead}} - \rho_{\mathrm{liquid}}) g}{\eta h} \tag{2.29}$$

If our system is 10 cm long, $\Delta l = 0.1\mathrm{m}$, then Q must be greater than $1.7 \times 10^{-9} \frac{\mathrm{m}^3}{\mathrm{s}}$. The pressure required for this volume flow is

$$\Delta p = R_{hyd,c} Q = \frac{12 \Delta l \eta}{(w - 0.63\, h) h^3} Q \approx 23.8\mathrm{k\,Pa} \tag{2.30}$$

This is a pressure which we are able to deliver in our experiments.

The Reynolds number for this volume flow is

$$Re = \frac{\rho U L}{\eta} = \frac{\rho Q L}{A \eta} = \frac{1000 \frac{\mathrm{kg}}{\mathrm{m}^3}\, 1.7 \times 10^{-9} \frac{\mathrm{m}^3}{\mathrm{s}}\, 25 \times 10^{-6}\mathrm{m}}{50 \times 10^{-6}\mathrm{m}\, 100 \times 10^{-6}\mathrm{m}\, \times 10^{-3}\mathrm{Pas}} = 8.5 \tag{2.31}$$

this Re is not smaller than 1 but the flow is still assumed to be laminar.

2.5.3 Percentage of captured beads

The percentage of captured beads in two dimensions in the xy-plane is per definition given as

$$P_{\mathrm{beads}} = \frac{\int_0^{y_0} u(y)\, \mathrm{d}y}{\int_0^{w} u(y)\, \mathrm{d}y} \tag{2.32}$$

where P_{beads} denotes the percentage of captured beads, $u(y)$ is the velocity profile, and y_0 is the level from $y = 0$ to $y = w$ where we capture the beads. See figure 2.14

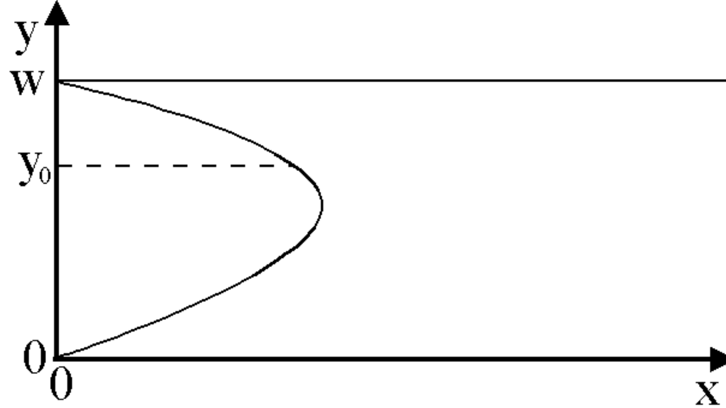

Figure 2.14: The percentage of captured beads.

2.5.4 Trajectories of the beads

To find the trajectories of the beads we use the x and y components for the velocity of the beads and the magnetic force on the beads

$$\frac{\mathrm{d}x}{\mathrm{d}t} = u(y) \quad \text{and} \quad \frac{\mathrm{d}y}{\mathrm{d}t} = \frac{F_{\text{mag}}(x,y)}{6\pi\eta R} \tag{2.33}$$

so to describe the beads

$$\frac{\mathrm{d}x}{\mathrm{d}y} = 6\pi\eta R \frac{u(y)}{F_{\text{mag}}(x,y)} \tag{2.34}$$

The trajectory of a bead is shown in figure 2.15.

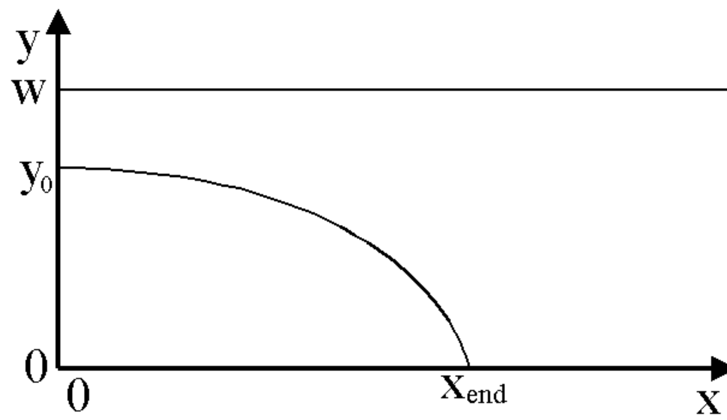

Figure 2.15: The trajectory of a captured bead.

Chapter 3

Simulations

In this chapter, we build two different models of the magnetophoretic microfluidic systems in two dimensions, and simulate different setups.

We start with a simple model, and simulate different designs of the system by varying the width of the magnetizable elements, the spacing between them and the positioning of the elements beside the fluid channel. In this model we only include the magnetic forces in the systems. From the results of these simulations, we decide which designs we wish to fabricate and test experimentally.

In the second model we furthermore include magnetizable beads and fluidic effects. This model is assumed to be close to reality and therefore comparable to real physical experiments.

3.1 First Model

We want to investigate different designs for the magnetophoretic microfluidic systems. We have decided to use only rectangular shaped magnetic structures[1] in the designs. We want to investigate how the size, interspacing and placement of the structures influence the design. To compare different designs we need a *measure of quality*. Many such measures can be defined and we will define a quality measure later in this section. Using this measure in the simulations we decide which designs are best and would be most promising to concentrate our attention on.

For the simulations, we use the program package *FEMLAB* which can be accessed via a graphical user interface, that makes it possible to easily simulate various setups in both two and three dimensions.

3.1.1 Simulation Setup

In our simulations, we only work in two dimensions because simulating in three dimensions is a *very* time-consuming task. When working in two dimensions instead of three dimen-

[1] The structures we consider are all long compared to their widths and heights in order to reduce demagnetization effects.

sions, there is translation in the third direction. It is very important that we take this fact into consideration when judging the result of the simulations. We rely on a measure of quality, but we know that this is only a simple measure for the two dimensional problem and that the real problem is three dimensional and much more complicated.

We investigate three different ways of placing the elements:

- *Double sided* design with magnetic elements on both sides of the channel.
  - *Symmetric*, where the structures are situated exactly opposite each other.
  - *Asymmetric*, where the structures are displaced to the greatest extend in respect to each other.
- *Single sided* design with magnetic elements only on one side of the channel.

In the simulations we vary the width of the magnetic elements (called the *bar width*) and the interspacing between the magnetic elements (called the *bar spacing*).

The setups used to carry out the simulations are sketched in figure 3.1. We use symmetric boundary conditions on the left and right boundaries in each case. In this way, we are in principle simulating infinitely long channels, which are made up of repetitions of the small pieces shown in the sketch in figure 3.1. We have in each case a fixed constant width of the channel of 96 μm. The magnetic elements have a fixed constant length of 505 μm in all the simulations. The distance from a bar to the side of the channel has a constant value of 2 μm in all the simulations. Furthermore the area we define in FEMLAB in which to carry out the simulation has the width of the bar-spacings, and is kept at a constant total length of 4 mm.

The simulations are made via FEMLAB's built-in linear magnetic model, where we have defined the external magnetic field, $\boldsymbol{H}_{\mathrm{ext}}$, to be perpendicular to the top- and bottom boundaries of the simulation-area as shown in figure 3.1.

3.1.2 Measure of Quality

As mentioned we need a measure of quality, a mode of comparison, in order to distinguish between the different designs and determine which of the designs are best.

Although this model does not include the small magnetic beads used to tag the target substance and also does not include any fluid effects, we know that these will be present in reality. Therefore we consider the effects when trying to find a good measure of quality.

The force that a magnetic bead experiences in the channel is what captures the bead. The faster the bead is captured, the higher the quality of the design. The bead is captured by being dragged out to the side walls of the channel, so the total magnetic force that the bead feels perpendicular to the channel side walls must be included in the quality measure. The fluid that in reality will be present in the channel will drag the magnetic bead along the channel, so a good measure could also include the forces exerted on the bead by the magnetic field in the channel antiparallel to the fluid flow direction.

The force exerted on a magnetizable bead by a magnetic field is given by equations (2.2) through (2.4)

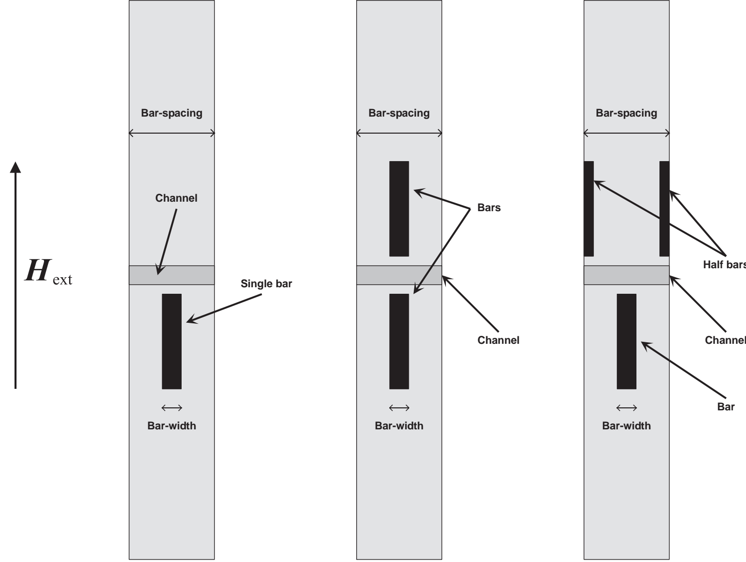

Figure 3.1: Sketch of the setups used to simulate the single sided, double sided symmetric and double sided asymmetric channel designs respectively. The left and right boundaries in each case are symmetric, so that the channel designs, which we simulate are in principle repeated infinitely many times. In the figure is also indicated the external magnetic field, $\boldsymbol{H}_{\text{ext}}$, which we use in all the simulations. The figures are not drawn to scale.

For now we decide to include only the force perpendicular to the channel walls in our measure of quality. The measure of quality, Q_{M1}, is defined as follows:

$$Q_{\text{M1}} = \frac{1}{A}\int_{\text{channel}} |F_{\text{sph,y}}|\,\mathrm{d}S \tag{3.1}$$

$$= \frac{1}{A}\int_{\text{channel}} \left|4\pi\mu_0 R^3 \frac{\chi_{\text{sph}}}{\chi_{\text{sph}}+3}\left[V_{\text{m}x}V_{\text{m}xy} + V_{\text{m}y}V_{\text{m}yy}\right]\right|\mathrm{d}S, \tag{3.2}$$

where $F_{\text{sph,y}}$ is the y-composant of the force from equation (2.4). $R = 5.25\times10^{-7}$ m is the radius of the beads, $\mu_0 = 4\pi\times10^{-7}\ \mathrm{N\,A^{-2}} = 1.26\times10^{-6}\ \mathrm{N\,A^{-2}}$, $\chi_{\text{sph}} = 1.49$. The variable V_{m} is the magnetic scalar potential (which is also the variable we solve for in the simulation). A is the area over which we integrate.

3.1.3 Analytical considerations

Before we start the simulation process of the different designs, we want to be sure that FEMLAB delivers the results we are interested in. We make a simple simulation of just one magnetizable element and measure the $\boldsymbol{H}$-field outside this element at some points along the symmetry axis of the element which is indicated in figure 3.2.

The value of the $\boldsymbol{H}$-field outside the magnetized element is found in the FEMLAB simulation via a cross-section line plot along the symmetry axis of the element. This plot

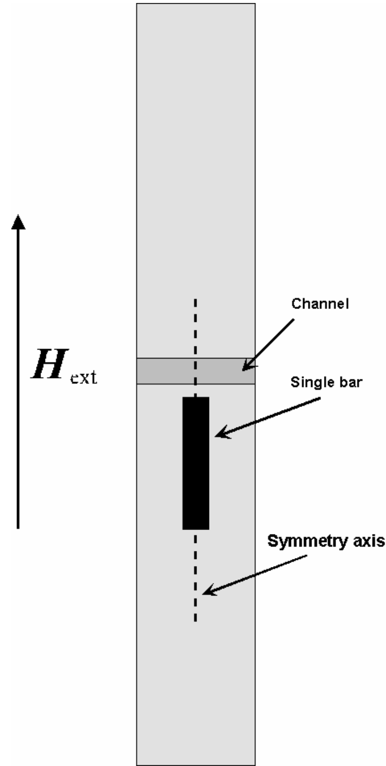

Figure 3.2: Sketch of the setup used to simulate a single magnetizable element. An external homogeneous magnetic field, $\boldsymbol{H}_{\text{ext}}$, is applied parallel to the symmetry axis. The value of the $\boldsymbol{H}$-field outside the element is measured on the symmetry axis via FEMLAB and compared with approximated analytical results. The figure is not drawn to scale.

is seen in figure 3.3.

For a few points along the symmetry axis of the magnetized element, we calculate the expected field from equation (2.1). Here we insert the numbers $H_{\text{ext}} = \frac{1\text{mT}}{\mu_0}$, $A_{\text{el}} = 50\,\mu\text{m} \times 50\,\mu\text{m}$, $\chi_{\text{el}} = 1000$ and $L_{\text{el}} = 500\,\mu\text{m}$. The value of the demagnetization factor N_{cyl} is given in [4], table 2.1 page 41. We see that the ratio between the length of the cylinder, with which we approximate the element, to the diameter of the approximated cylinder is about 10, and for this value, the table gives the demagnetization factor $N_{\text{cyl}} = 0.0172$.

For the same points along the symmetry axis, we read off the value of the magnetic $\boldsymbol{H}$-field from the FEMLAB simulation cross-sectional plot. The calculated values and the simulated values are listed in table 3.1.

From table 3.1 we see that the calculated values do not agree with the simulation results for small distances. However for greater distances there seems to be increasing and quite good agreement between the calculated and the simulated results. This disagreement is due to the rough estimates made to form the analytical expression in equation (2.1); it also only applies for great distances. Therefore we expect huge disagreements for small

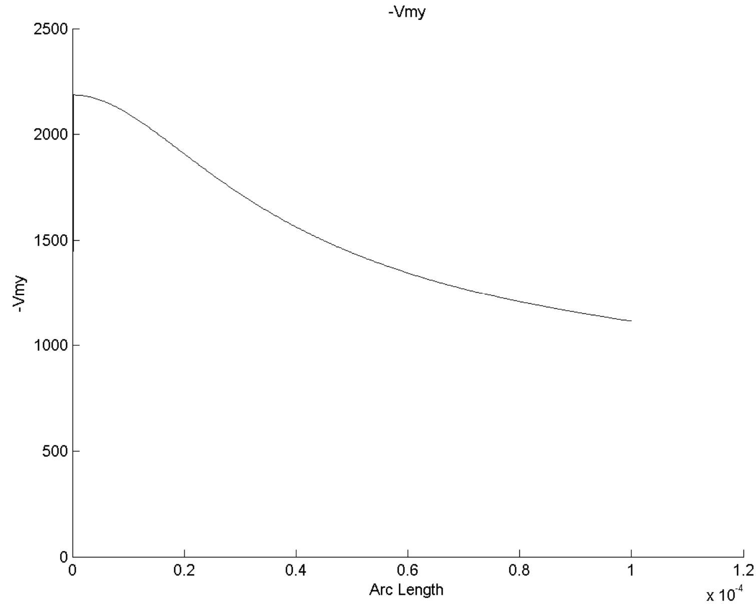

Figure 3.3: Graph from FEMLAB of the total magnetic $\boldsymbol{H}$-field outside a single magnetized element. The graph is made as a *cross-sectional plot* in FEMLAB. The cross section is taken from the middle of the element top at the coordinates $(0, 0)$ to $100\,\mu$m straight upwards from the element top through the channel (perpendicular to the channel walls). The y-axis is the y-composant of the total $\boldsymbol{H}$-field in the units $\left[\frac{\mathrm{A}}{\mathrm{m}}\right]$. The x-axis is the distance from the top of the element; the unit of the x-axis is [m].

distances from the element, as is also seen in the comparison in table 3.1.

All in all we believe that the simulations in FEMLAB are realistic under the assumptions made. We are now ready to carry out the simulations of different system designs.

3.1.4 Simulation Results

The results of the simulations are given in table 3.2. From FEMLAB we do not get the quality Q_{M1} directly. FEMLAB returns the size of the integral in equation (3.2), that is FEMLAB returns $Q_{\mathrm{M1}} \times A$. To obtain the quality Q_{M1} we find the area A from knowledge about the width of the channel and the length of the piece of channel that is integrated over (this length is equal to the bar spacing). By simple division we obtain the quality Q_{M1}.

The results from table 3.2 are plottet in figure 3.4.

From this graph we see that for a given design (double sided symmetric, double sided asymmetric or single sided) and for a given element-interspacing, the elements with width $50\,\mu$m perform better than the elements with greater widths. Therefore we choose to concentrate our futute work on designs with element-width of $50\,\mu$m.

Distance [μm]	10	30	50	80
Calculated $\boldsymbol{H}$-field $\left[\frac{\text{A}}{\text{m}}\right]$	87748	10429	4246	2129
Simulated $\boldsymbol{H}$-field $\left[\frac{\text{A}}{\text{m}}\right]$	2080	1720	1440	1200

Table 3.1: The value of the calculated total $\boldsymbol{H}$-field and the simulated $\boldsymbol{H}$-field outside a single magnetized element. The simulated values are read off of a graph from FEMLAB why there exists some uncertainty for these values; about $20\,\frac{\text{A}}{\text{m}}$.

3.1.5 Summary

We have investigated different magnetophoretic microfluidic system designs. The spacing between the magnetizable elements and the width of the elements were varied. We found that elements $50\,\mu$m wide performed better than wider elements for a given design and a given element-interspacing.

From these results we decide which element-widths and element-interspacings we want to use in our wafer design and fabrication. We decide to use only elements that are $50\,\mu$m wide. The wafer on which the magnetophoretic microfluidic systems are to be fabricated, has room for ten chips. For reasons to be discussed in section 6.2 we want to include only five different designs on the wafer (we want a duplicate of each design on the wafer). We want to be able to compare the performance of the different designs via experiments, so we need to choose designs that have some properties in common. We choose to include the following designs:

- Double sided symmetric, element-width $50\,\mu$m, element-interspacing $150\,\mu$m.
- Double sided symmetric, element-width $50\,\mu$m, element-interspacing $300\,\mu$m.
- Double sided symmetric, element-width $50\,\mu$m, element-interspacing $600\,\mu$m.
- Double sided asymmetric, element-width $50\,\mu$m, element-interspacing $600\,\mu$m.
- Single sided, element-width $50\,\mu$m, element-interspacing $300\,\mu$m.

We choose to concentrate on the double sided symmetric designs although the simulation results suggest that the double sided asymmetric designs might be better. Our primary concern is that the asymmetric designs might have a tendency to force the beads to oscilate from side to side through the channel instead of capturing the beads at the channel walls.

With this selection of designs we should be able to see a tendency in capturing efficiency (of the double sided symmetric designs) as the elements come closer together and converge towards a single large element. We should also be able to compare the asymmetric design with the symmetric design by using the designs with element-interspacing $600\,\mu$m. Finally we should be able to compare the single sided design with both the double sided symmetric and the double sided asymmetric design, because the single sided design contains the same

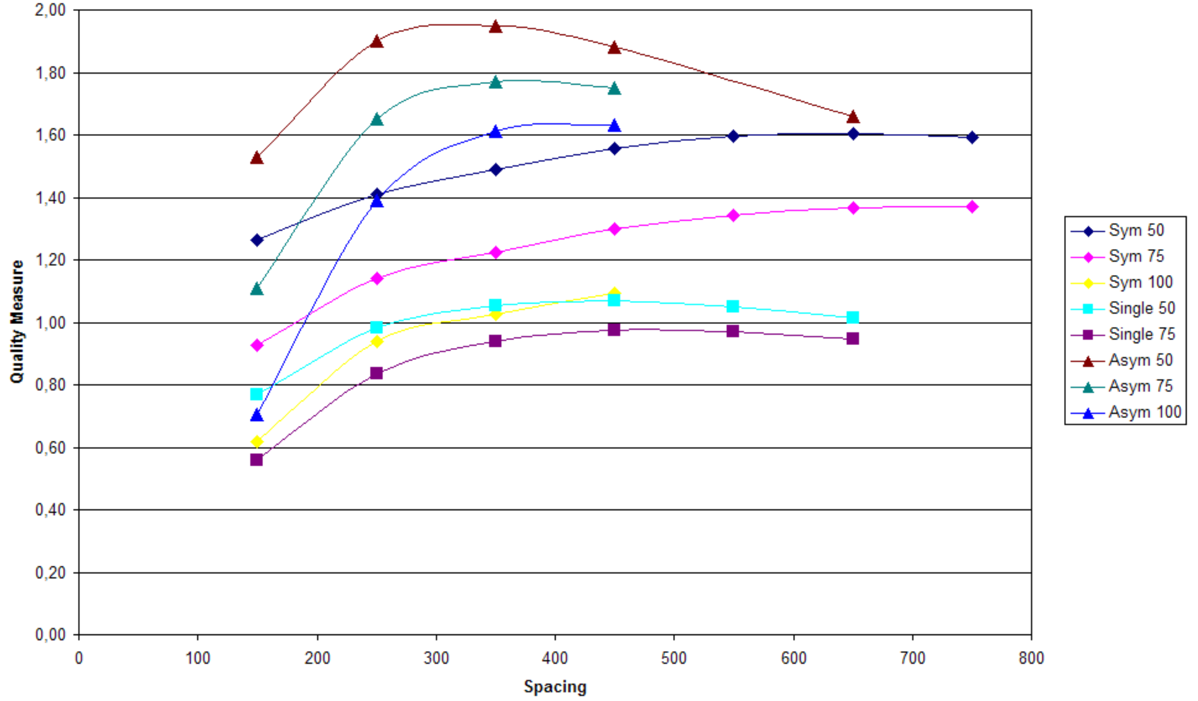

Figure 3.4: Graph made in Microsoft Excel from some of the simulation results. The graph shows the quality measure Q_{M1} as a function of the spacing between the elements. The unit of the y-axis is 10^{-14} N. The unit of the x-axis is $1\,\mu$m.

number of elements per channel length of as the asymmetric and the symmetric with element-interspacing $600\,\mu$m.

3.2 Second Model

Since the aim of our magnetophoretic microfluidic system is to capture cells with magnetizable beads in a flow, a model where such beads and a flow are included is the next step in refining our model. The magnetic field in the channel from different element configurations have already been modelled, so now only the fluid theory have to be added to make a model that describes the trajectories of the beads in the channel. There are many ways in which to describe the effectiveness of the systems. In our work we have chosen to describe the percentage of captured beads as a function of the length of the channel, the external $\boldsymbol{H}$-field and the volume flow. First we make an analytic estimate to describe how the length of the channel, the external $\boldsymbol{H}$-field and the volume flow are connected. Secondly we make a more describing expression for the percentage of beads captured. We can then determine which of the magnetic structures has the best capture percentage and

if the results agree with the first model. In all estimates and simulations will we use the bead type MyOne.

3.2.1 Relation between parameters

In this analytic estimate we only include the magnetic force and the viscous force, since we assume that we can capture beads unaffected by gravity. We wish to describe the percentage of beads captured as a function of the channel length, the volume flow and the external $\boldsymbol{H}$-field, since these are all parameters we can control. As a rough estimate we see from equation (2.32) and (2.34) that

$$P_{\text{beads}} \propto y_0 \quad \text{and} \quad y_0 \propto \frac{F_{\text{mag}}}{F_{\text{v}}} x_{\text{end}} \tag{3.3}$$

where x_{end} is the length of the channel. The percentage of captured beads are proportional to the ratio of the magnetic force and the viscous force times the length of the channel.

$$P_{\text{beads}} \propto \frac{F_{\text{mag}}}{F_{\text{v}}} x_{\text{end}} = \frac{4\pi\mu_0 R^3 \frac{\chi}{\chi+3} H \nabla H}{6\pi\eta R \frac{Q}{A}} x_{\text{end}} \tag{3.4}$$

where the force on a bead for a magnetic field is given in equation 2.3. We known that if the elements have reached magnetic saturation, ∇H is constant, for A, bar spacing and bar width. So for same geometric system ∇H is constant. This gives us

$$P_{\text{beads}} \propto \frac{R^2 \chi H}{\eta(\chi+3)Q} x_{\text{end}} \tag{3.5}$$

We have now described the percentage of captured beads as a function only of the channel length and the volume flow, but the $\boldsymbol{H}$-field is given as the contribution from the external $\boldsymbol{H}$-field and the $\boldsymbol{H}$-field from the elements. It will be very complicated to isolate the two $\boldsymbol{H}$-fields from each other. But what we are able to conclude is that the ratio $\frac{\chi R^2}{(\chi+3)}$ from equation (3.5) shall be high to contribute to the percentage of captured beads.

Instead of finding the percentage of captured beads as a function of the external H-field we will give it as a function of the force acting on the bead.

3.2.2 Analytic Estimate

To get an analytic expression for the percentage of captured beads in equation (2.32) we insert the velocity field from equation (2.19).

$$P_{\text{beads}} = \frac{\int_0^{y_0} y(w-y)\,\mathrm{d}y}{\int_0^{w} y(w-y)\,\mathrm{d}y} = \frac{y_0^2}{w^2}\left(3 - 2\frac{y_0}{w}\right) \tag{3.6}$$

This is only an order of magnitude estimate. To determine the bead's start position y_0 in the channel as a function of the end position x_{end} at the channel wall, we must integrate

equation (2.34) with respect to x and y and then solve for y_0, this can be done if we assume that the velocity u and the magnetic force $F_{\rm mag}$ only depend on y.

$$\frac{\mathrm{d}x}{\mathrm{d}y} = 6\pi\eta R \frac{u(y)}{F_{\rm mag}(y)} \tag{3.7}$$

For the velocity $u(y)$ we use equation (2.19). In equation (2.1) we found that the magnetic $\boldsymbol{H}$-field is inversely proportional to the distance squared and from equation (2.3) we can see that the magnetic force can be approximated to

$$F_{\rm mag}(y) \propto -\frac{1}{y^5} \tag{3.8}$$

In section 3.1 we found that this is only valid far from the element. So in FEMLAB we make lineplots of the y-component of the magnetic force in channel from a single element, shown in figure 3.5. The line plots are shown is figure 3.6. If we only consider the line

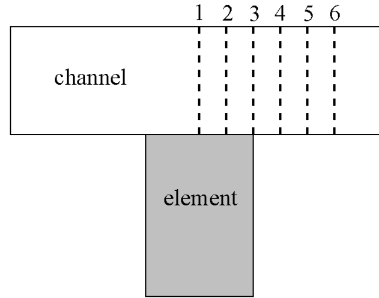

Figure 3.5: Lineplots of the y-component of the magnetic force in channel from a single element. The figure is not drawn to scale.

plots for cross-section 1, 2, 3 and 4 since these are dominating. It seems that the average of the magnetic force can be estimated to be inversely proportional to d^x where $x \in [1, 2]$. We choose the distance squared. Our first intuition of an expression for the magnetic force will be

$$F_{\rm mag}(y) = -\frac{1}{4} F_{\rm mag,c} \frac{w^2}{y^2} \tag{3.9}$$

where $F_{\rm mag,c}$ is the numerical size of the magnetic force in the center of the channel. It is easy to solve the integration of equation (3.7), but it will be very difficult to solve for $\frac{y_0}{w}$. Therefore we must find another function for the magnetic force that decreases with the distance squared. Two functions that behave like that, and can give us an expresion for y_0, are

$$F_{\rm mag}(y) = -\frac{1}{4} F_{\rm mag,c} \left(\frac{w\,y - w^2}{y^2} \right) \tag{3.10}$$

$$F_{\rm mag}(y) = -\frac{1}{2} F_{\rm mag,c} \left(\frac{w\,y - w^2}{y^2} \right) \tag{3.11}$$

In both of these functions $F_{\mathrm{mag,c}}$ is the numerical size of the magnetic force in the center of the channel from equation (3.9). Equation (3.9), (3.10) and (3.11) are shown in figure 3.7, for $F_{\mathrm{mag,c}} = 1\mathrm{N}$, in red, purple and blue respectively. Equation (3.10) has the same asymtodic behavier for $y \to 0^+$ as equation (3.9) where equation (3.11) has the same size of the force in the center of the channel as equation (3.9). It could be suggested that we use equation (3.10) since it similar asymtodic behavier and then the large forces near the channel are the same, but since it is the size of the force in the center of the flow that determines whether the beads will be captured or not we use equation (3.11). When we assume the flow to be the velocity field given in equation (2.19). We get equation (3.7) to

$$\frac{\mathrm{d}x}{\mathrm{d}y} = 6\pi\eta R \frac{u(y)}{F_{\mathrm{mag}}(y)} = 6\pi\eta R 6 \frac{Q}{(w-0.63\,h)\,h^3} \frac{2}{F_{\mathrm{mag,c}} w} \frac{y\,(w-y)}{\left(\frac{y-w}{y^2}\right)} \tag{3.12}$$

If we integrate from the start position of the bead in the channel $(0, y_0)$ to the end position of the bead $(x_{\mathrm{end}}, 0)$, see figure 2.15, we get

$$\int_0^{x_{\mathrm{end}}} \mathrm{d}x = 72\pi \frac{\eta\, R}{w(w-0.63\,h)h^3} \frac{Q}{F_{\mathrm{mag,c}}} \int_{y_0}^{0} \frac{y\,(w-y)}{\left(\frac{y-w}{y^2}\right)} \mathrm{d}y \tag{3.13}$$

$$= 72\pi \frac{\eta\, R}{w(w-0.63\,h)h^3} \frac{Q}{F_{\mathrm{mag,c}}} \left[-y^3\right]_{y_0}^{0} \tag{3.14}$$

$$x_{\mathrm{end}} = 18\pi \frac{\eta\, R}{w(w-0.63\,h)h^3} \frac{Q}{F_{\mathrm{mag,c}}} y_0^4 \tag{3.15}$$

From equation (3.15) we isolate $\frac{y_0}{w}$

$$\frac{y_0}{w} = \left(\frac{h^3(w-0.63\,h)}{18\pi\eta R w^3} \frac{F_{\mathrm{mag,c}}}{Q} x_{\mathrm{end}}\right)^{\frac{1}{4}} \tag{3.16}$$

and insert $\frac{y_0}{w}$ in equation (3.6). This gives us an analytic expression for the percentage of the captured beads as a function of the channel length.

$$P_{beads} = \left(\frac{h^3(w-0.63\,h)}{18\pi\eta R w^3} \frac{F_{\mathrm{mag,c}}}{Q} x_{\mathrm{end}}\right)^{\frac{1}{2}} \left(3 - 2\left(\frac{h^3(w-0.63\,h)}{18\pi\eta R w^3} \frac{F_{\mathrm{mag,c}}}{Q} x_{\mathrm{end}}\right)^{\frac{1}{4}}\right) \tag{3.17}$$

We can see that the percentage of captured beads depends linear of the ratio of the magnetic force in the center of the channel over the volume flow.

We are aware that we have made alot of rought approximations to reach this analytic description of the percentage of the captured beads, why equation (3.17) only is an order of magnitude solution.

3.2.3 Simulation Setup

The simulations for the second model are made in Matematica 5.0. To determine the trajectories of the beads we need the magnetic force field and the velocity field. The

magnetic force field was found from equation (2.4) for the bead type MyOne where the magnetic scalar potential is found in the FEMLAB simulations. The force field for a single section is then repeated to make a channel of continuum of elements. Since the $\boldsymbol{H}$-field simulations are in two dimensions, we only make the bead flow simulations in two dimensions since the gravity acts perpendicular to the capture direction, it is then natural to omit the gravity. So the model is only correct if the gravity can be neglected. The velocity field is found numerically for equation (2.15) for $z = \frac{h}{2}$. The volume flow we have used is $Q = 10^{-12}\frac{\mathrm{m}^3}{\mathrm{s}}$ since we are able to capture beads on a practicable length scale for a micro-chip with this volume flow. We start a grid of 100 beads placed in the inlet, and then we solve the trajectories for the beads with a simple program for $\boldsymbol{u} = (u_\mathrm{x}, u_\mathrm{y})$

$$u_\mathrm{x} = u_\mathrm{fluid}(y) \quad \text{and} \quad u_\mathrm{y} = \frac{F_\mathrm{mag}(x,y)}{6\pi\eta R} \tag{3.18}$$

The time-step was set so the beads at most moves 5μm between each calculation. The program code is shown in appendix H.

3.2.4 Data Treatment

After these simulations the start position of the i'th bead is given $(0, y_{0,i})$ connected with the end position $(x_{\mathrm{end},i}, 0)$ or $(x_{\mathrm{end},i}, h)$ depending on whether the beads are captured in the 'bottom' or 'top' of the channel. The end-position's x-coordinate is then coupled with start-postion's y-coordinate in a tabel $\boldsymbol{X}_1$ of coordinats, so the end position in the channel is given as a function of the start position in the channel.

$$\boldsymbol{X}_1 = (y_{0,i}, x_{\mathrm{end},i}) \tag{3.19}$$

The end position's x-coordinate is then coupled with start-postion's y-coordinate to describe the amount of captured beads as a function of the channel length in tabel $\boldsymbol{X}_2$,

$$\boldsymbol{X}_2 = \left(x_{\mathrm{end},i}, \frac{\sum_{y_0=0}^{h} u(y_0)\, G(y_{0,i})}{\sum_{y_0=0}^{h} u(y_0)} \right) \tag{3.20}$$

where,

$$G(y_{0,i}) = \begin{cases} 1 & \text{if } y_{0,i} < y_0 \\ 0 & \text{if } y_{0,i} > y_0 \end{cases} \tag{3.21}$$

3.2.5 Results

In this section we find the results for the different configurations of elements. First we use the $\mathbf{X}_1$ table so we are able to construct the end-position's as a function of the start-postion's in the channel.

All the symmetric systems are shown in figure 3.8 and in figure 3.9 we have zoomed in so we can tell the different systems apart from each other. We see that for the sym-

metric systems simulated, a bar spacing of 650μm is best.

All the asymmetric systems are shown in figure 3.10 and in figure 3.11 we have zoomed in so we can recognize the different systems from each other. We can see that for the asymmetric systems a bar spacing of 450μm is the best.

For the single systems we have found that for all the single and symmetric systems with the same bar spacing, follow almost the same curvature, and the single structures only capture in one side. In figure 3.12 we see this shown for a bar spacing of 550μm. Then we use the $\boldsymbol{X}_2$ table to determine the percentage of captured beads as a function of the channel length. This is shown in figure 3.13 for the symmetric systems and in figure 3.14 for the asymmetric systems. To get a quantitative expression of the behaviour we have compared the percentage of captured beads for a given channel length of $x = 0.07\,\mathrm{m}$. The results are given in table 3.3. We see from table 3.3 that the symmetric systems are better than the asymmetric systems, which is opposite to the simulation results from the first model. We believe this is due to the beads oscilating in the asymmetric systems. The two best of each type, the symmetric 650μm and the asymmetric 450μm is shown in figure 3.15.

3.2.6 Verification of analytic estimate)

To verify equation (3.17) we find in FEMLAB the size of the numerical magnetic force in the center of the channel, $F_{\mathrm{mag,c}}$, from a single element with a bar width of 50μm and a bar spacing of 750μm, see figure 3.16, where the numerical average force is about 2×10^{-14}N. If we insert this force with the volume flow we have used in the simulations $Q = 10^{-12}\,\frac{\mathrm{m}^3}{\mathrm{s}}$ we get the percentage of captured beads as a function of the channel length shown in figure 3.17. In figure (3.18) we see the percentage of captured beads as a function of the channel length for a single with a bar width of 50μm and a with bar spacing of 750μm found from the simulations. We can see in figure 3.17 that for the analytic solution to capture all beads need a channel of 10cm and from figure (3.18) that the solution found from the simulations to capture all beads need a channel of 43cm. The analytic equation (3.17) is then a factor 4.3 wrong.

The magnetic force in the center of the channel

To get an idea of how large an force we need in the center of the channel when we wish to capture 100 percent of the beads on a distance of 1cm and we expect that the beads are not affected by the gravity.

We isolate $F_{\mathrm{mag,c}}$ in equation (3.16) for $y_0 = w$ and get,

$$F_{\mathrm{mag,c}} = \frac{18\,\pi\,\eta\,R\,w^3}{h^3(w - 0.63\,h)}\frac{Q}{x_{\mathrm{end}}} \approx 5.9 \times 10^{-10}\mathrm{N} \tag{3.22}$$

We can then conclude that we need a force in the order 10^{-10}-10^{-9}N to capture a decent amount of beads on a micro chip unaffected by the gravity.

3.3 Summary

We have investigated a model of the magnetophoretic microfluidic systems, which include both magnetic effects and fluidic effects.

We have built an analytical model that calculates the percentage of beads captured along a channel for the single structures via the FEMLAB simulations and found that this is only a factor 4.3 wrong. We have also determined the percentage of beads captured as a function of channel length via simulations.

To carry out the actual simulation part, we have built a computer program in Matematica that imports magnetic simulation data from the first model (see section 3.1). Together with fluidic effects, these data are used to compute the trajectories of beads sent into one end of the channel. We use these trajectories to determine where the beads will be captured in a channel, and in this way also determine the percentage of beads captured as a function of the channel length. We use this as a measure of quality so that we can compare the different system designs we have dealt with in the first model in section 3.1.

We only simulate systems with element-widths of $50\,\mu$m since this was determined to be the optimum element width in the simulations of the first model in section 3.1. Of the systems we have simulated in model 2, we have found the best designs of each type to be the following:

- Double sided symmetric with spacing $650\,\mu$m.
- Double sided asymmetric with spacing $450\,\mu$m.

The single sided designs are nearly as good as the double sided symmetric designs.

Overall the best design (of the ones we have simulated) is the double sided symmetric system with an element-interspacing of $650\,\mu$m. Finally we have found that we need a force in the order 10^{-10}-10^{-9}N to capture a decent amount of beads on a micro chip unaffected by the gravity.

Setup			Integral ($Q_{M1} \times A$)	A	Q_{M1}
Type	Bar Width	Bar Spacing	[N m^2]	[m^2]	[N]
Single	50 μm	150 μm	1.1084×10^{-22}	1.44×10^{-8}	7.70×10^{-15}
Single	50 μm	250 μm	2.3563×10^{-22}	2.4×10^{-8}	9.82×10^{-15}
Single	50 μm	350 μm	3.544×10^{-22}	3.36×10^{-8}	1.05×10^{-14}
Single	50 μm	450 μm	4.6222×10^{-22}	4.32×10^{-8}	1.07×10^{-14}
Single	50 μm	550 μm	5.5509×10^{-22}	5.28×10^{-8}	1.05×10^{-14}
Single	50 μm	650 μm	6.3182×10^{-21}	6.24×10^{-8}	1.01×10^{-14}
Single	75 μm	150 μm	8.0657×10^{-23}	1.44×10^{-8}	5.60×10^{-15}
Single	75 μm	250 μm	2.0073×10^{-22}	2.4×10^{-8}	8.36×10^{-15}
Single	75 μm	350 μm	3.1558×10^{-22}	3.36×10^{-8}	9.39×10^{-15}
Single	75 μm	450 μm	4.2075×10^{-22}	4.32×10^{-8}	9.74×10^{-15}
Single	75 μm	550 μm	5.1233×10^{-22}	5.28×10^{-8}	9.70×10^{-15}
Single	75 μm	650 μm	5.8961×10^{-22}	6.24×10^{-8}	9.44×10^{-15}
Symmetric	50 μm	150 μm	1.8206×10^{-22}	1.44×10^{-8}	1.26×10^{-14}
Symmetric	50 μm	250 μm	3.3795×10^{-22}	2.4×10^{-8}	1.41×10^{-14}
Symmetric	50 μm	350 μm	5.0059×10^{-22}	3.36×10^{-8}	1.49×10^{-14}
Symmetric	50 μm	450 μm	6.7270×10^{-22}	4.32×10^{-8}	1.56×10^{-14}
Symmetric	50 μm	550 μm	8.4171×10^{-22}	5.28×10^{-8}	1.59×10^{-14}
Symmetric	50 μm	650 μm	1.0081×10^{-21}	6.24×10^{-8}	1.61×10^{-14}
Symmetric	50 μm	750 μm	1.1465×10^{-21}	7.2×10^{-8}	1.59×10^{-14}
Symmetric	75 μm	150 μm	1.3371×10^{-22}	1.44×10^{-8}	9.29×10^{-15}
Symmetric	75 μm	250 μm	2.7353×10^{-22}	2.4×10^{-8}	1.14×10^{-14}
Symmetric	75 μm	350 μm	4.1178×10^{-22}	3.36×10^{-8}	1.23×10^{-14}
Symmetric	75 μm	450 μm	5.6042×10^{-22}	4.32×10^{-8}	1.30×10^{-14}
Symmetric	75 μm	550 μm	7.0944×10^{-22}	5.28×10^{-8}	1.34×10^{-14}
Symmetric	75 μm	650 μm	8.5369×10^{-22}	6.24×10^{-8}	1.37×10^{-14}
Symmetric	75 μm	750 μm	9.8698×10^{-22}	7.2×10^{-8}	1.37×10^{-14}
Symmetric	100 μm	150 μm	8.9075×10^{-23}	1.44×10^{-8}	6.19×10^{-15}
Symmetric	100 μm	250 μm	2.2536×10^{-22}	2.4×10^{-8}	9.39×10^{-15}
Symmetric	100 μm	350 μm	3.4481×10^{-22}	3.36×10^{-8}	1.03×10^{-14}
Symmetric	100 μm	450 μm	4.7333×10^{-22}	4.32×10^{-8}	1.09×10^{-14}
Asymmetric	50 μm	150 μm	2.2077×10^{-22}	1.44×10^{-8}	1.53×10^{-14}
Asymmetric	50 μm	250 μm	4.5688×10^{-22}	2.4×10^{-8}	1.90×10^{-14}
Asymmetric	50 μm	300 μm	5.6156×10^{-22}	2.88×10^{-8}	1.95×10^{-14}
Asymmetric	50 μm	350 μm	6.5525×10^{-22}	3.36×10^{-8}	1.95×10^{-14}
Asymmetric	50 μm	450 μm	8.1341×10^{-22}	4.32×10^{-8}	1.88×10^{-14}
Asymmetric	50 μm	650 μm	1.0372×10^{-21}	6.24×10^{-8}	1.66×10^{-14}
Asymmetric	75 μm	150 μm	1.6015×10^{-22}	1.44×10^{-8}	1.11×10^{-14}
Asymmetric	75 μm	250 μm	3.9501×10^{-22}	2.4×10^{-8}	1.65×10^{-14}
Asymmetric	75 μm	350 μm	5.9611×10^{-22}	3.36×10^{-8}	1.77×10^{-14}
Asymmetric	75 μm	450 μm	7.5457×10^{-22}	4.32×10^{-8}	1.75×10^{-14}
Asymmetric	100 μm	150 μm	1.0152×10^{-22}	1.44×10^{-8}	7.05×10^{-15}
Asymmetric	100 μm	250 μm	3.329×10^{-22}	2.4×10^{-8}	1.39×10^{-14}
Asymmetric	100 μm	350 μm	5.4211×10^{-22}	3.36×10^{-8}	1.61×10^{-14}
Asymmetric	100 μm	450 μm	7.0554×10^{-22}	4.32×10^{-8}	1.63×10^{-14}

Table 3.2: Results from the 2D-simulations done in FEMLAB. The column "Integral" contains the values of $Q_{M1} \times A$ which is the number returned by FEMLAB. The value of A is calculated from knowledge of the width and length of the piece of channel over which we integrate.

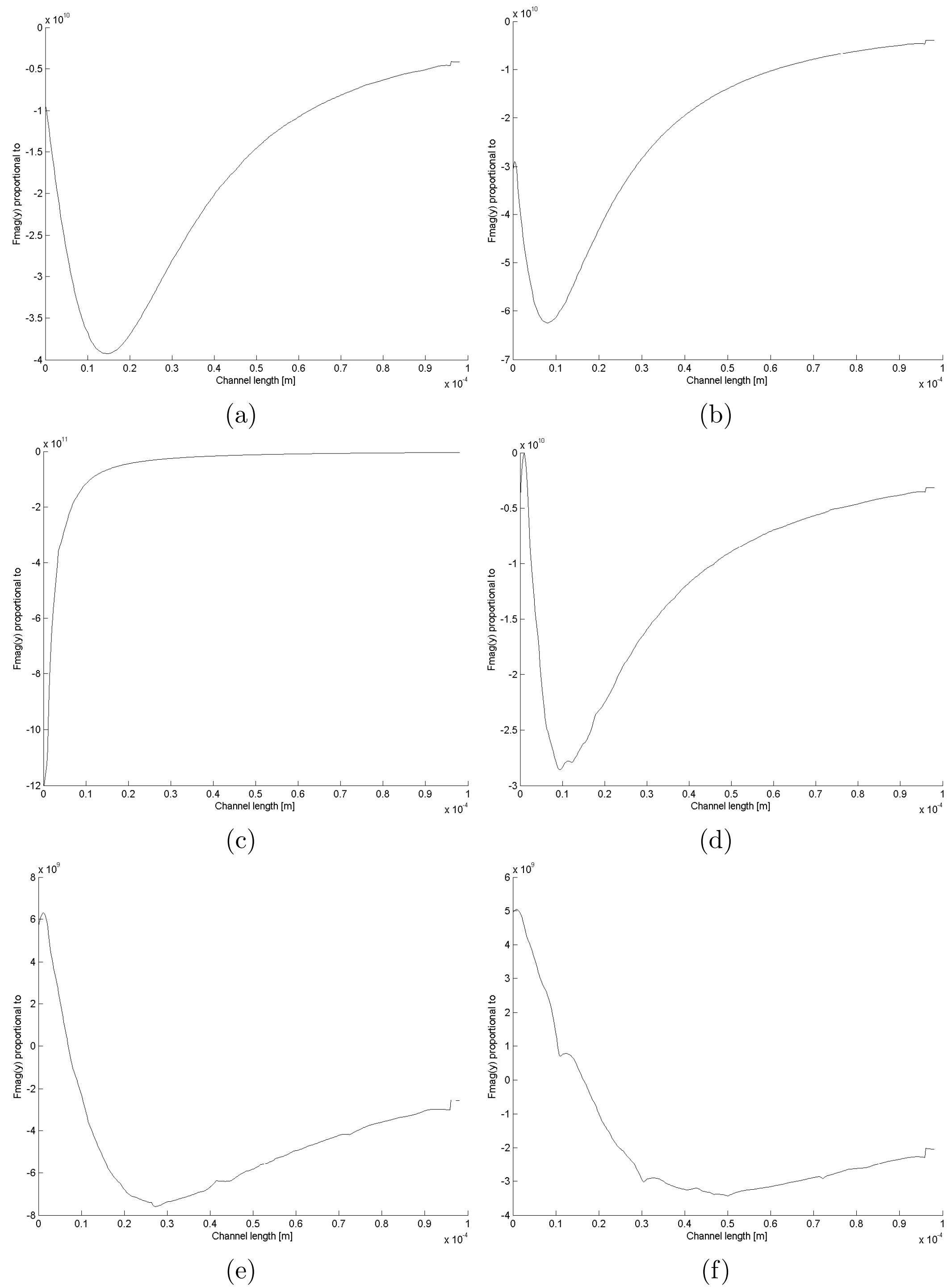

Figure 3.6: Line plots of the y-component of the magnetic force in channel from a single element in the cross-section given in figure 3.5. In (a) at cross-scetion 1, (b) at cross-section 2, (c) at cross-section 3, (d) at cross-section 4, (e) at cross-section 5 and (f) at cross-section 6.The cross sections are shown in figure 3.5.

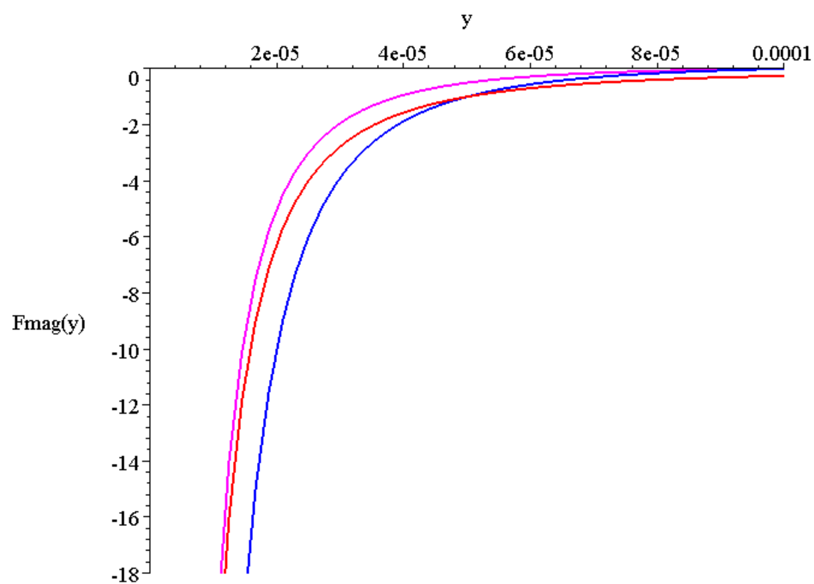

Figure 3.7: Different equations for the force from a single is element is plotted. Eq. (3.9) in red, Eq. (3.10) in purple and Eq. (3.11) in blue

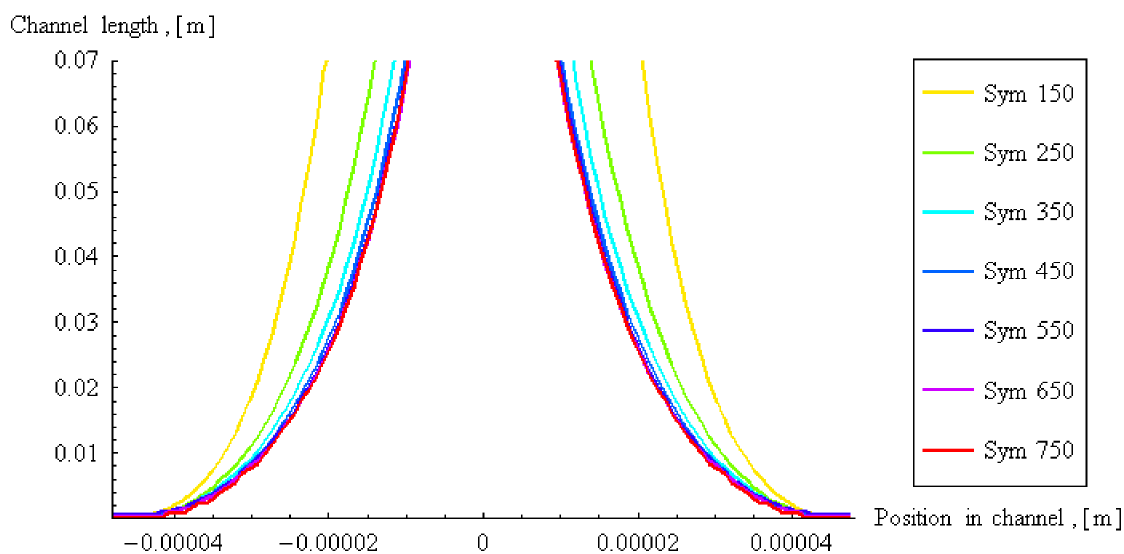

Figure 3.8: The capture point as function of the position for a bead in the symmetric systems.

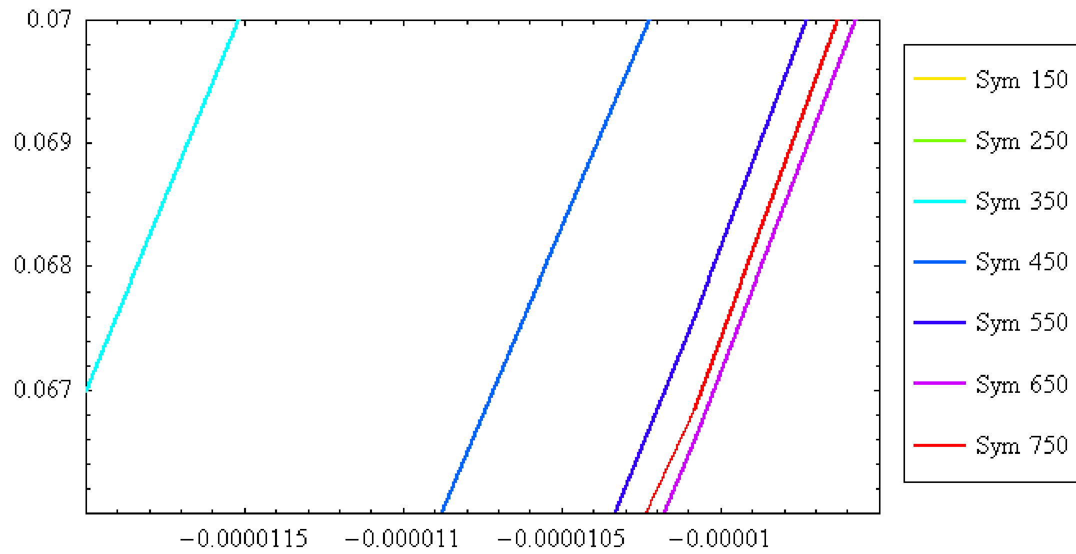

Figure 3.9: The capture point as function of the position for a bead in the symmetric systems, a zoom of figure 3.8.

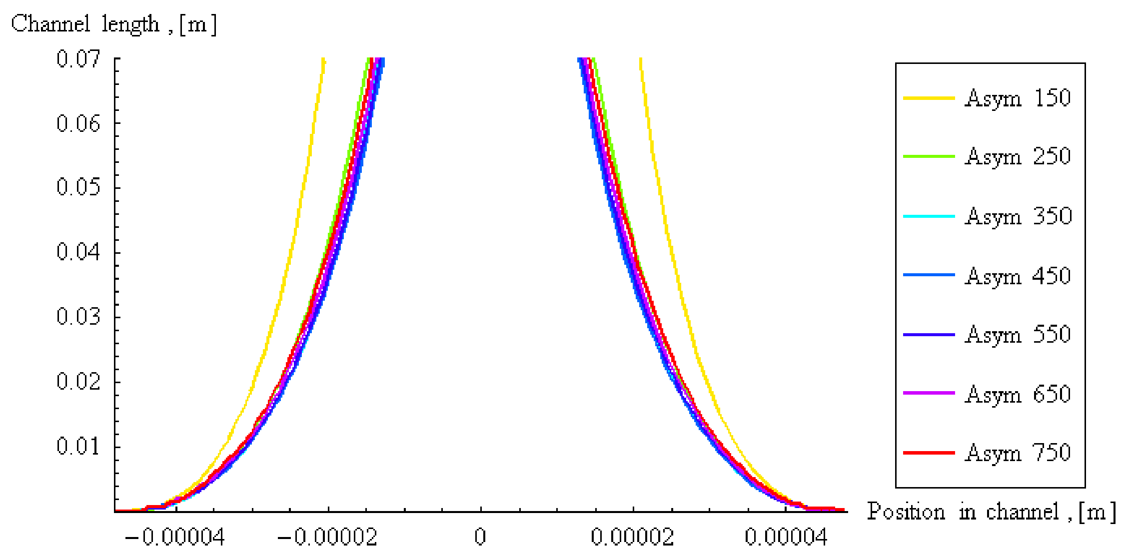

Figure 3.10: The capture point as function of the position for a bead in the asymmetric systems.

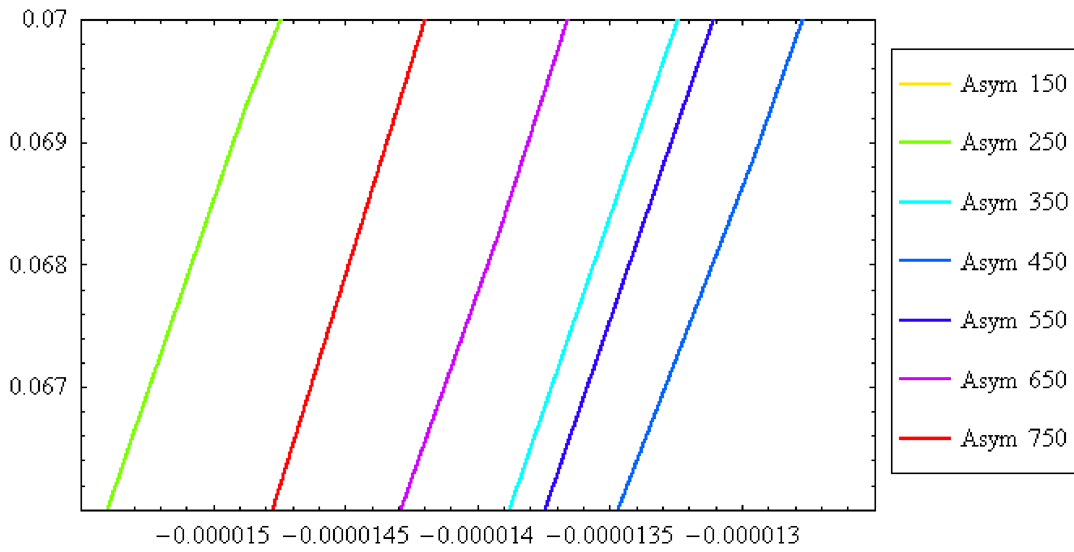

Figure 3.11: The capture point as function of the position for a bead in the asymmetric systems, a zoom of figure 3.10.

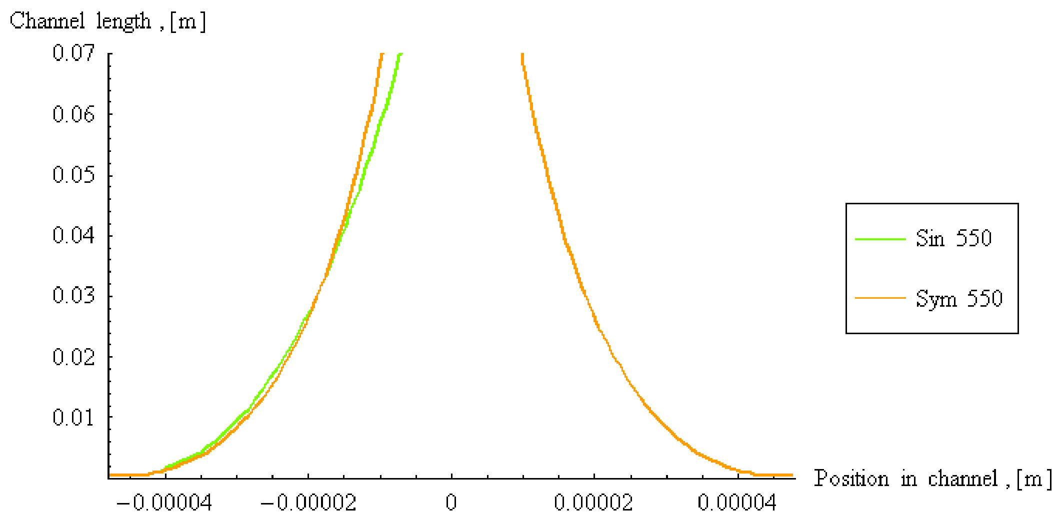

Figure 3.12: The single and symmetric system for a bar spacing of 550μm.

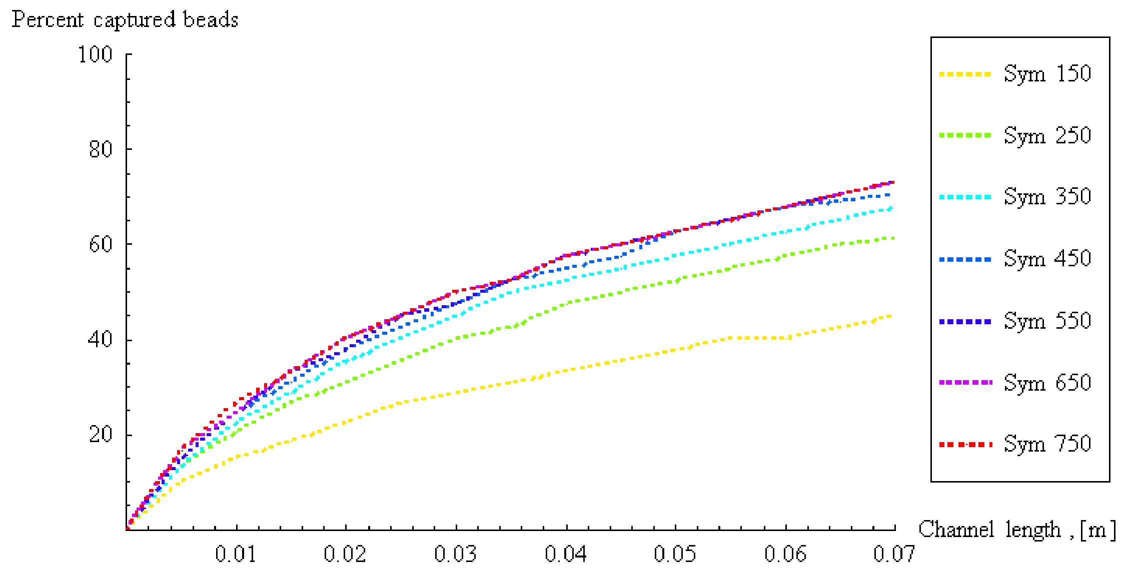

Figure 3.13: The percentage captured beads as a function of the channel length for the symmetric systems.

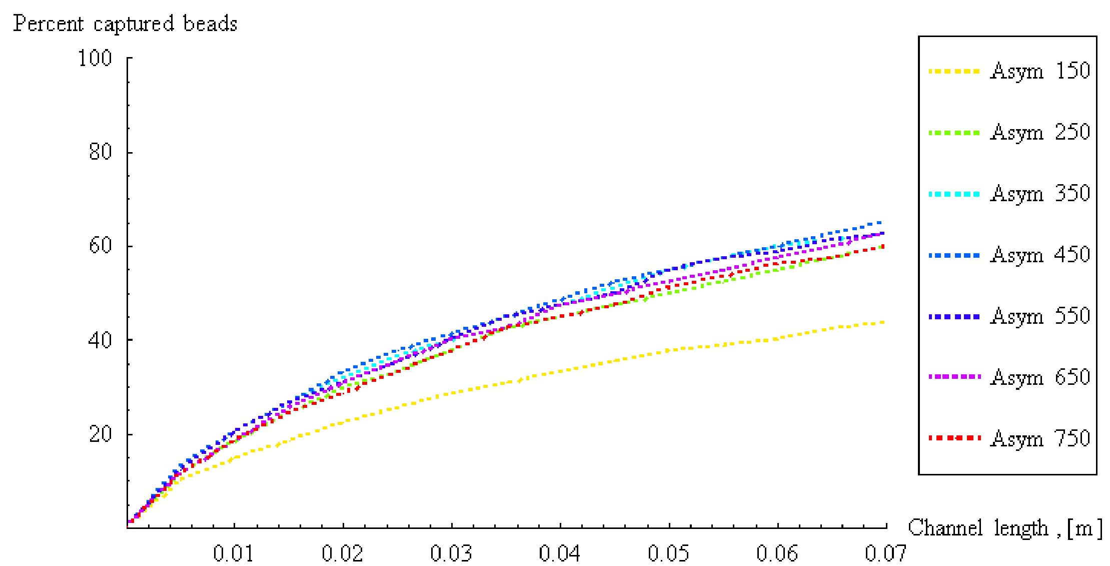

Figure 3.14: The percentage captured beads as a function of the channel length for the asymmetric systems.

Sym 150	Sym 250	Sym 350	Sym 450	Sym 550	Sym 650	Sym 750
44.8 %	61.2 %	67.3 %	70.4 %	73.0 %	73.0 %	73.0 %
Asym 150	Asym 250	Asym 350	Asym 450	Asym 550	Asym 650	Asym 750
43.9 %	59.9 %	62.5 %	65.1 %	62.5 %	62.5 %	59.9 %

Table 3.3: The percentage captured beads for a channel length of $x = 0.05\,\mathrm{m}$.

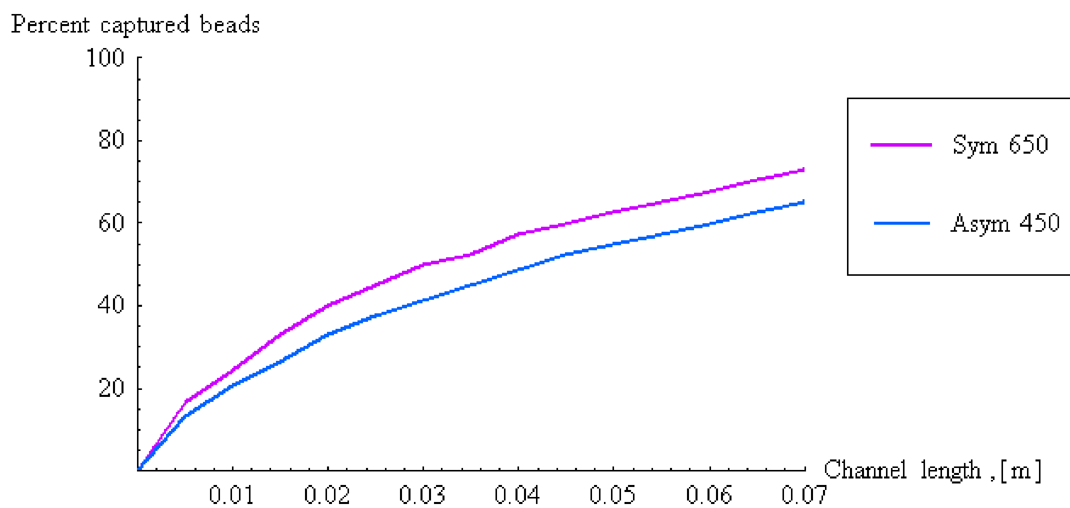

Figure 3.15: The percentage of captured beads as a function of the channel length for the symmetric 750μm and the asymmetric 450μm systems.

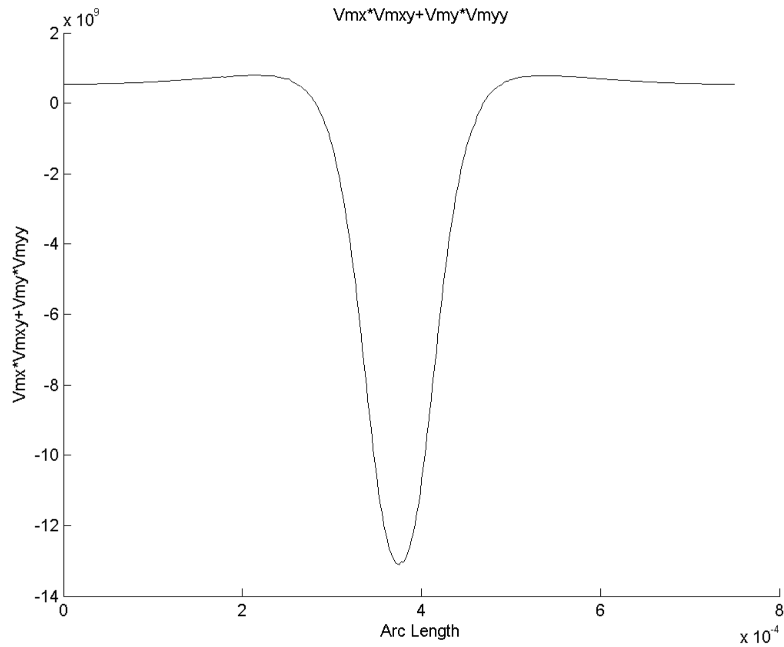

Figure 3.16: The y-composant of the force in the center of the channel from a single element with a bar width of 50μm and a bar spacing of 750μm.

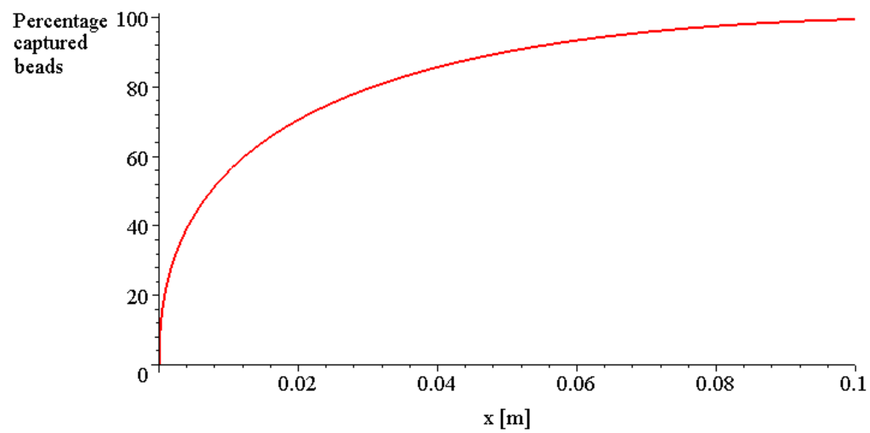

Figure 3.17: The percentage of captured beads as a function of the channel length for a single with a bar width of 50μm and a with bar spacing of 750μm found analytically.

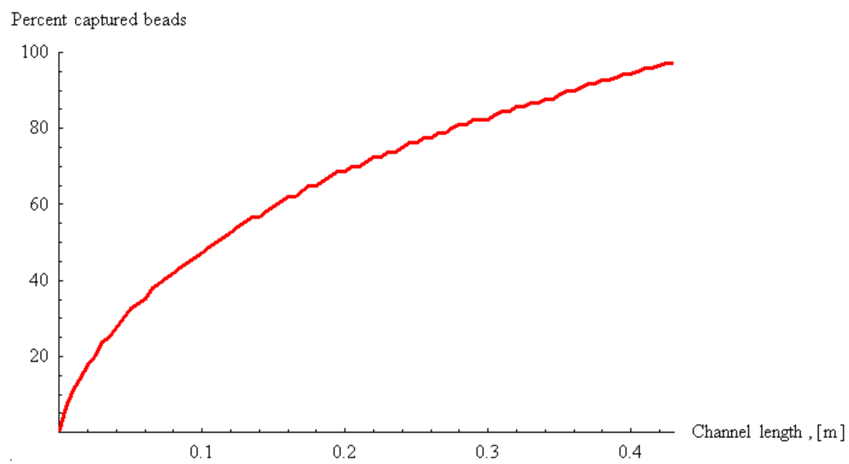

Figure 3.18: The percentage of captured beads as a function of the channel length for a single with a bar width of 50μm and a with bar spacing of 750μm found from the simulations.

Chapter 4

Experimental work

4.1 Introduction

This chapter describes the experimental work done during the project, as well as the thoughts and ideas leading to the tests we have created. In a previous 3-week course the fabrication of a similar chip was attemped, however unsuccesfull. We believe there was both mask design flaws, as well as large process design flaws. We have therefore in addition to the development of a new magnetophoretic chip design, developed a “SU-8 Test Mask”.

The experimental work is divided into two chapters, the first describes the ”SU-8 Test Mask” and the tests we have made with it and the conclusions drawn from these tests. The second chapter describes the magnetophoretic mask design, and the fabrication attempt made as well as the fabrication tests and some equipment tests we have made.

Chapter 5

The "SU-8 Test Mask"

This chapter discusses the ideas behind the "SU-8 Test Mask", the mask design and process parameters, the tests we have made and the evaluation of the results obtained.

Due to our previous fabrication problems in the cleanroom, it was decided to make a SU-8 test mask, on which we could study the adhesion between SU-8 and gold. We intend to study how the shape and size of the structures affect the adhesion, as well as determining the more optimal process parameters for the SU-8.

5.1 Ideas leading to the "SU-8 Test Mask"

During a 3 week course in January 2004 we attempted unsuccesfully to fabricate a magnetopforetic microfluid system, using a mask designed by our co-supervisor Mikkel Fought Hansen. We were having large and continous problems with the SU-8 simply falling off in large areas, as well as problems with a electroplating process step. It was decided to make a brand new mask design, but before making the mask design for our project, we decided to make this test mask to study how we might improve the design and process parameters for our next mask design and fabrication attempt.

The trouble in dealing with SU-8 is that it is still relatively new, and there are many process parameters that have not been fully tested and optimized for more specific applications such as ours. This mask design is made to determine some of the process parameters to be used in our final fabrication process, as well as hopefully giving us insight into how the dimensions of the SU-8 structures affect the adhesion. By studying the wafers from the 3-week course we believe it is important to minimize the overall size of the structures made in SU-8, as well as avoiding sharp corners where ever possible. We hope to prove this with our mask design.

5.2 Mask design

We have several different test structures on our masks as described below, and a few more are described in appendix E.

5.2.1 The channel

Our first priority is to study how the channel can be made, since we need to create a microfluidic channel on our final magnetophoretic chip. On the original magnetophoretic mask set, the channel was made by taking a $1\,\text{cm} \times 3\,\text{cm}$ rectangular structure made in SU-8, where the channel with in- and outlets are made by removing SU-8. The original design is shown in figure 5.1:

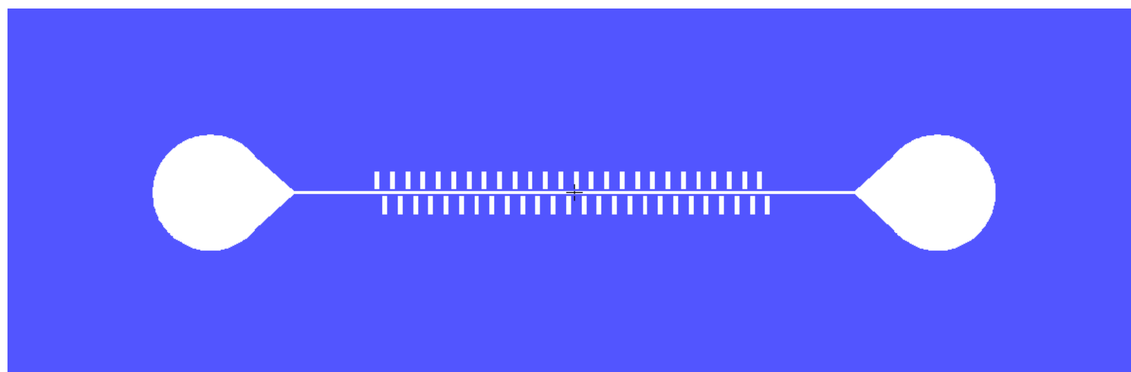

Figure 5.1: Sketch of the original channel design

The original channel is a very big structure, which we believe creates large stress between the gold and SU-8 layer resulting in adhesion failure. We have developed 2 approaches to solving this problem: The *walled channel* and the *stress relieved channel*. Two original channels are also included on the “SU-8 Test Mask” for comparison.

Walled Channel

The walled channel has the same dimensions for channel width, length and outlet diameter as the original channel, however the channel is now surrounded by a thin wall instead of the massive SU-8 structure. This can be seen on figure 5.2

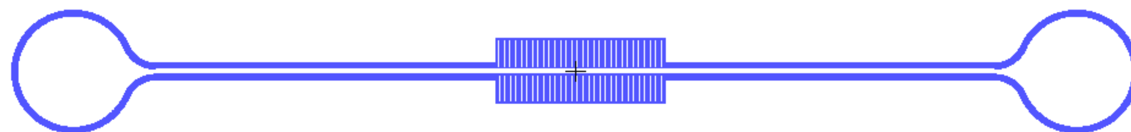

Figure 5.2: Sketch of walled channel. Wall thickness 100 μm wall

We have created two walled channel designs, one with 100 μm wide wall, and one with a 200 μm wide wall. We have also tried changing the diameter of the inlet and outlet holes, using both the original diameter 3 mm as well as a slightly smaller one with a diameter of 2 mm. The micro drill used to open a hole to the inlet/outlet is 1 mm wide, so we can

not schrink the inlet/outlets any more. We have also attempted to avoid sharp edges as much as possible, by rounding all edges.

Stress relieved channel

This design is very similar to the original channel design. The difference between the two is that the new design has rounded inlets and outlets and that the large SU-8 mass has been pierced with stress relieving holes. Each hole has a diameter of 150 μm and there are approximatly 7800 holes. We hope that these holes will help release the stress that is built up in the SU-8. The stress relieved channel can be seen on figure 5.3.

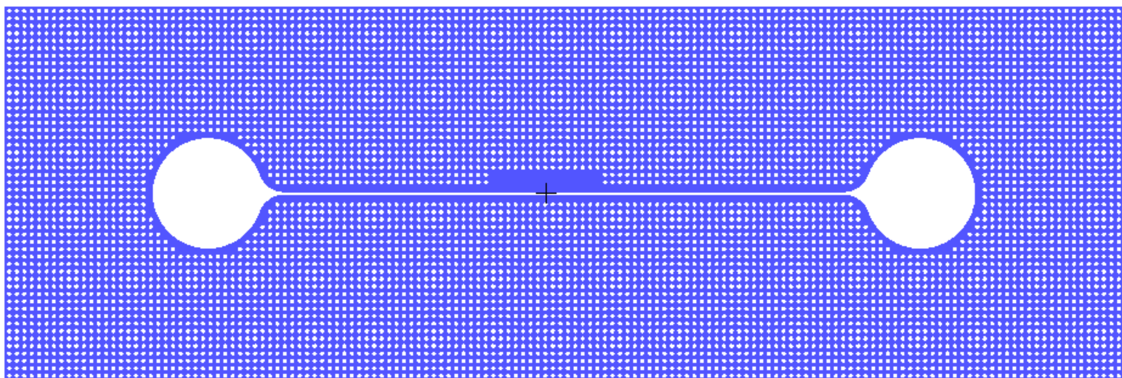

Figure 5.3: Sketch of the stress relieved channel. Holes have been made in the massive SU-8 structure to relieve built up stress.

5.2.2 Pull test squares

At the center of the design are 25 squares, which are meant to be used for pull tests. The squares are 5 mm $\times$ 7 mm. We intend for the pull tests to reveal the optimal process parameters. In this project the pull tests where only used to study different exposures, but the same mask design can be used for further testing.

5.2.3 Different size squares

On the mask is included a large amount of squares with sidewalls ranging from 50 μm to 2 cm. This is to study how the size affects the adhesion. Our theory is that larger structures experience more stress, and are thus more likely to experience adhesion failure. Furthermore on some of these structures we have made rounded corners, to see if they compensate for the large size. The squares are seen on figure 5.4:

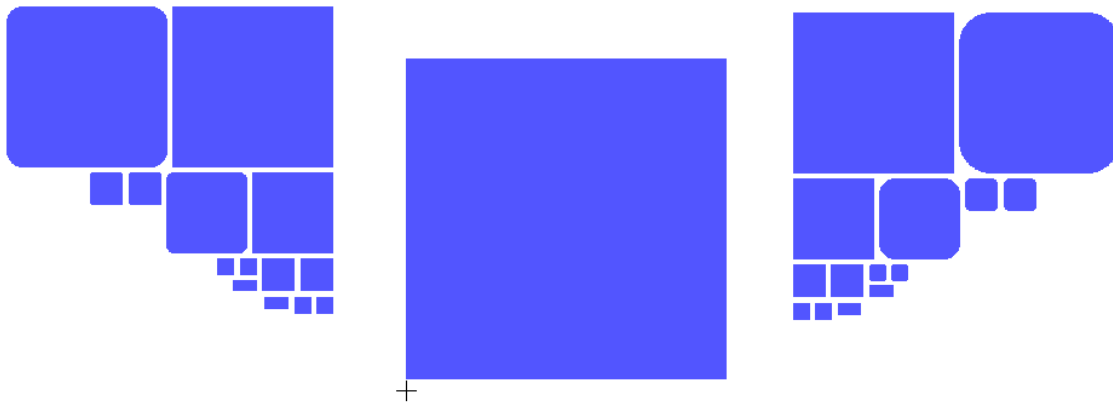

Figure 5.4: Different size squares

5.2.4 Triangles

Also included in the mask design are triangles of different size. All the angles are 60°. The sidelenghts vary from 50 μm to 2 cm. These structures have been included to test if there is a difference between structures of the same sidelength, but with different angles at the corners. In figure 5.5 we have shown the smaller triangles since they are the ones used for visuel inspection later on.

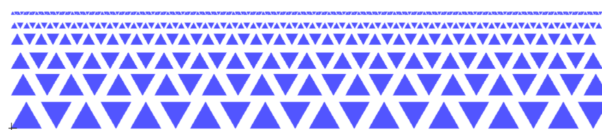

Figure 5.5: Triangles of different sizes

5.2.5 Text

There is also a small amount of text on the mask, the main purpose of which is to easily identify the wafers. The text simply states the project name, the name of the people in the group and the date of creation. This is shown in figure 5.6

SU8 TESTSTRUKTURER VERSION 1
ANDERS EBRO CHRISTENSEN
DANIEL EVAN NIELSEN
HENRIK GERT HASSAGER
23 FEB. 2004

Figure 5.6: Mask ID text

5.3 Fabrication

We have made four wafer batches of four wafers each, using the “SU-8 Test Mask”. Only four wafers are processed per batch due to hotplate limitations. The first two batches were “SU-8 2002 Visuel inspection” and “SU-8 2050 Visuel inspection” since the only inspection performed was a visuel one in a standard microscope. These two batches were fabricated prior to the processing of our MAP wafers. The third and fourth batch, the “SU-8 2002 Pull test” and the “SU-8 2050 Pull test” were fabricated after the manufacturing of the MAP wafers, and are called Pull test since Alicia Johansson and Maria Nordström performed pull tests on the squares previously mentioned. For all batches the primary parameter investigated was the exposure dose.

5.3.1 Process Sequence

This is the process sequence that was used for the manufacturing of SU-8 test wafers. For those not familiar with cleanroom processes there is a more in depth explanation of the terms used in appendix D. For specific batch details see appendix F.

- Fresh pyrex wafers are rinsed in Triton X-100 soap,
  followed by a 10 min immersion in Piranha
- E-beam deposition of 300 Å Ti and 1000 Å Au
- Plasma ash cleaning
- SU-8 2002 deposition
- Soft bake
- Exposure
- Post-exposure bake
- Development

The SU-8 2002 wafers are done at this point, and can be inspected in a microscope for the visuel tests, or diced for the pull tests. For the SU-8 2050 tests the process sequence continues below.

- Plasma ash cleaning
- SU-8 2050 deposition
- Soft bake
- Exposure
- Post-exposure bake
- Development
- Plasma ash, SU-8 monolayer removal

The Su-8 2050 wafers are now ready to be inspected in a microscope or be diced for the pull tests.
The last step, the SU-8 monolayer removal is done since we use the same final process step for our magnetophoretic chip design, and we want to make the SU-8 processing as close to the magnetophoretic chip processing to make comparisons easier.

5.4 Tests

There are several parameters influencing the adhesion of SU-8. Just to mention a few: The type of SU-8, the substrate type, the type of metal on the substrate and the amount, the exposure time, humidity, ambient temperature, spinning speed, spin acceleration, soft bake temperature, soft bake ramping time... and the list continues. It is therefore necessary to use some time optimizing the parameters for our process. This is however a very time-consuming process.

We have therefore chosen to focus on a few parameters and try to keep the remaining parameters as constant as possible. Spin parameters are taken from [1] and [2]. The ambient temperature and humidity are controlled in the cleanroom, but may still vary as much as 3 degrees and 10 %. The two types of SU-8 used, the substrate and the metal layer are held constant. From [1] and [2] we have a recommended exposure dose for SU-8, but those values are given for SU-8 on silicon, and we have SU-8 on a thin metal layer on top of a pyrex substrate, and we therefore need to adjust the exposure dose. Another parameter is the development time. This also affects the adhesion, but is not independent of the exposure dose, since the exposure dose determines the side wall profile, which again determines how the development proceeds.

Below is a description of each batch, followed by a description of the tests we have made and a summary of the results.

5.5 Batch “SU-8 2002 visual”

This is the first batch we made. We did not know the optimal exposure dose, and we did not even know the range. We therefore choose a broad range of exposure times ranging from 10 s to 175 s. By using a shutter along with the aligner only one sixth of the wafer is exposed, which allows for several exposures on each wafers giving a better coverage of the large range. By turning the wafer between exposures the same part of the mask is exposed each time, making the same structures for each exposure making comparison easier. Unfortunately only a small area and therefore few different structures are exposed, but this first batch allows us to narrow the range before the next batch. The exposure time is shown in table 5.1. The total is stated first, then how the dose was given. Multiple exposures are used to prevent heating of the wafers. The wait time between multiple exposurers is always 30 sec. The intensity was measured to: 8.9 $\frac{\text{mW}}{\text{cm}}$, to find the dose simply multiply the intensity with the exposure time.

We have taken microscope pictures of the exposed structures. These are seen on figures (5.7) and (5.8). Many of the exposure times were much too high, resulting in bad resolution which can clearly be seen from the pictures. From the visual inspection of the wafers it was decided that 25 s seemed to be the best exposure, and this exposure time has been used for the subsequent exposures of SU-8 2002.

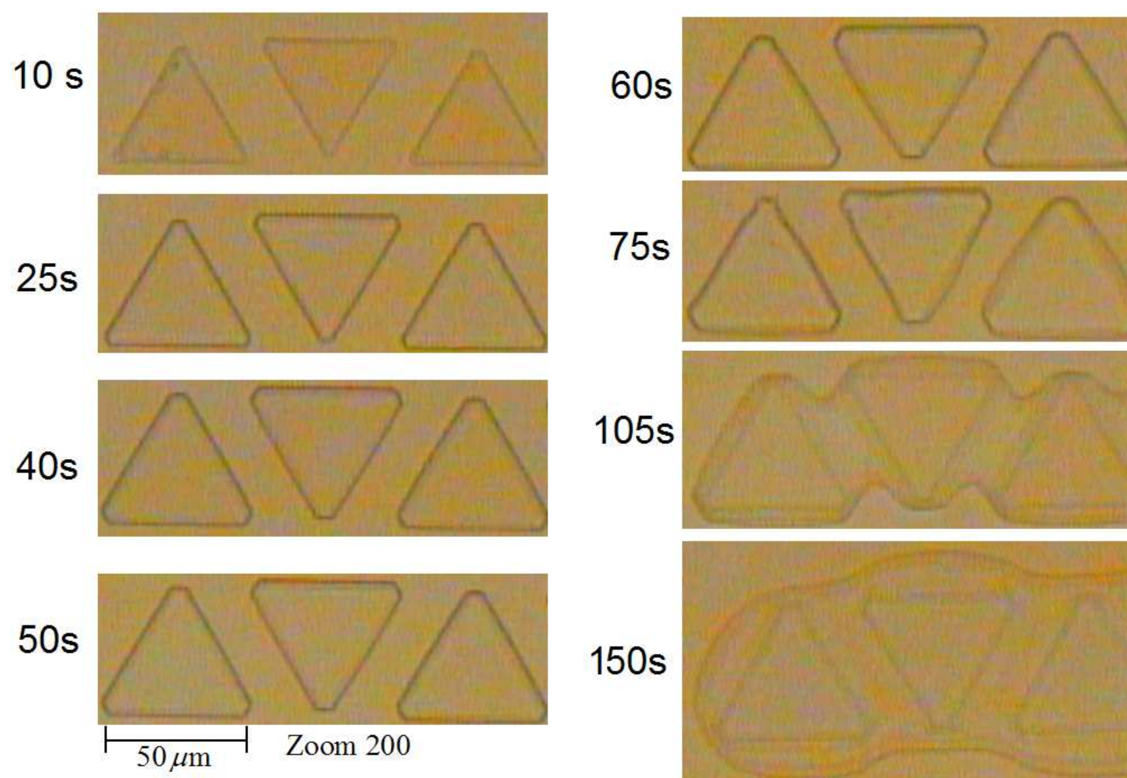

Figure 5.7: Triangle made in SU-8 2002. Sidelength 50 μm

5.6 Batch "SU-8 2050 Visual"

The second batch of wafers used the exposure dose found in "SU-8 2002 Visual", section 5.5, on a layer of SU-8 2002 before depositing the SU-8 2050. We thought it possible to align the first layer of SU-8 to the next, but discovered that it is not posssible to see a 2 μm layer of solidified SU-8, under a 50 μm layer of SU-8. Therefore the 2 layers are not aligned to each other making it hard to draw reliable conclusions from the exposure tests.

Wafers	Time 1	Time 2	Time 3	Time 4	Time 5	Time 6
1 and 2	10 s (1 x 10 s)	25 s (1 x 25 s)	40 s (2 x 20 s)	50 s (2 x 25 s)	60 s (2 x 30 s)	75 s (3 x 25 s)
3 and 4	90 s (3 x 30 s)	104 s (4 x 26 s)	120 s (4 x 30s)	135 s (5 x 27 s)	150 s (5 x 30 s)	175 s (7 x 25 s)

Table 5.1: Exposure times for "SU-8 2002 visual". (2x25 s) means that the exposure was split into two, first exposing for 25 s then waiting 30 s and then exposing 25 s again.

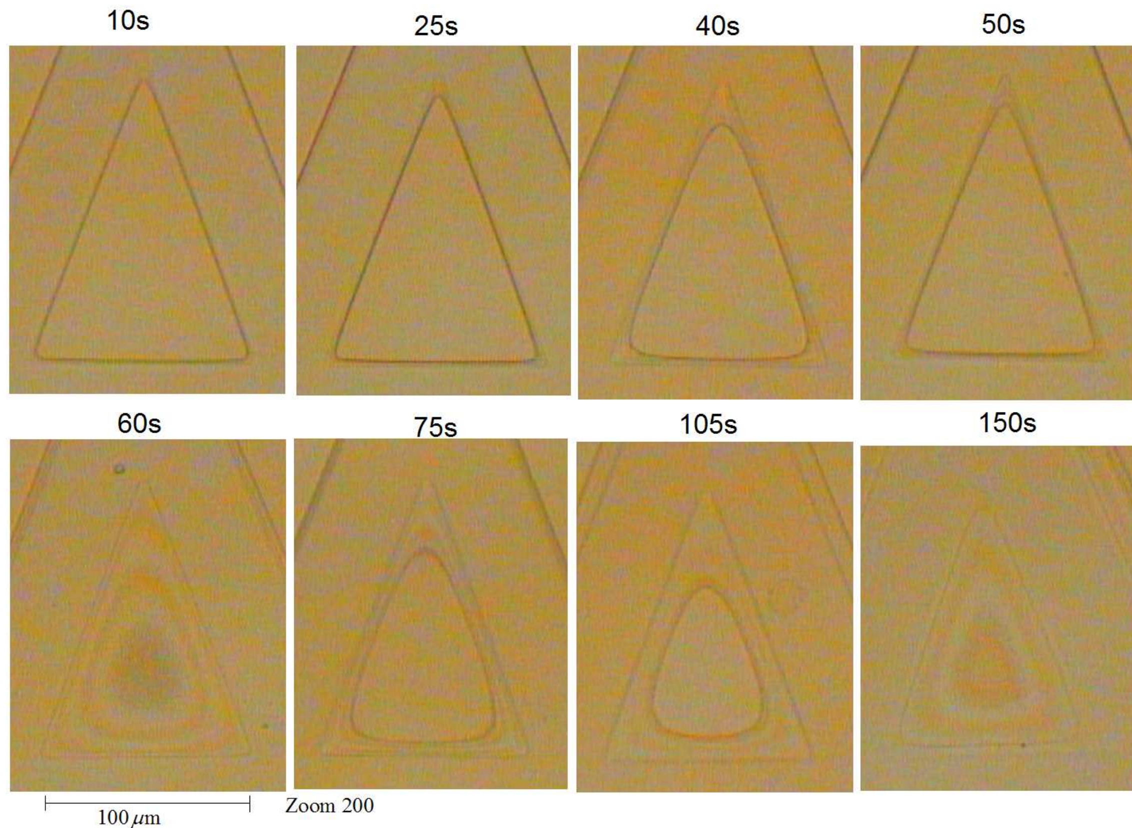

Figure 5.8: Triangular pit made in SU-8 2002. Bottom sidelength of triangle 100 μm. The exposure times are given above each figure. Note how the center hole becomes smaller with increasing exposure. This is caused by scattering of the exposure light.

It is however obvious that the underlying SU-8 2002 structures affect the exposure and adhesion of the top layer of SU-8 2050. The exposure times are given in table 5.2. The intensity was measured to: 8.9 $\frac{\mathrm{mW}}{\mathrm{cm}}$.

Allthough not having much reliably data due to distortion caused by the misalignment, it was decided the best exposure would be 60 sec, but more measuring points are definitly needed. From figure 5.9 it is clearly seen that a too small exposure dose results in many stress cracks. From figure 5.10(A) it can be seen that at 250 s, the magnetic structures cannot be developed properly due to overexposure as compared to figure 5.10(B) which has only received 90 s.

	Left	Right
Wafer 1	30 s (1 x 30 s)	60 s (2 x 30 s)
Wafer 2	90 s (3 x 30 s)	120 s (4 x 30 s)
Wafer 3	150 s (5 x 30 s)	200 s (8 x 25 s)
Wafer 4	250 s (10 x 25 s)	300 s (10 x 30 s)

Table 5.2: Exposure times for ”SU-8 2050 visual”

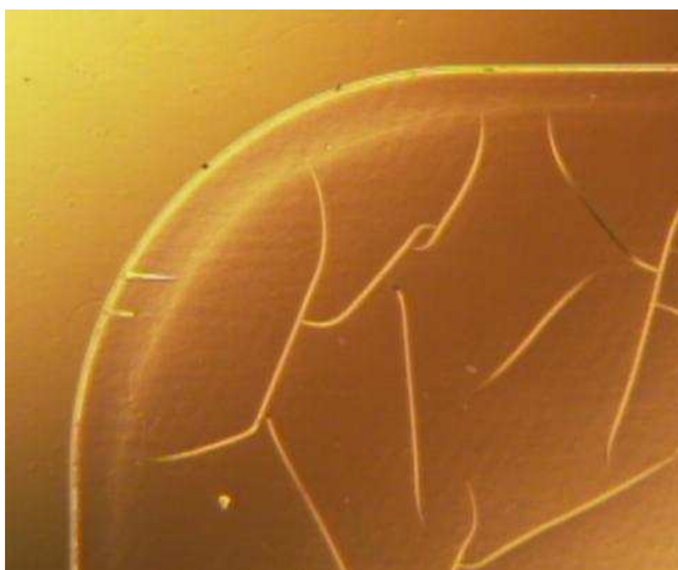

Figure 5.9: Under exposure results in stress cracks everywhere

5.7 Batch “SU-8 2002 Pull Test”

This Pull test batch is made using the information gained from the “SU-8 2002 Visual” batch to narrow the range. Exposure times are now between 10 s and 40 s as compared to the 10 s to 175 s used in the “SU-8 2002 Visual”. The exposure times used are shown in table 5.3.

When the manufacturing was done, the wafers were diced and pull tests were performed by Alicia Johansson and Maria Nordström.

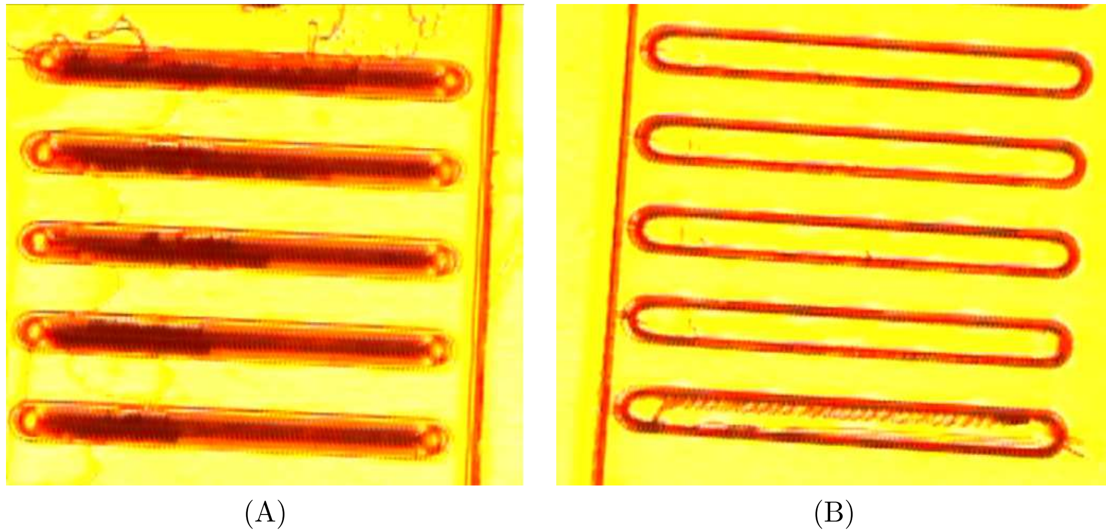

(A) (B)

Figure 5.10: (A) The wafer has been exposed for 250 s, which closes the holes making elektroplating impossible. (B) This wafer has been exposed for 90 s giving a much better result.

	Left	Right
Wafer 1	10 s (1 x 10 s)	15 s (1 x 15 s)
Wafer 2	20 s (1 x 20 s)	25 s (1 x 25 s)
Wafer 3	25 s (1 x 25 s)	20 s (1 x 30 s)
Wafer 4	35 s (2 x 17.5 s)	40 s (2 x 20 s)

Table 5.3: Exposure times for "SU-8 2002 Pull Test"

	Left	Right
Wafer 1	20 s (1 x 20 s)	30 s (1 x 30 s)
Wafer 2	40 s (2 x 20 s)	50 s (2 x 25 s)
Wafer 3	50 s (2 x 25 s)	60 s (2 x 30 s)
Wafer 4	70 s (3 x 23.3 s)	80 s (4 x 20 s)

Table 5.4: Exposure times for "SU-8 2050 Pull Test"

5.8 Batch "SU-8 2050 Pull Test"

This Pull test batch is made using the results gained from the "SU-8 2050 visual" batch to narrow the range. Exposure time now ranges from 20 s to 80 s as compared to the 30 s to 300 s used before. The new exposure times are shown in table 5.4. Another experience gained from the "SU-8 2050 visual" batch was to flood expose the SU-8 2002, thus having SU-8 2002 over the entire wafer surface since alignment was not possible.

When the manufacturing was done, the wafers were diced and pull tests were performed by Alicia Johansson and Maria Nordström.

5.9 SU-8 tests and their results

5.9.1 Pull tests

In a pull test the diced chips backside is glued to a holding device and another holding device is glued to the topside, unto the SU-8 layer. The devices are pulled from each other and the breaking load is recorded. The breaking load, is the load the chip can handle before adhesion failure. The bond strength is then calculated as $\frac{mg}{A}$, where m is the breaking load, g is the constant of gravity and A is the area of the chip, in every case $A = 5$ mm$\times$7 mm=35 mm^2.

Making the measurements is a very time consuming task, and therefore only few pull tests have been made. We have therefore choosen not to make pull tests of all exposures. For both SU-8 Pull test batches we choose 4 out of 8 exposures. 5 chips were used for each exposure, but especially for the thin SU-8 very few results were obtained. The results for SU-8 2002 are listed in table 5.5, the results for the SU-8 2050 are listed in table 5.6, and also in figure 5.11. So few results were obtained for SU-8 2002 that no figure was made.

SU-8 2002	Breaking Load [kg]	Bond strength [1×10^6 Pa]
Exposure: 15 s	26.19	7.34
	59.36	16.6
	66.82	18.7
Average		14.2
Exposure 20 s	76.28	21.4
Average		21.4
Exposure 25 s	39.69	11.1
Average		11.1

Table 5.5: Pull test results for SU-8 2002

SU-8 2050	Breaking Load [kg]	Bond strength [1×10^6 Pa]
Exposure: 30 s	47.05	13.2
	19.87	5.57
Average		9.38
Exposure: 40 s	15.43	4.32
	38.96	10.9
	23.41	6.56
	27.52	7.71
	22.88	6.41
Average		7.19
Exposure: 50 s	21.37	5.99
	32.33	9.06
	25.49	7.14
	7.72	2.16
	33.9	9.50
Average		6.77
Exposure: 60 s	48.38	13.6
	28.61	8.02
	49.77	13.9
	42.91	12.0
	38.49	10.8
Average		11.7

Table 5.6: Pull test results for SU-8 2050

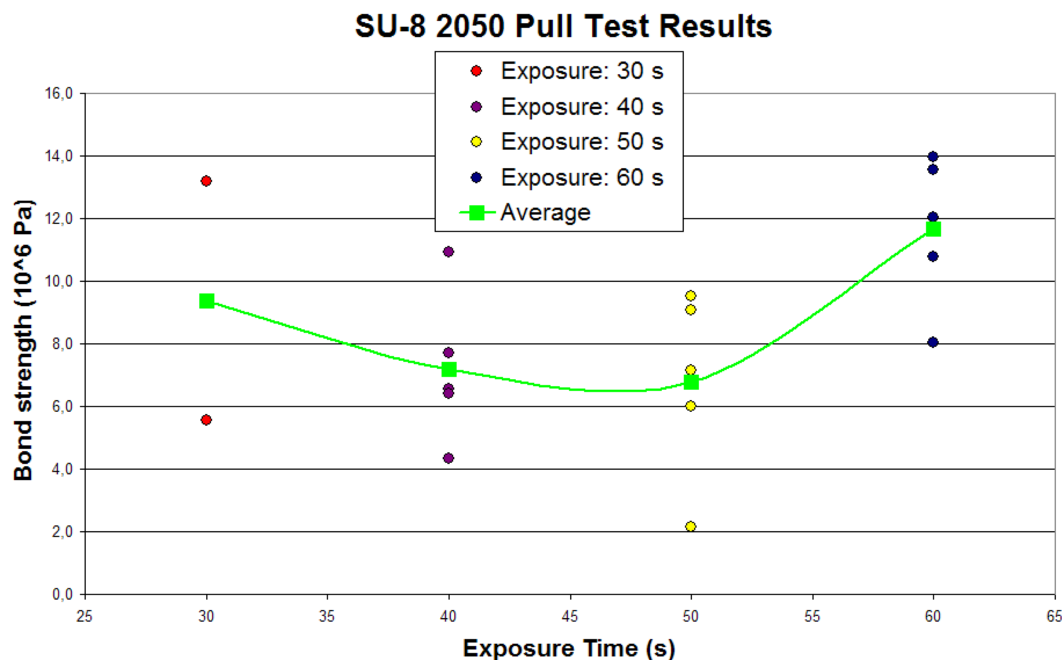

Figure 5.11: Results of the pull tests of the SU-8 2050

The results of the pull tests for each exposure are quite far apart, meaning that to get more reliable data more measuring points are needed. Looking at the average of each exposure however the variance between them is relatively small. Judging from the results it would seem that 60 s gives the best results for the pull tests, but more tests are needed, and judging from the initial results indicating that a optimum might be found, it should be worth researching more about this problem. We also conclude that for sensitive applications visual determination of the optimal parameters might not be sufficient, and that making pull tests could add more insight.

5.9.2 Plasma ash versus 250°C oven

In the 3-week course we used a 250°C oven to dehydrate the wafers before spinning on SU-8. This time we have used a plasma ash process to dehydrate the wafer surface. This has some practical benefits, but we did not know how it would affect the adhesion. If the oven is used, the wafers need to be placed in the oven overnight, making it very time consuming, as compared to the plasma ash, which in total takes ten min, and the time can be used to prepare the spinner. The plasma ash not only dehydrates the wafer surface, but also cleans it a little, as compared to the oven which is a dirty piece of equipment, since many other wafers are placed in the oven at the same time, and the high temperature in the oven helps release particles from the oven sides and other wafers, which can then land on our wafers. Finally we wish to use 2 layers of SU-8 this time. This means that for the

second dehydration process the first layer of SU-8 would be exposed to high temperatures for a very long time if the oven was used, and we know that SU-8 is sensitive to heat.

Using visual inspection after the SU-8 was spun onto the wafers, it seemed clear that the plasma ash also was superior to the oven when evaluating the effectiveness of cleaning the wafer making a better quality layer of SU-8. It could be interesting to make pull test comparisons between the plasma asher and the oven. It might have been a good idea also to include a visual inspection, to see if holes in the thin SU-8 layer are created during this process. The plasma ash might not etch the SU-8, but it might still influence the creation of holes, or even the adhesion.

The last thing to consider is that the plasma ash removes some material during the process. We wish to make the plasma ash powerfull enough to effectively dehydrate and clean the wafer, but without damaging or removing the first SU-8 layer, before spinning on the second. We used a *Dektak* height profiler to measure the height of the SU-8 before and after a plasma ash. There was no discernable change in height.

5.9.3 Soft-bake

In the 3-week course we used soft bake times ranging from 15 to 45 minutes at 95°C, since these were the process parameters given to us. We have found that the recommended parameters in [1] and [2], says to bake 1 min at 65°C and 2 min at 95°C for SU-8 on silicon. We decided to test whether these long baking times were really necessary to harden the resist, or perhaps even detrimental to the adhesion. We gave a SU-8 2002 wafer a 2 min bake at 65°C and 2 min at 95°C with a 2 min ramp in between. After cooling $\approx$ 40min we placed the wafer on a clean room wipe and pressed a tweezeer into the SU-8. No discernable marks were left behind and we therefore conclude that the new baking time is sufficient. For the thicker SU-8 2002 we used a 5 min bake at 95°C which was also sufficient.

5.9.4 Exposure

In the 3-week course we used an exposure time of 180 s, because we had been told that SU-8 can not be overexposed, and it is better to expose to much than to little. We have now found from the visuel inspections and the pull tests that the optimum exposure dose lies around 60 s, meaning that we used 3 times as much light as the optimal dosage resulting in extreme overexposure, which as seen on figure 5.8 results in closing of the smaller structures, which is not good for our process since we want precisely defined magnetizable elements from the electroplating, and if the structures are closed, bad or no electrical contact is the result. Extreme overexposure also makes the adhesion worse.

5.9.5 Development

In the 3 week course we developed the SU-8 for a total of 30 min, and even some wafers for 45 min because we were told that one can not overdevelop SU-8. We had earlier noticed SU-8 flakes starting to fall off allready while the wafer was still in the developer. We decided to use a shorter development time, with greatly enhanced results.

To ensure that it was the change of developer time and not one of the other changes we took two of the completed wafers from batch "SU-8 2002 visual" and two from "SU-8 2050 visual". We then placed them in the developer for an additional 20 min. We observed some SU-8 structures falling off from both batches, the largerst structures falling off first, especially the ones with square corners. We conclude that it is important not to develop the wafers more than necessary, and that it is indeed possible to overdevelop the wafers. It is stated in [2] that if the wafer is not developed enough a white film is seen on the wafer when rinsing.

5.9.6 Structures

One of the purposes of the SU-8 test mask was to test whether or not rounding the corners of the structures would be effective and if the size of the structures affects the adhesion. On figure 5.12 the top left corner of two squares with sidelength 1 cm is shown. The one with the square corner has suffered adhesion failure on the edge, allthough one should notice that the adhesion failure did not occur at the corner but on the side. We also found as we expected that larger structures are more prone to adhesion failure. Finally we note that with optimized process parameters larger structures can more easily be fabricated.

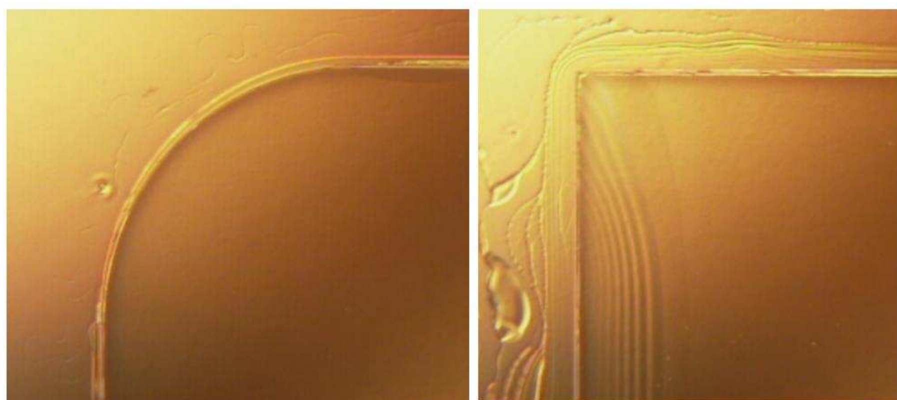

Figure 5.12: On the left is the rounded 1 cm×1 cm square, on the right a square of the same size but without rounded edges. The right square has suffered adhesion failure

We also compared the different types of microfluidic channel designs. The three designs on the wafer is the original channel surrounded by a large SU-8 rectangle, the walled channel where the channel is defined by a single wall, and finally the stress relieved channel which resembles the original channel, but where stress relieving holes has been placed throughout the structure. These channels are shown in figure 5.13 and are taken from the left side of wafer from batch "SU-8 2050 Pull test". For exposures around 50-60 s there is not much difference, but for the higher exposures doses the difference becomes significant. We conclude that the walled channel seems to be the best candidate.

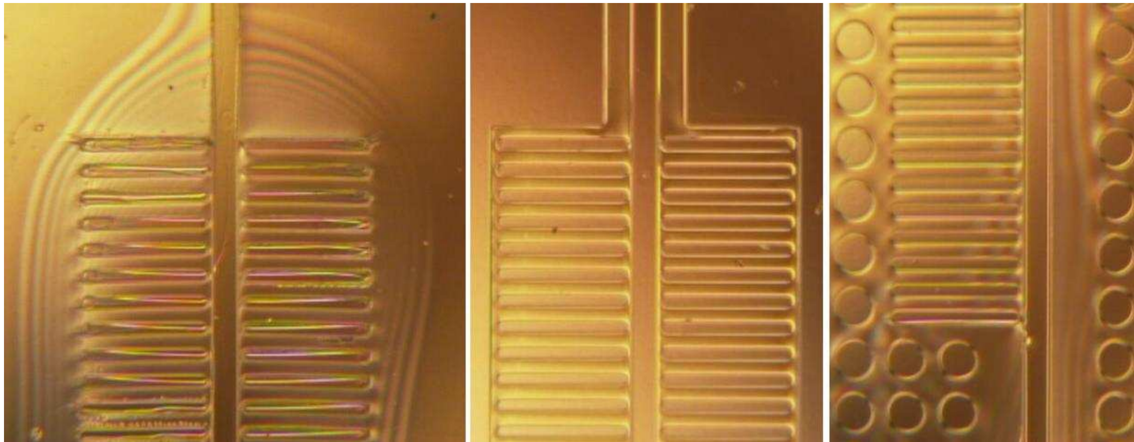

Figure 5.13: On the left is the original channel, which has suffered massive adhesion failure. The right is the stress relieved channel which has suffered some adhesion failure. The middle is the walled channel which seems to be the best candidate for making the channel and electroplating mould

For smaller SU-8 structures there is no discerneble effect of rounding the edges as can be seen from figure 5.14. The squares shown have a sidelength of 1000 μm.

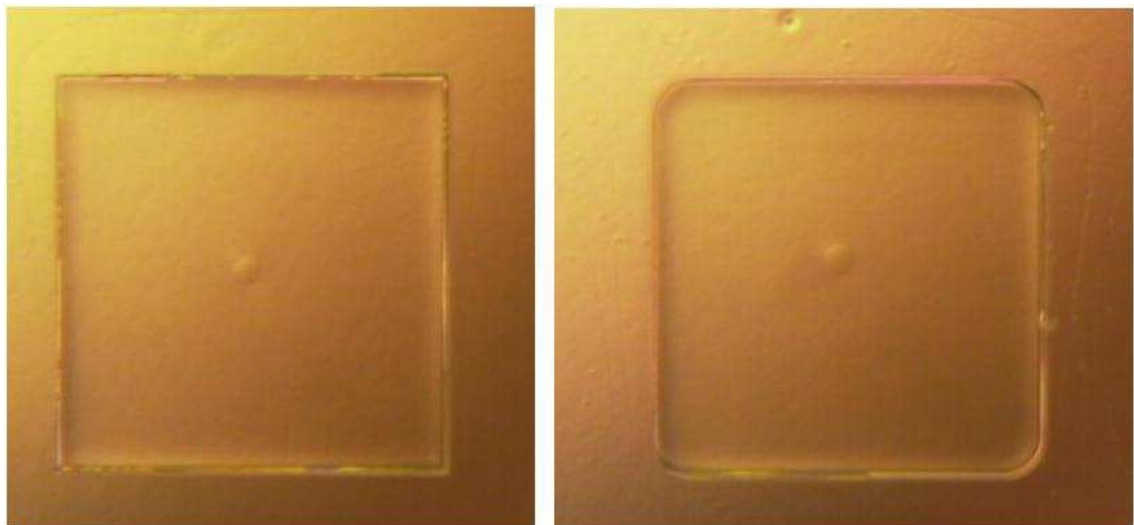

Figure 5.14: Smaller squares with sidelength 1000 μm made in SU-8. There is no discerneble effect of rounding the edges.

5.10 Two layers of SU-8

In the 3-week course we saw many newton rings caused by bad adhesion. They were almost on every structure. These effects are almost gone with the new structure design and process sequence. The new design however includes 2 layers of SU-8. The thin insulating layer and the thick mould layer. The interaction between these two layers is not straightforward. Figure 5.15 shows the corner of one of the rounded squares from the left side of wafer 2 from batch “SU-8 2050 Pull test”. Notice how there is a slight change of colour over the structure in the bottom left corner.

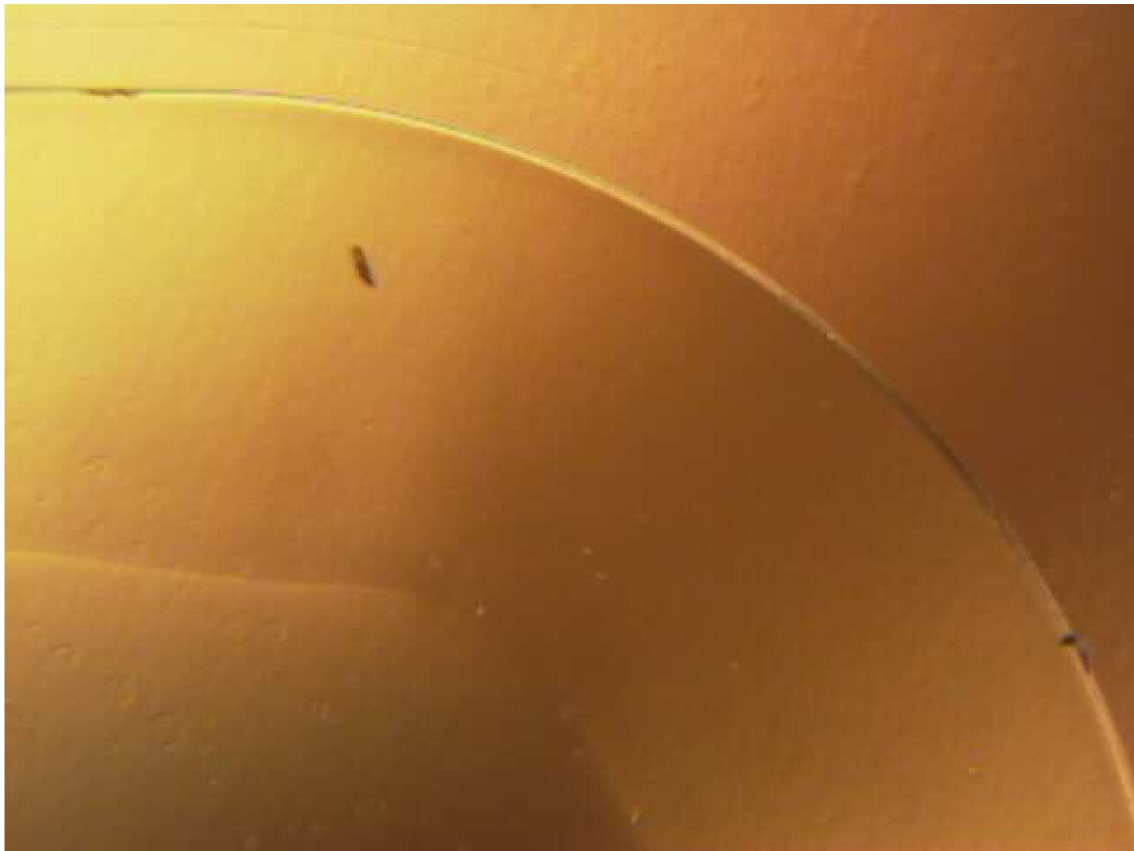

Figure 5.15: Corner of rounded square from pull test wafer 2 left side. Notice the slight change in colour in the bottom left corner.

It took a while to understand what we were seeing, but we had a wafer where a part of a square had been removed by accident. This is shown on figure 5.16. It can be seen that in the top right corner the SU-8 2050 pulled the SU-8 2002 with it when it was removed. On the top left side the SU-8 2002 remains while the SU-8 2050 have been removed. We conclude that the adhesion between the gold and the SU-8 2002 was better than between the SU-8 2002 and the SU-8 2050. Finally notice how the line marking the border between

the two areas just mentioned continues down to the bottom of the figure, where the SU-8 2050 has not been removed. We conclude that this nuance change marks bad or even zero adhesion between SU-8 2002 and SU-8 2050. We have not been able to establish a clear correlation between these nuance changes and the exposure time. We have found the rounded structures to be slightly better than the square structures. So far we have not found an explanation for this phenomenon.

Figure 5.16: Side of square structure. Top right area: Both layers of SU-8 removed. Top left area: SU-8 2002 remains while SU-8 2050 has been removed. Bottom Area: Both layers of SU-8 remain. Notice how the vertical line seperating the top areas continues below.

5.11 Summary

With our SU-8 test mask we have found that both the walled channel and the stress relieved channel are superior alternatives compared to the original channel design. The walled channel seems to be the best overall solution. We have found that rounding corners helps increase the adhesion, as well as reducing the size of the structures as much as

possible, however we have also found the optimizing the parameters lessons the impact of sharp edges and large structures. We have found that when working with SU-8 it is important to optimize the parameters for the application, especially the exposure dose. We have concluded that many of the parameters used in our 3-week course were far from the optimal parameters. The exposure dose has been reduced by a factor of 3, and the baking time by a factor of 9. Pull tests have been made, and however not quite succesfull seems worthy for further study and experiments. Finally we have found that plasma ashing is preferable to using the 250°C oven for dehydrating the wafers. Also tests have been made to ensure that the etching of the SU-8 by the plasma asher is not significant.

Chapter 6

Magnetophoretic Chip Fabrication

6.1 Introduction

We now wish to put simulations to the test. We therefore create a new mask set containing five different chip designs, each repeated twice on the wafer, one in which we use the "Stress relieving holes" concept developed during the SU-8 tests, and one in which we use the walled channel, also from the SU-8 tests. This chapter first contains a description of the mask design and the structures on it. Thereafter follows the process sequence used in the fabrication of the wafers. Unfortunately the fabrication was unsuccesfull, and therefore the final section only describes the tests we have made during processing to find our design flaws as well as the conclusions drawn from these tests. Some equipment tests are also made.

6.2 Mask Design

The magnetophoretic chip design consists of three masks. The first defines where the gold used as electroplating base should be. The second defines where the SU-8 2002 used for electrical insulation should be, and the final determines where the SU-8 2050 used as electroplating mould and channel walls should be.

6.2.1 The chip

On one wafer there is room for ten magnetophoretic chips. We have chosen to create a duplicate of each chip, thus having five different chip designs on the wafer. Half of these chips are created using the stress relieving holes design, the other half with the walled channel design which now has been supplemented by circular support pillars. The support pillars are made to facilitate lid bonding processes. The reason for choosing to make both the stress relieving holes concept and the walled channel concept was that we did not yet have the results from the SU-8 tests regarding wheter the walled channel or the stress relieved channel was the best, when the MAP mask was created. On figure 6.1(a) is shown where the gold is placed on the chip. Note that the actual chip is longer,

wider and with more elements than this sketch. On figure 6.1(b) the SU-8 2002 is shown, the yellow rectangles are where the gold is still visible and where the electroplating will be.The SU-8 2050 layer has been added on figure 6.1(c). The small dots on figure 6.1 (c) are the support pillars. On figure 6.2 the chip design with stress releasing holes are shown. The two first layers are the same.

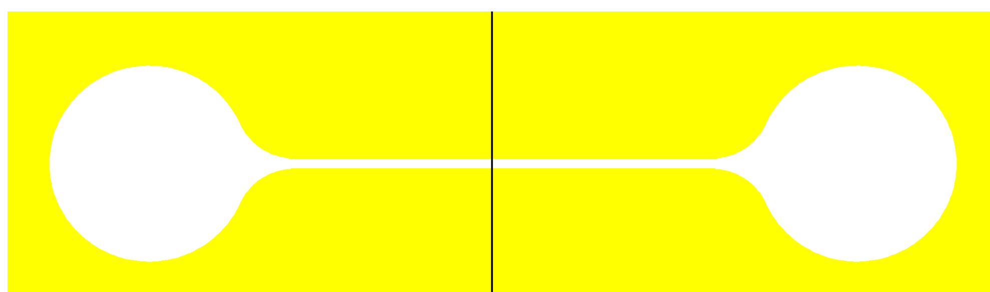

(a) The gold layer.

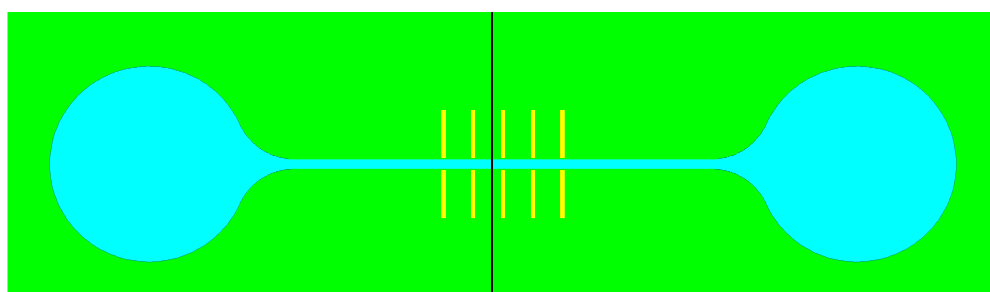

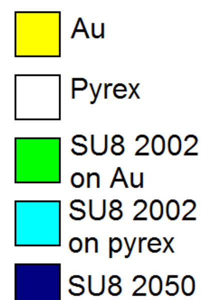

(b) The SU-8 2002 layer is added

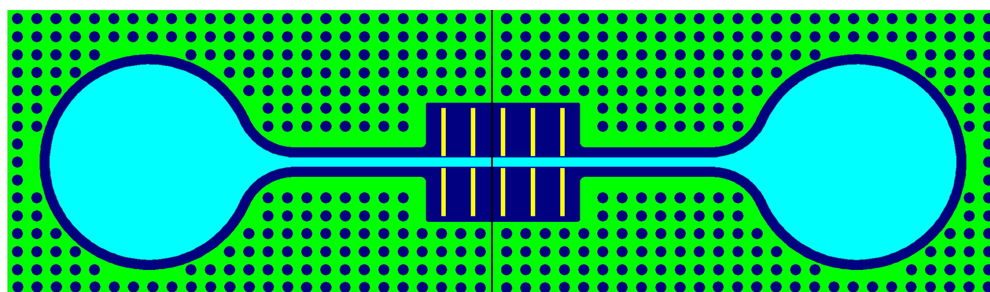

(c) The SU-8 2050 layer is added

Figure 6.1: The 3 layers in the chip design. The black center line marks where the figure has been squesed to make for a simpler sketch. The real chip is both longer and wider.

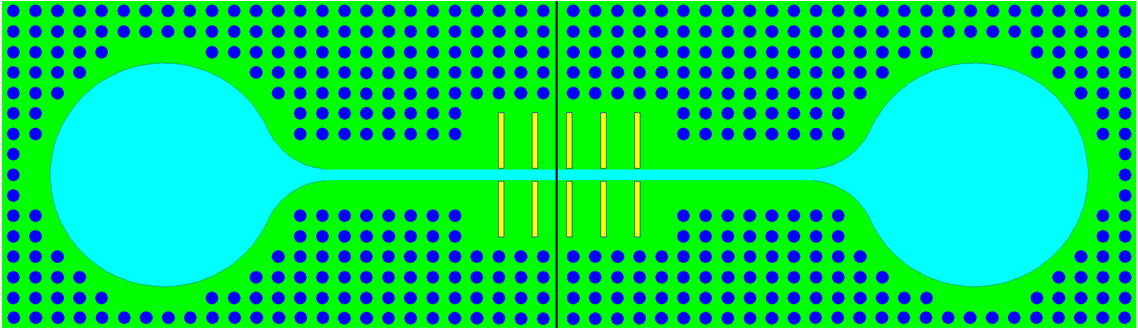

Figure 6.2: Sketch of the stress relieved channel

The actual chips made are listed in table 6.1. Each chip has been given a single letter name, which has been included on the mask, making it possible to distinguish the chips from each other with the naked eye.

Name	Type	Bar width (μm)	Bar length (μm)	Spacing (μm)	Number of bars
A	Symmetric	50	500	300	41
B	Symmetric	50	500	600	20
C	Symmetric	50	500	150	82
D	Asymmetric	50	500	600	20
E	Single Bar	50	500	300	41

Table 6.1: List of the chips on the mask design

6.2.2 Teststructures

Also included in the chip design are numoruos test structures. Some of these are to be used to determine the magnetic properties af the electroplated material, such as the permeability. Others are simply included to test design ideas we have. We have made structures with longer bars, with thinner bars and with thicker bars merely to see if it is possible to fabricate these structures, so that if another mask design is made one knows if these kind of structures can be fabricated. Especially we wanted to test whether the structures shown in figure 6.3 and 6.4 could be produced, since we have had some thoughts that a single long bar along the entire length of the channel could be interesting to study, but we did not wish to use one of the five chips on this design, since we thought it unlikely to succeed due to the very long very thin wall seperating the element from the channel. At the suggestion of Torben Tang from "Institut for produktion of ledelse" we have also made some test structures to study the effect of adding surrounding electroplating rectangles, hoping to make the electric field in the center more uniform. One of these tests chips

with four structures are shown in figure 6.5. On the chip the thickness of the surrounding electroplating rectangle and the distance to it is varied.

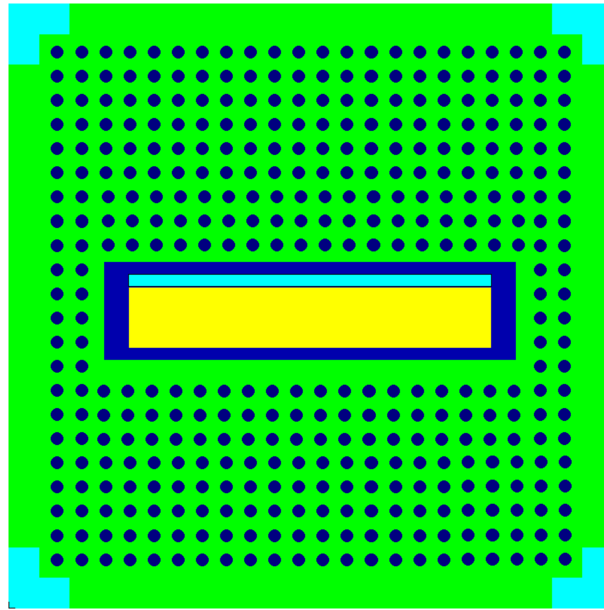

Figure 6.3: Thick single bar. The bar has a width of 3000 μm

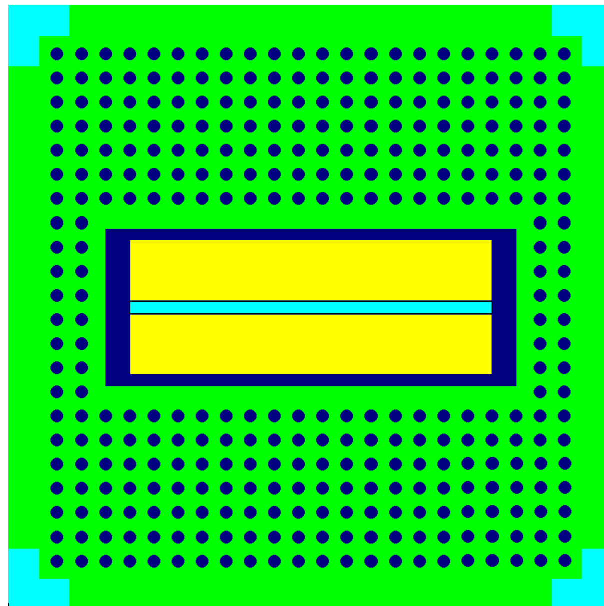

Figure 6.4: Thick double bars. The bars have a width of 3000 μm

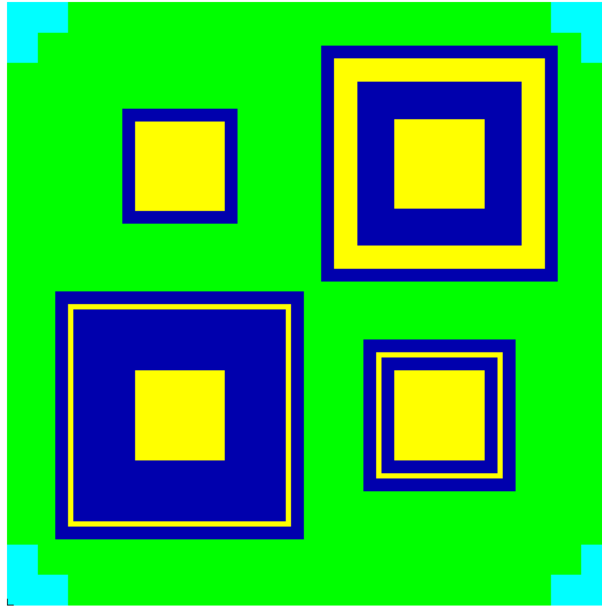

Figure 6.5: Test structure to make the electroplating electric field

6.3 Process sequence for Magnetophoretic Chip

The process sequence for the magnetophoretic chips is listed here. For the process parameter details, see appendix G. For those not familiar with cleanroom work and microfabrication processing more details about the process steps are given in appendix D

- Fresh pyrex wafers are rinsed in Triton X-100 soap,
  followed by a 10 min immersion in Piranha
- AZ5412E standard resist deposition
- Exposure using mask “#1 Gold, lift-off”
- Development
- E-beam deposition of 300 Å Ti and 1000 Å Au
- Plasma ash cleaning
- SU-8 2002 deposition
- Soft bake
- Exposure using mask “#2 SU8 Insulation/Bonding”
- Post-exposure Bake
- Development
- Plasma ash cleaning
- SU-8 2050 deposition
- Soft bake
- Exposure using mask “#3 SU8 Channels”
- Post-exposure Bake
- Development
- Plasma ash, SU-8 Monolayer removal
- Electroplating

6.4 Process tests and their results

This section contains the tests and the results drawn from our processing. We have chosen to divide the information into subcategories making it easier to find the desired information. This results in some things being repeated.

6.4.1 Electroplating

We have made 3 attempts at electroplating the wafers, which all failed. The process parameteres for each attempt is shown in appendix G. On the first attempt we aimed at making a 38 μm layer of Permalloy, but after electroplating it was clear that there was too much electroplated material filling the mould structures and flowing over the edges. However some of the problems with the electroplating creeping under the SU-8 and blocking the entire channel had been solved by the new mask and process design.

We have studied the composition of the material electroplated on the first wafer. Figure 6.6 shows a picture of the left chip C made using Scanning Electron Microscope (SEM). On figure 6.7 is shown the same structure made using x-ray diffraction. The structure is colour coded according to the elements found. Note that we are only studying the metal elements. This means that the black areas is the SU-8 photoresist composed mainly of oxygen and carbon. We wanted to examine how much metal had been electroplated on top of the SU-8 structures.

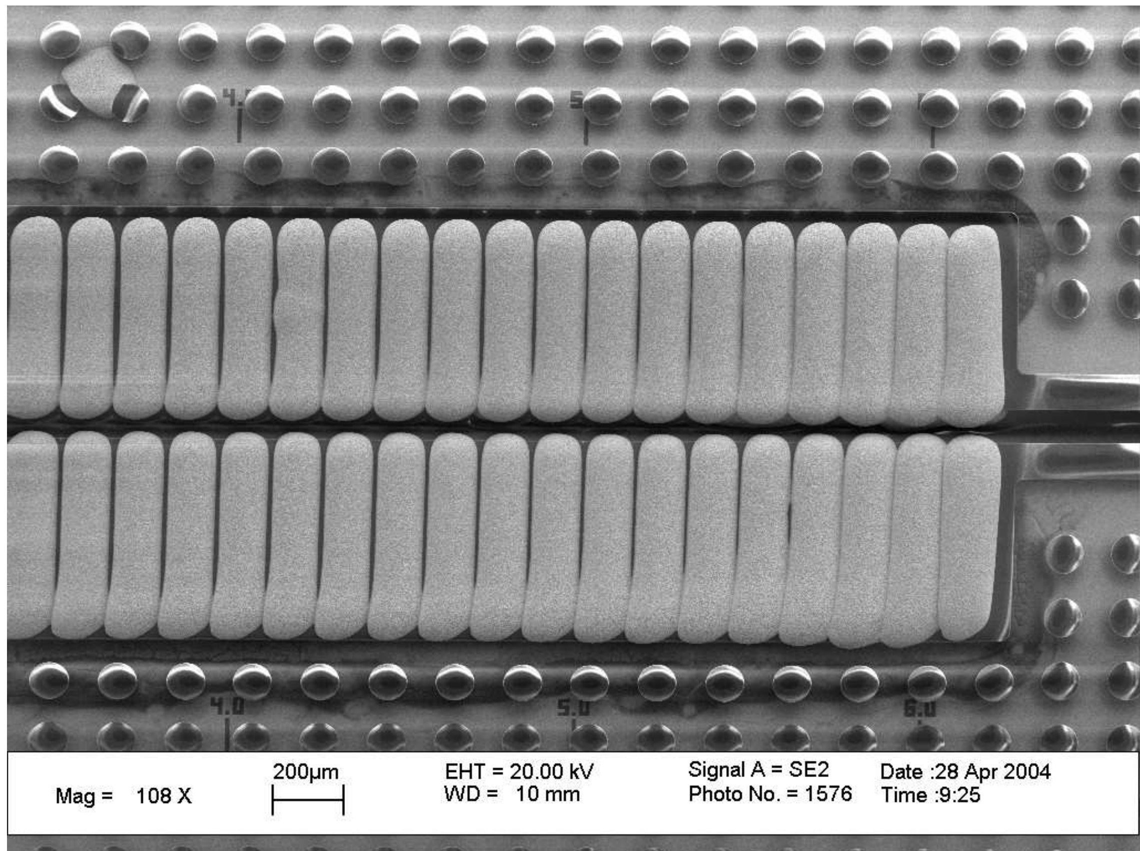

Figure 6.6: SEM image of the first electroplating attempt. Note the overflow

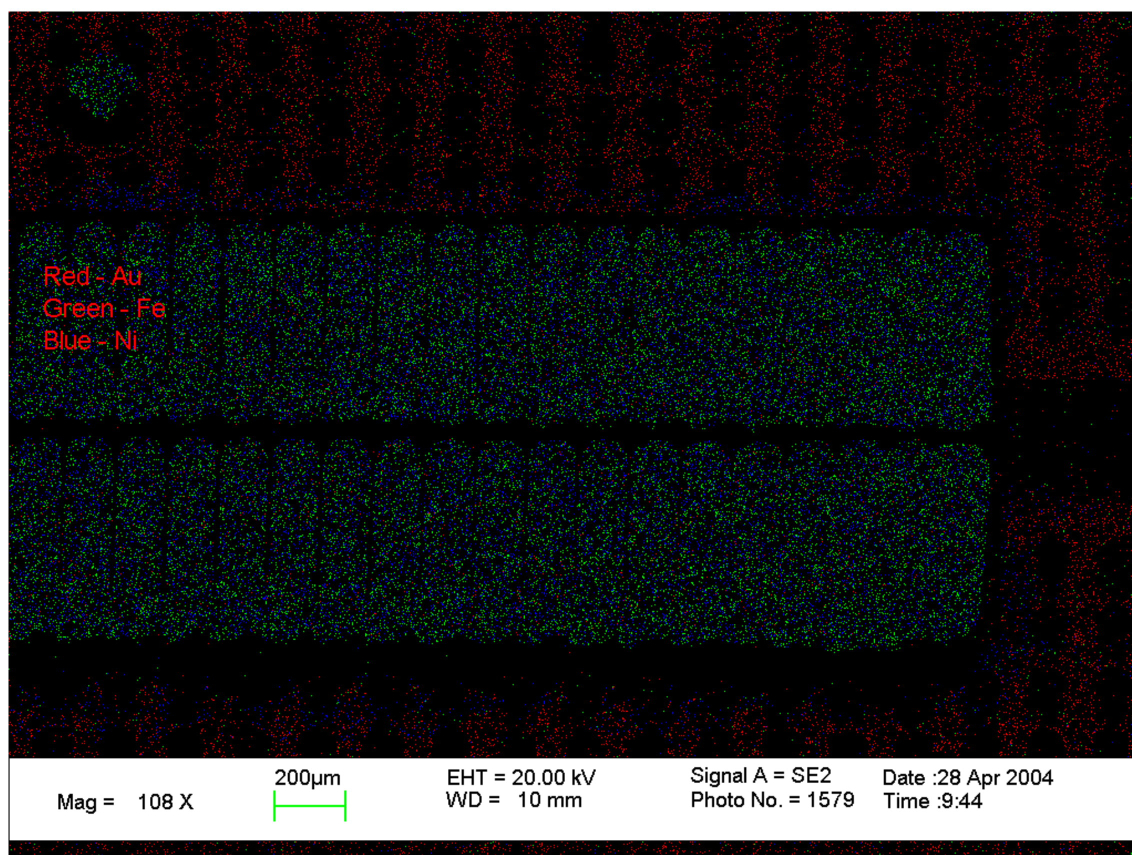

Figure 6.7: X-ray diffraction of the structure shown in 6.6. The elements found are colourcoded

The pictures show that the material is electroplated mostly in the right places, however sometimes large areas of material appear such as the material at the topmost left corner. We believe this happens due to holes in the thin SU-8. As we will show later in section 6.4.4 the SU-8 2002 layer is only 0.6 μm to 0.7 μm thick instead of the expected 2 μm, this makes it even more likely that small cracks or holes in the SU-8 2002 layer could appear. The solution could be to use a thicker layer of SU-8 which could be made with SU-8 2005.

X-ray diffraction has also been used to determine the mass composition of the electroplated material. To make Permalloy we need to achieve a composition of 80:20 Ni:Fe. The achieved results measured with x-ray diffraction on the first attempt was: 70:30 in some places and 65:35 in other places. This is not perfect but close to the desired result. In the second attempt we tried increasing the current density to enhance the composition to 80:20, which resulted in improvements at some points on the the wafer and worse results at other points. From figure 6.8 it is also clear that the increased current density destroys some of the SU-8 structures.

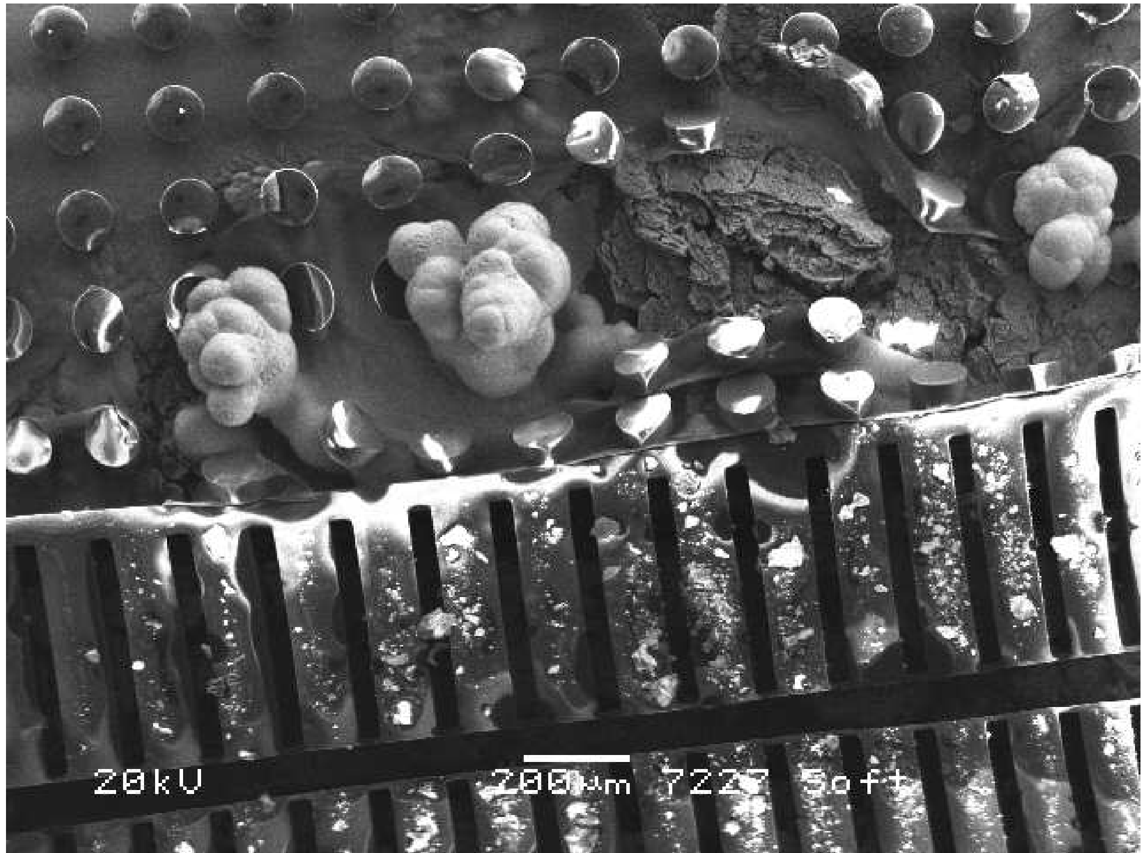

Figure 6.8: SEM image of electroplating destroying the SU-8. The electroplating actually pushes the SU-8 aside on top of each other.

We were also surprised to see that the teststructure earlier shown in figures 6.3 and 6.4 were quite succesfull contrary to our expectations. The results of the electroplating are shown in figure 6.9 and 6.10. These results are good, in spite of the gold having been removed from these structures as well, and we conclude that in a future MAP mask design one of these structures should be incorporated as one of the chips.

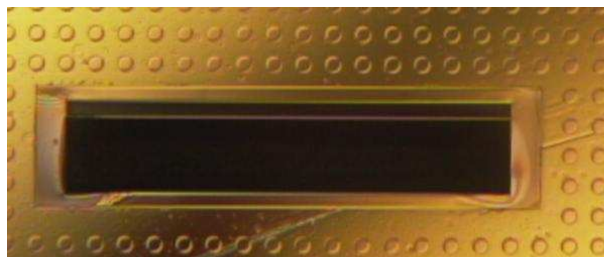

Figure 6.9: The succesfull electroplating of the very large single bar test structure

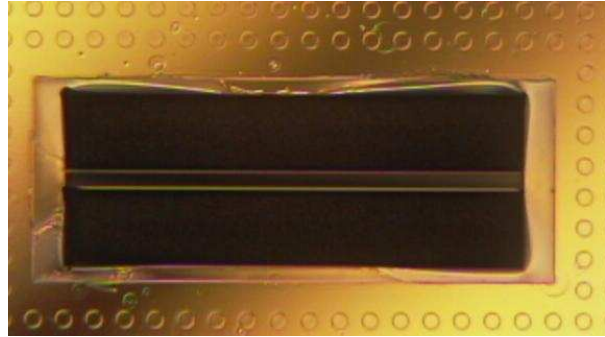

Figure 6.10: The succesfull electroplating of the very large double bar test structure

Solutions to the electroplating problems

We noticed that while all the magnetophoretic chips had their channels filled with electroplated material, this did not happen for most of the test structures also included on the wafer. The main difference between the chips and the teststructures is that we remove the gold from the channels in order to make a visuel inspection of the experiments easier. In figure 6.11 two channels in which the gold has been removed, and electroplating has blocked the channel is shown. In figure 6.12 one of the electroplated test structures are shown. The electroplating has not blocked the channel on the test structure.

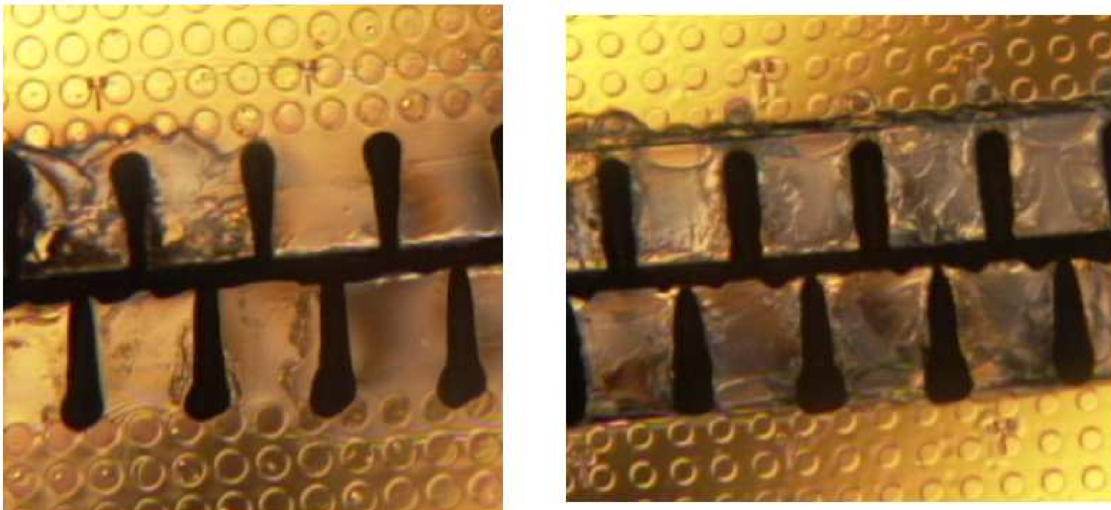

Figure 6.11: Two chips are shown in which the electroplating has blocked the channels.

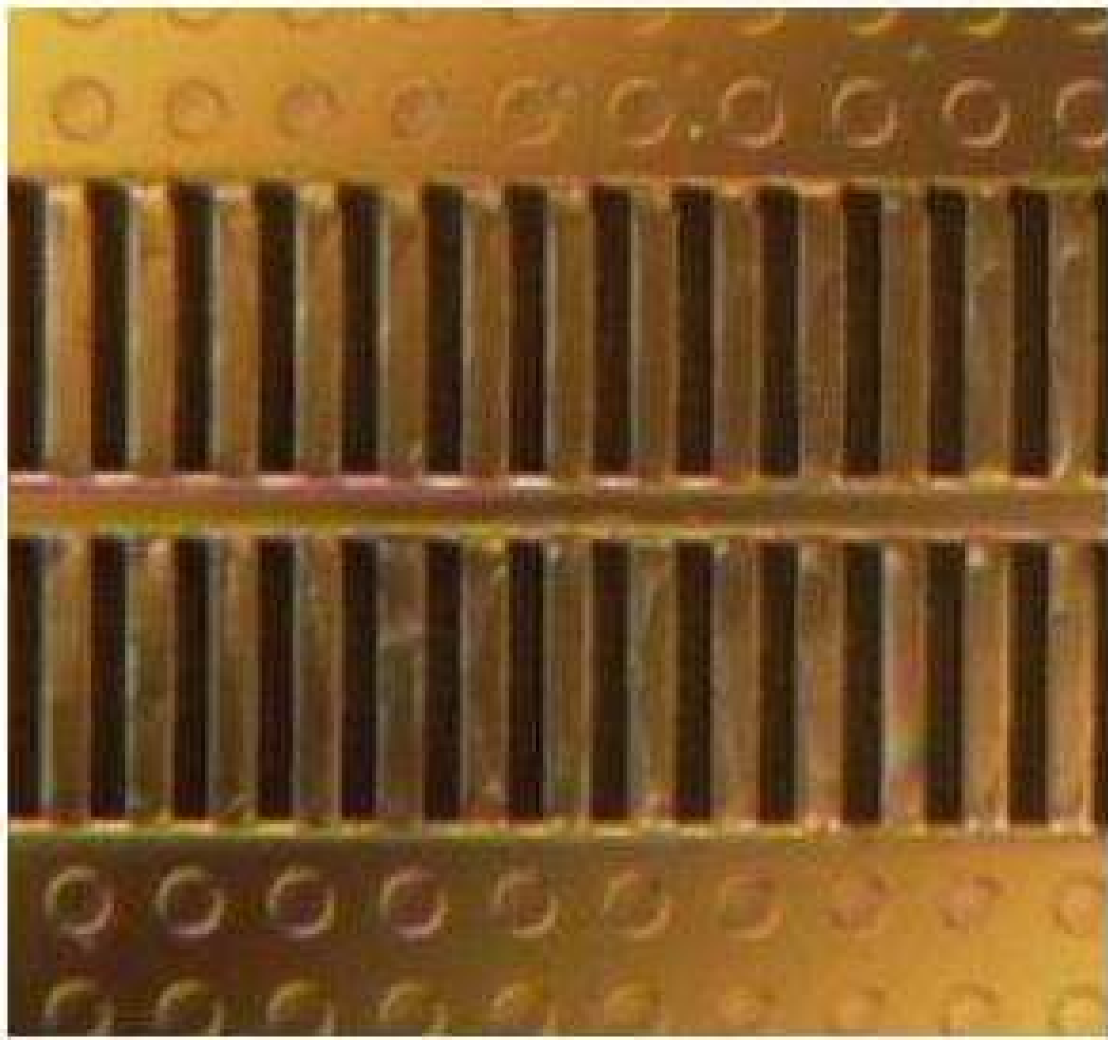

Figure 6.12: A test structure from the same wafer as 6.11. Note that the channel has not been filled by the electroplating, and that the gold is not removed from the channel.

Knowing that we would not send magnetic beads through the teststructures we did not remove the gold from them, since this takes time when designing the masks. This means that when we are exposing the resist, the areas with the gold reflects the incoming light, exposing the SU-8 once more. Where the gold has been removed the light passes right through the pyrex wafer without being reflected. This means the SU-8 where the gold has been removed only gets half as much exposure as the SU-8 on top of gold. This affects the SU-8 as can be seen from figure 6.13 and 6.14. Since the teststructures have much better electroplating results it follows that a redesigning of mask "#1 Gold, lift-off" from our mask set would solve this problem.

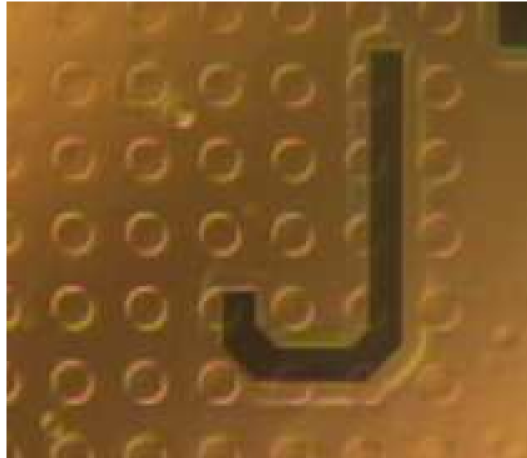

Figure 6.13: The letter J has been created by making a liftoff of the gold. Note how the SU-8 behaves differently around the letter.

Figure 6.14: The letter D has been created by making a liftoff of the gold. It is evident that where the gold has been removed there is an increased risk of unwanted electroplating

6.4.2 Hotplate

We had reason to believe that the hotplate in the cleanroom was not uniform in its heat distribution. We suspected this since in the 3-week course we had wafers placed on the

hotplate as shown in figure 6.15. On the same figure is shown with red where the most severe adhesion failures occured.

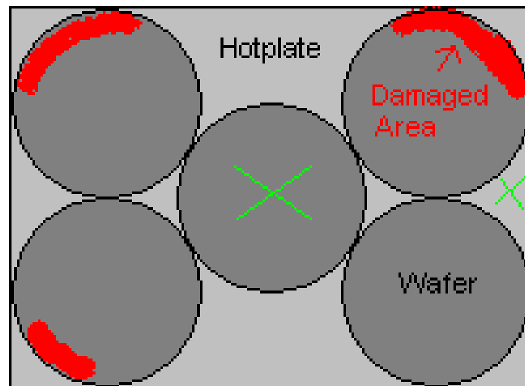

Figure 6.15: Hotplate. The darker gray circles marks where and how the wafers were positioned. The red color shows where there was massive adhesion failure. The green crosses shows where the temperature was measured.

We have therefore made a temperature measurement of the hotplate. When the hotplate controls specified that the hotplate was 100°C we measured 88°C at the center cross and 72°C at the right cross. The temperature probe used is a contact probe, so the actual temperature is probably a bit higher. Noteworthy is that there is a great temperature difference between the center and the edges.

6.4.3 KS aligner

Before each exposure we measure the intensity of the UV-light to ensure that we use the correct intensity. These measurements are always performed at the center of the aligner. At one time we measured the intensity at seven points across the wafer area. The results are shown in figure 6.16. It is evident that the intensity is not uniform over the wafer. This means that structures close to the edges get much less light than the structures at the center. This can not be compensated for, but since the light intensity falls most rapidly at the edges of the wafer, it is vital to keep important structures close to the center.

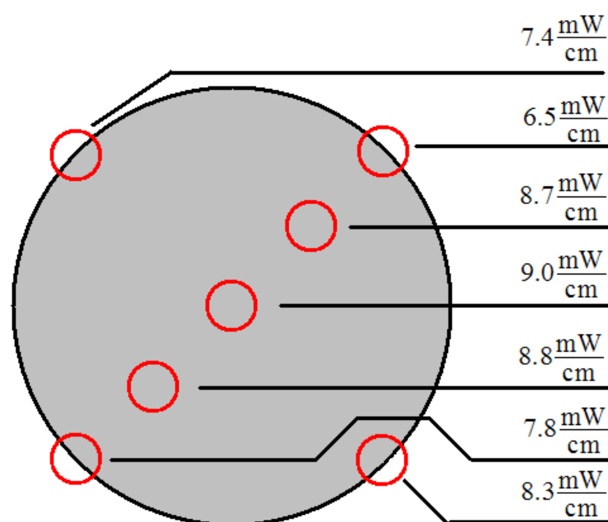

Figure 6.16: KS aligner intensity measurement. The black circles marks the wafer, and the seven red circles mark the measuring points. On the right is shown the intensity measured. The intensity distribution is not uniform over the wafer area.

6.4.4 Height measurement of SU-8

When the electroplating created a higher metal layer than the SU-8 mould structures we decided to examine if the SU-8 mould was actually 50 μm. At first the machine we needed was out of order so we took one of the pull test chips from the SU-8 tests, placed it vertically and made a visuel measurement by comparing the height of the SU-8 to the known thickness of the Pyrex wafer. This resulted in an estimate between 30 and 35 μm. Later we used a Dektak machine, which is a height profiler. We measured the height of the thin SU-8 three places on wafer and the height was between 0.6 μm and 0.7 μm instead of the expected 2 μm. We measured the thick SU-8 to be 33 μm, instead of the expected 50 μm but in accordance with our visual estimate. The height of the SU-8 is controlled by the viscosity of the SU-8 solution and the spinning speed during deposition. When using SU-8 2050, and spinning at 3000 RPM for 30 sec using the recomended parameters from [2] the height should be 50 μm, again according to [2]. It is now clear that this is not so simple. We therefore recommend always measuring the height of deposited SU-8 until correct spin parameters are found. To compensate for this a thicker SU-8 such as SU-8 2005 should be used for the thin layer or the spin time should be reduced. For the thick layer the height problem can be solved by spinning at a lower speed, such as 2000 RPM or 2500 RPM instead of 3000 RPM.

6.5 Summary

We have found that allthough the new mask design and process sequence seems to be better than the previous, it is still not perfect. There are problems with the SU-8 layers being too thin, but this can be solved by using thicker SU-8 and/or slower spinning speed during deposition. The mask for the gold lift-off should be redesigned so that the gold is not removed from the channels, since this gives better electroplating results. We have found that the electroplating deposits material at too high a rate, which can be solved by decreasing the time in the plating bath. Furthermore the composition of the NiFe alloy is not completly Permalloy, and more tests run should be made to find the right current densities. The ring included on the new mask design results in better electroplating stability. We have found that the hotplate heat distribution is not uniform, and the temperature is too low at the edges. We have compensated for this by increasing the temperature in the center and only placing four wafers instead of five wafers on the hotplate at a time, removing the center wafer. We also found that the light distribution from the KS-aligner was not uniform, the intensity decreasing rapidly af the edges.

Chapter 7

Conclusion

In the present report we have investigated magnetophoretic microfluidic systems. We have split the work in two main parts:

Theory and Simulation The simulation part contains theoretical studies and actual simulations of the systems using the software packages "FEMLAB" and "Matematica".

Fabrication and Process optimization The fabrication part contains information about the microfabrication processes and –parameters needed to fabricate the systems.

In the following we sum up the conclusions from these two parts.

7.1 Theory and Simulation

We have investigated two different models describing the magnetophoretic microfluidic systems. The first model includes only magnetic effects to give a simple model for the systems. The second model includes both magnetic effects aswell as fluidic effects to give a more precise model. The simulations aim to uncover the behaviour of the systems. We have concentrated on a strait channel with magnetizable elements placed along the sides of the channel. We investigate three different configurations:

- *Double sided* design with magnetic elements on both sides of the channel.
  - *Symmetric*, where the structures are situated exactly opposite each other.
  - *Asymmetric*, where the structures are displaced to the greatest extend in respect to each other.
- *Single sided* design with magnetic elements only on one side of the channel.

The width of the elements and the interspacing between the elements are varied in the simulations in order to determine the "best" system designs in each model. To determine which designs are best, we obviously need a way to compare two different designs, i.e.

we need a measure of quality. In each model we define such a quality measure, and by carrying out simulations of the various system designs, we get the following results

First model:

Double sided symmetric is optimized at element width 50 μm and element interspacing 650 μm.

Double sided asymmetric is optimized at element width 50 μm and element interspacing 350 μm.

Single sided is optimized at element width 50 μm and element interspacing 450 μm.

Second model:

Double sided symmetric is optimized at element width 50 μm and element interspacing 650 μm.

Double sided asymmetric is optimized at element width 50 μm and element interspacing 450 μm.

In the first model, we find that the optimal double sided asymmetric design is better than the optimal double sided symmetric design. Whereas in the second model the optimal double sided symmetric design is better than the optimal double sided asymmetric design. It is worth noting that the optimum for the double sided symmetric design occurs at the same element interspacing for both models. The optimum for the double sided asymmetric design occurs almost at the same element interspacing.

The measures of quality for the two models yield the same result for the double sided symmetric designs. Likewise for the double sided asymmetric designs. It seem though that it is *not* possible to compare a symmetric design with an asymmetric design even though the same measure of quality is used in both situations.

It would therefore be of value to develop a different measure of quality that could make it possible to compare the symmetric designs directly with the asymmetric designs.

Finally we have found that we need a force in the order 10^{-10}-10^{-9}N to capture a decent amount of beads on a micro chip unaffected by the gravity.

7.2 Fabrication and Process optimization

During our project we have developed two different mask sets. The first is the SU-8 Test Mask, a mask specially tailored to determining process parameters for new fabrication sequenses. We have succesfully used this mask design to determine optimal process parameters such as exposure time, baking time and development time. We have found that rounding corners helps increase the adhesion, as well as reducing the size of the structures as much as possible, however we have also found the optimizing the parameters lessons the impact of sharp edges and large structures. We have found that when working with SU-8 it is important to optimize the parameters for the application, especially the exposure dose.

We have concluded that many of the parameters used in our 3-week course were far from the optimal parameters. The exposure dose has been reduced by a factor of 3, and the baking time by a factor of 9. Pull tests have been made, and however not quite succesfull seems worthy for further study and experiments. Finally we have found that plasma ashing is preferable to using the 250°C oven for dehydrating the wafers.

We have developed alternatives to the original SU-8 channel structures, and found these superior to the original design

We have created a mask for a Magnetophoretic chip design and process a sequence hoping to fabricate the systems found in our simulations. Allthough the actual fabrication was not succesfull, we have performed process tests and through them found both mask, design and equipment flaws and have found ways to solve these problems. We have found that allthough the new mask design and process sequence seems to be better than the previous, it is still not perfect. A new mask and process design can now be made, using the experiences gained which should give a succesfull fabrication.

Chapter 8

Outlook

During our PMP we have thought of many ways to optimize our micro chip:

To the Gold/SU-8 problem we have thought of an mechanical bonding between the gold and the Su-8, but this requires that we are able to make meshable structures in either the gold or the SU-8.

Instead of having a micro fluidic channel which is 100μm in the direction of the magnetic structures and a hight of 50μm, we could turn the channel so the distance between the elements is 50μm and the hight of the channel is 100μm. In this way the beads only have to travel half the distance to where they are captured and this is with an unchanged volume flow. If it is possible to made an 100μm thick layer of SU-8 with channel structures of 50μm is unknown.

If we want the gravity not to affect the bead trajectories in the way so the beads stick to the wall places which are unwanted, we can turn our micro chip so that gravity acts anti-parallel to the direction of the velocity field and in this way only contributes with a constant.

Appendix A

Magnetizable Element

We want to find the field outside a rectangular magnetizable element placed in an external homogeneous magnetic field as shown in figure A.1. In this figure the element is drawn like an ordinary bar magnet because the element behaves as a bar magnet when subjected to an external homogeneous magnetic field.

First we want to find the magnetization, $\boldsymbol{M}_{\text{el}}$, of the element in the external field $\boldsymbol{H}_{\text{ext}}$. To this end, we need to do an approximation in order to be able to solve the problem analytically. In reality this is a three dimensional problem, where the element is a box with a cross sectional area, A_{el}, and a length, L_{el}. We need to approximate the real element by a cylinder (made of the same material as the real element) with the same cross sectional area and the same length as the real element, as shown in figure A.2.

The magnetic field, $\boldsymbol{H}_{\text{i}}$, inside the cylinder is given by:

$$\boldsymbol{H}_{\text{i}} = \boldsymbol{H}_{\text{ext}} + \boldsymbol{H}_{\text{d}} \tag{A.1}$$

$$= \boldsymbol{H}_{\text{ext}} - N_{\text{cyl}}\boldsymbol{M}_{\text{cyl}} = \boldsymbol{H}_{\text{ext}} - N_{\text{cyl}}\chi_{\text{el}}\boldsymbol{H}_{\text{i}} \Longleftrightarrow \tag{A.2}$$

$$\boldsymbol{H}_{\text{i}} = \left(\frac{1}{1 + N_{\text{cyl}}\chi_{\text{el}}}\right)\boldsymbol{H}_{\text{ext}} \tag{A.3}$$

where $\boldsymbol{H}_{\text{d}}$ is the *demagnetization field*, N_{cyl} is the *demagnetization factor* for the cylinder and χ_{el} is the magnetic susceptibility for the material the element and cylinder is made of.

Now we have the magnetization of the cylinder, $\boldsymbol{M}_{\text{cyl}}$, as

$$\boldsymbol{M}_{\text{cyl}} = \chi_{\text{el}}\boldsymbol{H}_{\text{i}} = \frac{\chi_{\text{el}}}{1 + N_{\text{cyl}}\chi_{\text{el}}}\boldsymbol{H}_{\text{ext}}. \tag{A.4}$$

In order to calculate the field outside the cylinder, we need to find the field from the cylinder. To solve this problem, we make use of an analogy between magnetostatics and electrostatics. In electrostatics we can easily find the field from two *electrical charges* a certain distance apart. We want to solve the magnetostatic problem we have by solving the corresponding electrostatic problem and then do symbol substitution. In order to do this we use the method of *magnetic charges* or *magnetic monopoles*[1]. So we approximate the cylinder with just two point charges a distance L_{el} apart as seen in figure A.3.

[1] Of course magnetic charges or magnetic monopoles *do not* exist, but is a useful concept to us in this

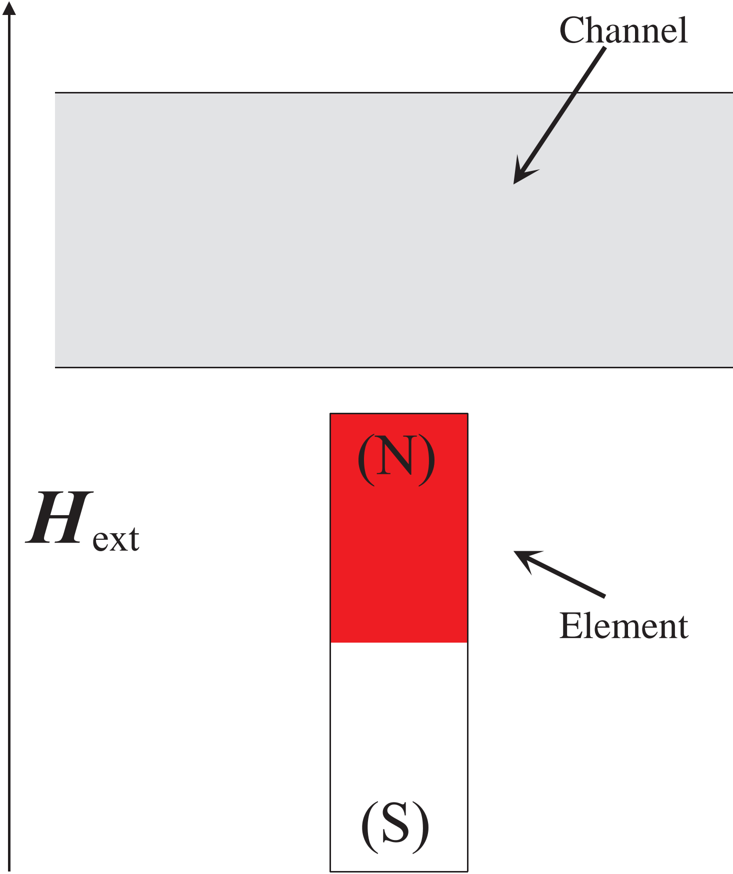

Figure A.1: Sketch of the problem to be solved: A rectangular element subjected to an external homogeneous magnetic field. In this situation the element will behave as an ordinary bar magnet.

The size, q_m, of the magnetic charges is given by

$$q_\mathrm{m} = A_\mathrm{el} \mid \boldsymbol{M}_\mathrm{cyl} \mid \tag{A.5}$$

$$= A_\mathrm{el} \frac{\chi_\mathrm{el}}{1 + N_\mathrm{cyl}\chi_\mathrm{el}} H_\mathrm{ext} \tag{A.6}$$

The electrostatic problem sketched in figure A.4 is now solved. We only aim to find the electric field, $\boldsymbol{E}$, as a function of y (i.e. on the y-axis):

---

situation. In electrostatics there exist monopoles. In classical electromagnetism, the solutions to many magnetostatic problems are very similar to the solutions for the corresponding electrostatic problems. Sometimes the electrostatic problems are much easier to solve than the corresponding magnetostatic problems. Because of this similarity, one can often *approximate* the solution to a magnetostatic problem with the solution to the corresponding electrostatic problem, using appropriate symbol substitutions

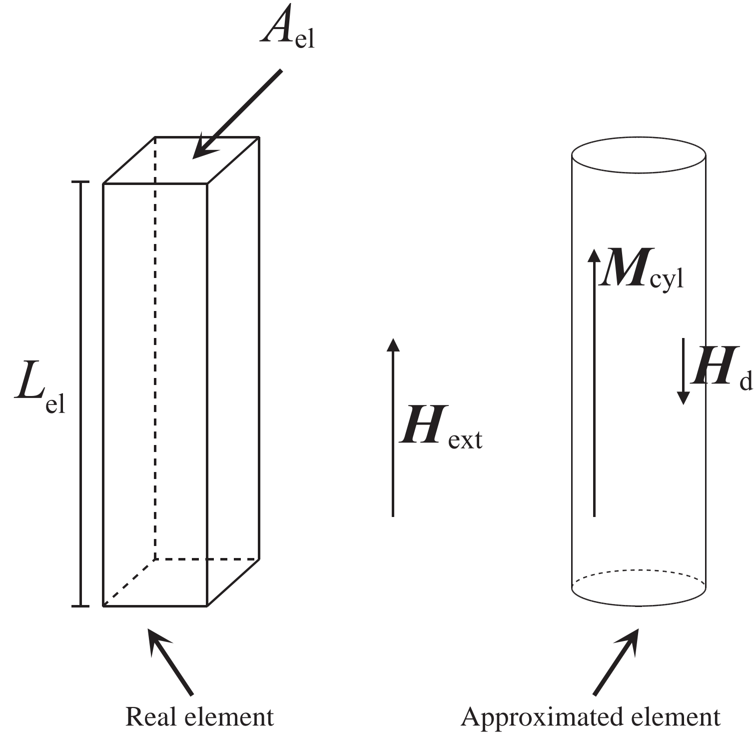

Figure A.2: The real element is a three dimensional box with length L_{el} and cross sectional area A_{el}. It is approximated with a cylinder having the same length and cross sectional area.

$$\boldsymbol{E}(y) = \boldsymbol{E}_{+\text{q}}(y) + \boldsymbol{E}_{\text{-q}}(y) \tag{A.7}$$

for the positive y-axis we have

$$E(y) = E_{+\text{q}} - E_{\text{-q}} = \frac{q}{4\pi\epsilon_0}\left(\frac{1}{y^2} - \frac{1}{(y+L)^2}\right) \tag{A.8}$$

To obtain the solution to the corresponding magnetostatic problem, we just do substitution of symbols:

- The size of the electric field E is exchanged with the size of the magnetic induction B.
- The electric charge q is exchanged with the magnetic charge q_{m}.
- The permitivity of free space ϵ_0 is exchanged with the reciprocal of the permeability of free space $\frac{1}{\mu_0}$.

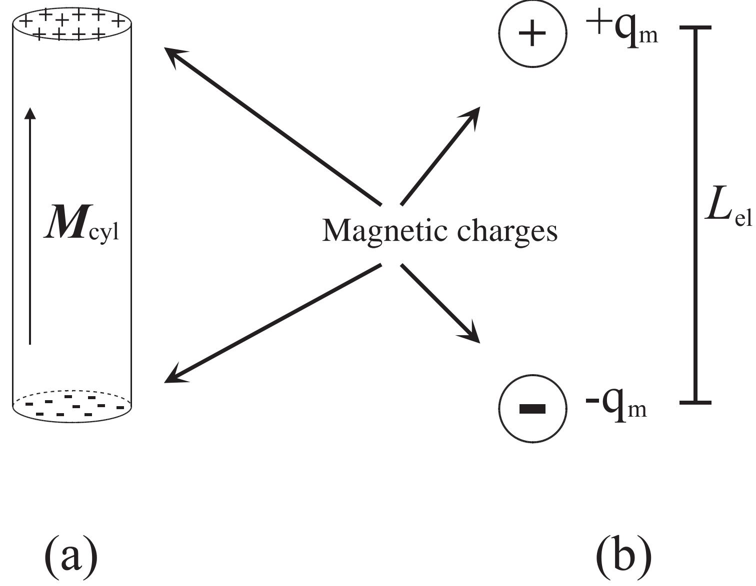

Figure A.3: In order to solve the problem, we make use of an analogy between electrostatics and magnetostatics. To this end we introduce the concept of magnetic charges. (a) Shows the cylinder with magnetic charges on the end surfaces. (b) shows the approximation consisting of just two magnetic point charges separated by a distance L_{el}.

- The separation length L is exchanged with the separation length L_{el}.

With these symbol substitutions the solution for the corresponding magnetostatic problem reads

$$B(y) = \frac{\mu_0 q_{\mathrm{m}}}{4\pi}\left(\frac{1}{y^2} - \frac{1}{(y+L_{\mathrm{el}})^2}\right) \tag{A.9}$$

From this we get the size of the $\boldsymbol{H}$-field from the element to

$$H_{\mathrm{el}}(y) = \frac{1}{\mu_0}B(y) = \frac{q_{\mathrm{m}}}{4\pi}\left(\frac{1}{y^2} - \frac{1}{(y+L_{\mathrm{el}})^2}\right) \tag{A.10}$$

The size of the total $\boldsymbol{H}$-field outside the element (on the y-axis) is thus given by

$$H_{\mathrm{tot}}(y) = H_{\mathrm{ext}}(y) + H_{\mathrm{el}}(y) \tag{A.11}$$

$$= H_{\mathrm{ext}}\left[1 + \frac{A_{\mathrm{el}}\chi_{\mathrm{el}}}{4\pi(1+N_{\mathrm{cyl}}\chi_{\mathrm{el}})}\left(\frac{1}{y^2} - \frac{1}{(y+L_{\mathrm{el}})^2}\right)\right] \tag{A.12}$$

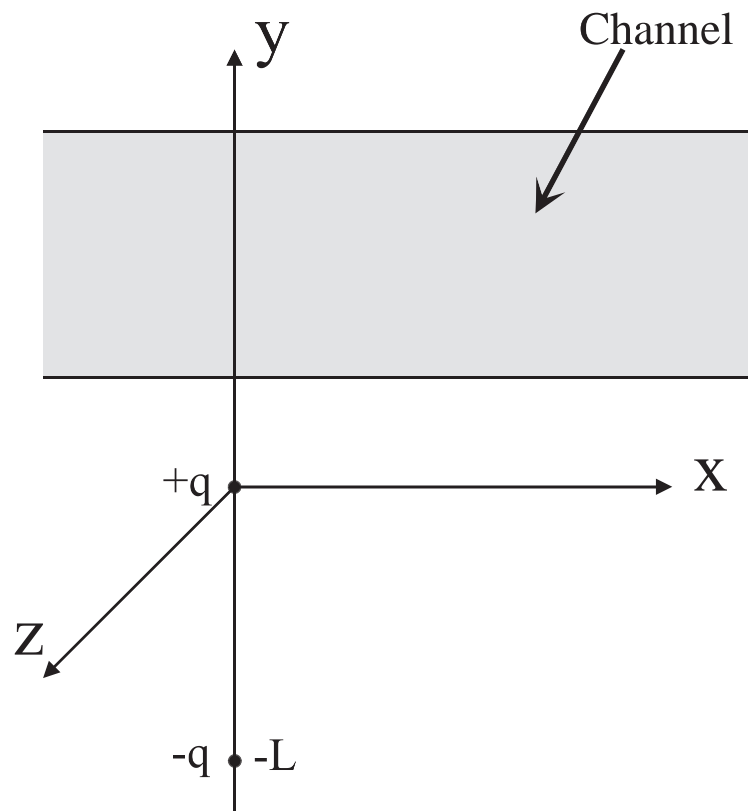

Figure A.4: The electrostatic problem we need to solve is this: Two charges are separated by a distance L, find the electric field on the positive y-axis.

Appendix B

Magnetizable sphere

We consider a solid sphere made of a soft magnetic material (which we assume to be linear) subjected to an external magnetic field. This situation is sketched in figure B.1

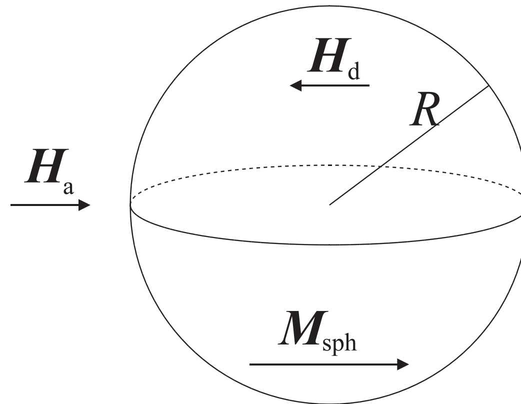

Figure B.1: Sketch of a magnetizable sphere placed in an external magnetic field.

We want to find the force, $\boldsymbol{F}_{\text{sph}}$, on the sphere from the external magnetic field $\boldsymbol{H}_{\text{a}}$. The total field, $\boldsymbol{H}_{\text{i}}$, inside the sphere is given by:

$$\boldsymbol{H}_{\text{i}} = \boldsymbol{H}_{\text{a}} + \boldsymbol{H}_{\text{d}} \tag{B.1}$$

where $\boldsymbol{H}_{\text{d}}$ is the *demagnetization field* inside the sphere and is given by

$$\boldsymbol{H}_{\text{d}} = -N_{\text{sph}}\boldsymbol{M}_{\text{sph}} \tag{B.2}$$

with N_{sph} beeing the *demagnetization factor* for the sphere and $\boldsymbol{M}_{\text{sph}}$ the magnetization of the sphere.

The magnetization of the sphere is given by $\boldsymbol{M}_{\text{sph}} = \chi_{\text{sph}}\boldsymbol{H}_{\text{i}}$ with χ_{sph} beeing the

magnetic susceptibility of the material that the sphere is made of. This way we have:

$$\boldsymbol{H}_{\mathrm{i}} = \boldsymbol{H}_{\mathrm{a}} - N_{\mathrm{sph}}\chi_{\mathrm{sph}}\boldsymbol{H}_{\mathrm{i}} \Longleftrightarrow \tag{B.3}$$

$$\boldsymbol{H}_{\mathrm{i}} = \frac{1}{1+N_{\mathrm{sph}}\chi_{\mathrm{sph}}}\boldsymbol{H}_{\mathrm{a}} \Longrightarrow \tag{B.4}$$

$$H_{\mathrm{i}} = \frac{1}{1+N_{\mathrm{sph}}\chi_{\mathrm{sph}}}H_{\mathrm{a}} \tag{B.5}$$

The magnitization of the sphere is thus given by

$$\boldsymbol{M}_{\mathrm{sph}} = \chi_{\mathrm{sph}}\boldsymbol{H}_{\mathrm{i}} \tag{B.6}$$

$$= \frac{\chi_{\mathrm{sph}}}{1+\chi_{\mathrm{sph}}N_{\mathrm{sph}}}\boldsymbol{H}_{\mathrm{a}} \tag{B.7}$$

$$= \frac{\mu_{\mathrm{sph}}-\mu_0}{\mu_0+N_{\mathrm{sph}}(\mu_{\mathrm{sph}}-\mu_0)}\boldsymbol{H}_{\mathrm{a}} \tag{B.8}$$

where μ_0 is the permeability of free space and μ_{sph} is the permeability of the material that the sphere is made of. This permeability is, according to classical electromagnetism, given by $\mu_{\mathrm{sph}} = \mu_0(1+\chi_{\mathrm{sph}})$.

In [4] page 40 it is seen that the demagnetization factor for a sphere is $N_{\mathrm{sph}} = \frac{1}{3}$. With this we get

$$\boldsymbol{M}_{\mathrm{sph}} = 3\frac{\mu_{\mathrm{sph}}-\mu_0}{\mu_{\mathrm{sph}}+2\mu_0}\boldsymbol{H}_{\mathrm{a}} \tag{B.9}$$

By using the magnetization, $\boldsymbol{M}_{\mathrm{sph}}$, and the volume, V_{sph}, of the sphere, we can derive the effective dipole moment, $\boldsymbol{m}_{\mathrm{sph}}$, of the sphere:

$$\boldsymbol{m}_{\mathrm{sph}} = V_{\mathrm{sph}}\boldsymbol{M}_{\mathrm{sph}} \tag{B.10}$$

$$= \frac{4}{3}\pi R^3\boldsymbol{M}_{\mathrm{sph}}$$

$$= 4\pi R^3\frac{\mu_{\mathrm{sph}}-\mu_0}{\mu_{\mathrm{sph}}+2\mu_0}\boldsymbol{H}_{\mathrm{a}} \tag{B.11}$$

Now we can simply use the expression for the force on a magnetic dipole in an external magnetic field from classical elctromagnetism, $\boldsymbol{F} = (\boldsymbol{m}\cdot\boldsymbol{\nabla})\boldsymbol{B}$, to find the force on the sphere:

$$\boldsymbol{F}_{\mathrm{sph}} = (\boldsymbol{m}_{\mathrm{sph}}\cdot\boldsymbol{\nabla})\boldsymbol{B}_{\mathrm{a}} \tag{B.12}$$

$$= \left[\left(4\pi R^3\frac{\mu_{\mathrm{sph}}-\mu_0}{\mu_{\mathrm{sph}}+2\mu_0}\boldsymbol{H}_{\mathrm{a}}\right)\cdot\boldsymbol{\nabla}\right]\mu_0\boldsymbol{H}_{\mathrm{a}} \tag{B.13}$$

$$= 2\pi\mu_0 R^3\frac{\mu_{\mathrm{sph}}-\mu_0}{\mu_{\mathrm{sph}}+2\mu_0}\boldsymbol{\nabla}\mid\boldsymbol{H}_{\mathrm{a}}\mid^2 \tag{B.14}$$

$$= 2\pi\mu_0 R^3\frac{\chi_{\mathrm{sph}}}{\chi_{\mathrm{sph}}+3}\boldsymbol{\nabla}\mid\boldsymbol{H}_{\mathrm{a}}\mid^2 \tag{B.15}$$

$$= 4\pi\mu_0 R^3\frac{\chi_{\mathrm{sph}}}{\chi_{\mathrm{sph}}+3}\boldsymbol{H}_{\mathrm{a}}\boldsymbol{\nabla}\boldsymbol{H}_{\mathrm{a}} \tag{B.16}$$

where R is the radius of the sphere.

Because there are no free currents in this problem, the curl of the $\boldsymbol{H}$-field is zero, why we can write

$$\boldsymbol{H}_{\mathrm{a}} = -\boldsymbol{\nabla} V_{\mathrm{m}} = -\begin{pmatrix} V_{\mathrm{m}x} \\ V_{\mathrm{m}y} \end{pmatrix} \tag{B.17}$$

where V_{m} is the *magnetic scalar potential*.

With this we get

$$\boldsymbol{F}_{\mathrm{sph}} = 4\pi\mu_0 R^3 \frac{\chi_{\mathrm{sph}}}{\chi_{\mathrm{sph}}+3} \begin{pmatrix} V_{\mathrm{m}x}V_{\mathrm{m}xx} + V_{\mathrm{m}y}V_{\mathrm{m}yx} \\ V_{\mathrm{m}x}V_{\mathrm{m}xy} + V_{\mathrm{m}y}V_{\mathrm{m}yy} \end{pmatrix} \tag{B.18}$$

where we denote $\frac{\partial}{\partial x}V_{\mathrm{m}x}$ by $V_{\mathrm{m}xx}$ and so forth.

Equation (B.18) is valid in two dimensions.

Appendix C

Fluid Theory

The Navier-Stokes equation reads

$$\rho\Big(\frac{\partial}{\partial t} + (\boldsymbol{u}\cdot\boldsymbol{\nabla})\Big)\boldsymbol{u} = -\boldsymbol{\nabla}p + \eta\nabla^2\boldsymbol{u}, \tag{C.1}$$

where ρ is the density of the fluid, η is the viscoity of the fluid. and the continuity equation:

$$\frac{\partial\rho}{\partial t} = -\boldsymbol{\nabla}\cdot(\rho\boldsymbol{u}). \tag{C.2}$$

For an incompressible fluid $\boldsymbol{\nabla}\cdot\boldsymbol{u} = 0$.

C.1 Two planes

For a flow between two infinte parallel plates seperated by a distance of h a presure only depended by the x-coordinate. We have then $\boldsymbol{u} = (u_{\mathrm{x}}(x,y,z),0,0)$ and for a incompressible fluid

$$\boldsymbol{\nabla}\cdot\boldsymbol{u} = \frac{\partial u_{\mathrm{x}}}{\partial x} + \frac{\partial u_{\mathrm{y}}}{\partial y} + \frac{\partial u_{\mathrm{z}}}{\partial z} = 0, \tag{C.3}$$

since $u_{\mathrm{y}} = 0$ and $u_{\mathrm{z}} = 0$ must $u_{\mathrm{x}} = u_{\mathrm{x}}(y,z)$. Then

$$(\boldsymbol{u}\cdot\boldsymbol{\nabla})\boldsymbol{u} = u_{\mathrm{x}}\frac{\partial}{\partial x}(u_{\mathrm{x}}(y,z),0,0) = 0. \tag{C.4}$$

For a steady flow the Navier Stokes equation is

$$0 = -\boldsymbol{\nabla}p + \eta\nabla^2\boldsymbol{u} \tag{C.5}$$

$\boldsymbol{\nabla}p = -\frac{\Delta p}{L}$ and since we have translation in z $u_{\mathrm{x}} = u_{\mathrm{x}}(y)$ Navier-stokes equation is now

$$\frac{\mathrm{d}^2u_{\mathrm{x}}(y)}{\mathrm{d}y^2} = -\frac{\Delta p}{\eta\,L}, \tag{C.6}$$

which gives

$$u_{\mathrm{x}}(y) = -\frac{1}{2}\frac{\Delta p}{\eta\, L}y^2 + c_1 y + c_2. \tag{C.7}$$

If the plates are located at $y = 0$ and $y = h$ then

$$c_1 = \frac{1}{2}\frac{\Delta p}{\eta\, L}h \quad \text{and} \quad c_2 = 0. \tag{C.8}$$

This gives the velocity profile $u_{\mathrm{x}}(y)$

$$u_{\mathrm{x}}(y) = \frac{1}{2}\frac{\Delta p}{\eta\, L}y(h - y) \tag{C.9}$$

C.1.1 The volume flow

$$Q = \frac{1}{2}\frac{\Delta p}{\eta\, L}\int_0^w \int_0^h y(h-y)\,\mathrm{d}y\mathrm{d}z = \frac{1}{12}\frac{\Delta p}{\eta\, L}wh^3 \tag{C.10}$$

C.2 Flow structure through a square cross-section

The solution to a square cross-section channel of width w and hight h must be of

$$u_{\mathrm{x}}(y,z) = \sum_{n=1}^{\infty}\sum_{m=1}^{\infty} u_{\mathrm{nm}} \sin\left(n\pi\frac{y}{w}\right)\sin\left(m\pi\frac{z}{h}\right) \tag{C.11}$$

where u_{nm} is a unknown constant.

$$\nabla^2 u_{\mathrm{x}}(y,z) = -\frac{\Delta p}{\eta L} \tag{C.12}$$

Since we expect a dobbel sum of sinus functions, we fourier transform the constant 1.

$$\sum_{k=1}^{\infty} a_k \sin\left(k\pi\frac{y}{w}\right) \tag{C.13}$$

By multiplication of $\sin\left(n\pi\frac{y}{w}\right)$ and a integration of y from 0 to w we get:

$$\int_o^w \sin\left(n\pi\frac{y}{w}\right)\sum_{k=1}^{\infty}\sin\left(k\pi\frac{y}{w}\right)\mathrm{d}y = \int_o^w \sin\left(n\pi\frac{y}{w}\right)\mathrm{d}y \tag{C.14}$$

The ortogonalitets theorem is used:

$$a_n\int_o^w \sin^2\left(n\pi\frac{y}{w}\right)\mathrm{d}y = \int_o^w \sin\left(n\pi\frac{y}{w}\right)\mathrm{d}y \tag{C.15}$$

and so we get

$$a_n = \frac{2}{n\pi}\left(1-(-1)^n\right) = \begin{cases} 0 & \text{for} \quad n = 2,4,6,... \\ \frac{4}{\pi}\frac{1}{n} & \text{for} \quad n = 1,3,5,... \end{cases} \tag{C.16}$$

We then solve the left side of the Navier-Stokes equation

$$\sum_{n=1}^{\infty}\sum_{m=1}^{\infty} u_{nm}\nabla^2 \sin\left(n\pi\frac{y}{w}\right)\sin\left(m\pi\frac{z}{h}\right) \tag{C.17}$$

$$= -\pi^2\sum_{n=1}^{\infty}\sum_{m=1}^{\infty} u_{nm}\left(\frac{n^2}{h^2}+\frac{m^2}{w^2}\right)\sin\left(n\pi\frac{y}{w}\right)\sin\left(m\pi\frac{z}{h}\right) \tag{C.18}$$

and the right side of the Navier-Stokes equation

$$-\frac{\Delta p}{\eta\, L}\sum_{\text{odd } n}^{\infty}\frac{4}{\pi}\frac{1}{n}\sin\left(n\pi\frac{y}{w}\right)\sum_{\text{odd } m}^{\infty}\frac{4}{\pi}\frac{1}{m}\sin\left(m\pi\frac{z}{h}\right) \tag{C.19}$$

$$= -\frac{\Delta p}{\eta\, L}\frac{16}{\pi^4}\sum_{\text{odd } n}^{\infty}\sum_{\text{odd } m}^{\infty}\frac{1}{nm}\sin\left(n\pi\frac{y}{w}\right)\sin\left(m\pi\frac{z}{h}\right) \tag{C.20}$$

We see that

$$u_{nm} = \frac{\Delta p}{\eta\, L}\frac{16}{\pi^4}\frac{1}{nm}\frac{1}{nm\left(\frac{n^2}{h^2}+\frac{m^2}{w^2}\right)} \tag{C.21}$$

Now the solution to the Navier-Stokes equation for a sqaure cross-section is

$$u(y,z) = \frac{\Delta p}{\eta\, L}\frac{16}{\pi^4}\sum_{\text{odd } n}^{\infty}\sum_{\text{odd } m}^{\infty}\frac{1}{nm\left(\frac{n^2}{h^2}+\frac{m^2}{w^2}\right)}\sin\left(n\pi\frac{y}{h}\right)\sin\left(m\pi\frac{z}{w}\right) \tag{C.22}$$

Appendix D

Cleanroom Processes

This chapter describes in more detail the principles of the methods used during our fabrication. This is a rewritten chapter taken from our own 3 week report made in January 2004.

D.1 Photo Lithography

Photolithography is the process of transferring a pattern from a template to a substrate by use of light. Basically a pattern is created on a piece of glass, called a *mask*. The mask is placed in close proximity (some micrometer) to the substrate on which a light sensitive solution called *photo resist* has been deposited. Light is shone through the mask transferring the pattern from the mask onto the resist on the substrate. If a *negative photo resist* is used, the unexposed resist can be washed away in a *developer* leaving only the exposed patterned resist. If a *positive photo resist* is used, the exposed resist can be washed off in the developer, leaving just the unexposed patterned resist on the substrate. The mask can then be reused on multiple substrates, and once the mask has been created the transfer of pattern to substrates is very fast. Often the light used is ultra violet (UV) light since the wavelength of the light limits the resolution, i.e. smaller wavelengths give better resolution.

Spinning

The photo resist is deposited on the substrate using *spinning*. Spinning is a technique where the substrate, in this case a wafer, is set in rotation and the resist is poured onto the rotating substrate. In this way it is possible to obtain a fairly homogeneous layer of photo resist on the substrate and the thickness of the deposited layer can be controlled quite good. To spin photo resist on our wafer we use a special machine, called a *spinner*, which has programs optimized for given resist thicknesses.

When the photo resist has been spun on, it is *soft baked*. This is a mild heat treatment used to evaporate solvent residues from the photo resist, so that it turns into a solid layer.

Mask Modes

The distance between the mask and the photo resist during exposure has huge influence on the final result. There are generally three different methods, *contact* (soft or hard), *proximity* and *projection*.

Contact gives the most precise transfer of the pattern on the mask to the photo resist. The harder the contact between the mask and the substrate with photo resist, the more precise the transfer. But a hard contact also increases the wear of the mask. In order to avoid hard wear of the mask, one can use soft contact. In soft contact the mask and the substrate (with photo resist) are still in contact, but only held together by a light pressure.

Proximity is a method where the mask is placed in close proximity to the substrate, but without touching it. In this way the wear of the mask is minimal, and the precision of the transfer only suffers slightly.

Projection is used to project the pattern from the mask through lenses onto the photo resist on the substrate, such that the feature size can be reduced. It is possible to obtain a decrease of 1:10 with this method. It requires a huge and expensive setup though and is therefore not common.

Exposure and development

Depending on what kind of structure (e.g. metal or channels) we wish to have, different kinds of photo resists will be used. Related to these different photo resists are special exposure times and development chemicals.

There are many kinds of photo resist. One of the photo resists used at MIC is a *reversible* photo resist called *AZ5214E* that is positive but can be reversed to negative. In general this resist is used positive for etching and negative for deposition of another material e.g. a metal.

Etching and depositing can be done since it is possible to treat the whole substrate affecting *only* the unprotected (uncovered) areas. After the desired treatment the photo resist can simply be removed when it is no longer needed.

Another type of photo resist often used at MIC are the epoxy based negative resists from the *SU-8 2000* series developed by MicroChem. These resists are sensitive to near UV radiation. They are normally used to micro fluid system or as a mould for high aspect ratio electro plating. With the SU-8 2000 resists we can spin on layers from 1 μm to 200 μm thick, if we can either vary the amount of solvent or the rotation speed. An example of an epoxy is SU-8 2050, where the “50” referes to a thickness of 50 μm if used with a rotation speed of 3000 rpm. With this epoxy we can vary the thickness of the layer by changing the rotation speed.

Cleaning of wafers

Before we can use the wafers they have to undergo two cleaning processes. First a water-soap cleaning process, which removes dust and particles, and secondly a piranha etch, which will remove metals and other pollutants:

Water-Soap The wafers are washed in an rough water flush and then polished on a special developed turntable for cleaning pyrex wafers using a special soap, Triton X100. The turntable has to be wet during the polish process. Due to handling of the wafers the last polished side of a wafer is the cleanest and will therefore be our topside.

Piranha Piranha is a rough etch process (a wet chemistry process) that has to be done in a fume hood since the reaction generates a lot of oxygen gas and toxic fumes. To make the piranha 1200 mL H_2SO_4 is mixed with 300 mL H_2O_2. The temperature increases to 80 °C, and the bath should therefore be handled with care. The oxygen and acid will remove metals and other pollutants from the wafer. The cleaning time is about 10 minutes.

D.2 Deposition of Metal

To make structures of metal on a wafer, we have to go through the following steps: A HMDS treatment, spin on photo resist, negative reverse exposure, development, metal deposition and lift off.

HMDS coating A HMDS treatment is a coating of a thin hexamethyldisilazane film, which improves the adhesion of the photo resist to the wafer. This is done since hexamethyldisilazane is a molecule with two active ends. The disilazane will bond to the oxygen in silicon oxide, this reaction, known as *silylation*, forms a strong bond to the wafer. The hexamethyl end will bond to the photo resist, since both the hexamethyl and photo resist are hydrofobe.

Spin on photo resist Since we want to make a deposition of metal we use the *AZ5214E* photo resist. To spin on the photo resist we use a spinner with a standard program that spins on a layer of 1.5 μm photo resist and then gives the wafer a soft bake.

Negative Reverse Exposure To revert a reversal photo resist, the resist is first exposed through a mask, then heat treated for a short time (about two minutes), then a *flood exposure* is made. A flood exposure is a process where the entire wafer is exposed without a mask.

Development When the wafer has been flood exposed it is ready to be developed. It is immersed in a mixture of 4000 mL H_2O and 800 mL NaOH under carefull stirring for one minute.

Metal deposition We deposit metal using E-beam deposition, where an electron beam evaporates metal from a bulk, which then condenses on the wafer.

Lift off Now we have metal all over the wafer, at some places directly on the wafer, places where we wish to have metal, and on other places on top of a layer of photo resist, places where we do not wish to have metal. We can now make a *lift off process* which is a wet chemistry process. The wafer is placed in a bath of acetone that can be applied heat and ultra sound. The acetone dilute the photo resist underneath the metal layer, which can be done more efficiently when heat is added. The ultra sonic starts a vibration of the metal layer on the resist so it mechanically falls off. When all the unwanted metal is ripped off, it is important that the wafer is put directly in a water rinse and this has to be done fast since acetone evaporate fast and we therefore risk having metal flakes to stick on the wafer.

D.3 SU-8 Processing

SU-8 processing involves the following steps: Dehydration, spin on SU-8 2000, soft bake, exposure, post exposure bake and development.

Dehydration Before we can spin on SU-8 2000 on our wafer we have to make sure that there are a minimum of water molecules on the surface, since the SU-8 2000 is highly hydrophobic. The dehydration can be done in an oven or a *plasma ash*, which basically is an oxidation process using a plasma.

Spin on SU-8 2000 To spin on the SU-8 2000 we fill a standard injection tube with SU-8 2000, this is done the day before so micro bubbles can rise to the surface. The wafer is placed in the spinner and with an 'air pressure' a small amount of SU-8 2000 is placed at the centre of the wafer and the rotation of the wafer is started.

Soft bake Before we can expose the epoxy we have to soft bake the substrate to evaporate the solvent this is done on a hot plate with a special heat ramp program.

Exposure The epoxy is exposed to UV-light through a mask and the molecules in the epoxy start to crosslink.

Post Exposure Bake When the epoxy has been exposed the wafer is placed on a hot plate with a special heat ramp program so a crosslinking process continues when the temperature is increased, until we get a hard epoxy glue.

Development To dissolve the unhardened resist three wet chemistry baths are used, a *first* developer bath, a *final* developer bath and a isopropanol (IPA) bath. In the first bath most of the unhardened epoxy is dissolved, in the final bath the last unhardened epoxy is dissolved and in the IPA the development process stops. Depending on the thickness of the deposited layer the times in the baths can vary.

D.4 Electroplating

Electroplating is a method of depositing metal layers on a substrate using electrochemical processes. Basically the substrate is immersed in an aquarious solution containing ions of

the metal (or metals) of interest. Now an electrolysis process is startet with the substrate beeing one of the electrodes and a rod of a certain metal beeing the other electrode. This way (by running an electric current through the system), metal is deposited on the substrate.

The electroplating equipment we use is located in 'Institut for Produktion og Ledelse' (IPL) building 204 at DTU. For transportation of the wafers from the MIC cleanroom to IPL, we use a carrier with water, filled in the cleanroom a day before. This is done since the electroplating is a wet chemistry process in an aquarious solution and the SU-8 2000 is highly hydrophobic; we want the water down in the micro structures. As a extra bonus the water protects the wafer from dust particles when we handle it at IPL (the electroplating is not done in a cleanroom). We use a electroplating solution with Fe^{2+} and Ni^{2+} ions. Between the wafer's gold layer and a nickel element placed opposite of the wafer is applied a AC current. This AC current is constructed so that the wafer most of the time is cathode while the nickel element most of the time is anode, this should result in the deposition of a fine permalloy film only where the magnetic structures should be on the wafer. The exact composition can be found in the table D.1.

Component	Formula	Concentration [mol/L]	Amount [g/2.5 L]
Nickelsulfate-hexahydrat	$NiSO_4 \cdot 6H_2O$	0.400	262.8
Ironsulfate-hexahydrat	$FeSO_4 \cdot 7H_2O$	0.035	24.316
5-Sulphosalicyl acid	$C_7H_6O_6S$	7.636	19.091
Na laulyl sulfate	$NaC_{12}H_{25}SO_4$	0.576	1.441
Naphtalene sulphonic acid	$Na_3C_{10}H_5(SO_3)_3$	3.040	7.600
Boron acid	H_3BO_3	30.916	77.29
Natriumhydroxid	$NaOH$	3.500	8.75

Table D.1: Parameters for the electroplating bath

It is important to know the free area of the gold layer to deposit a layer with a certain thickness, the ideal area has to be around $2\,\mathrm{dm}^2$. With the following formula we can calculate the thickness of the deposition layer, as if we only electroplate with Ni:

$$X_{Ni} = t\,\theta \frac{I\,M}{z\,F\,A\,\delta} \tag{D.1}$$

Where t is the deposition time, θ is the efficiency, I is the current, M is the molar mass, z is the number of free electrons, F is Faraday's number, A is the area and δ is the density. This gives a good idea of the thickness we will get in a certain time.

Appendix E

Additional test structures on the SU-8 tests mask

E.0.1 Magnetic structures

For our project design, we also need to incorporate elongated holes to be used as a mould for the electroplating of the magnetic structures. It is important that these structures are developed completly to ensure uniform electroplating. However by overdeveloping the risk of adhesion failure increases. We would like to test the adhesion of these structures, as well as the development time, versus the thickness and shape of the holes. We have therefore made different structures with different holes and sizes, which can be seen on figure refElementer. These structures have been made twice on the mask, one twice as large as the other. At present our calculations predict that we only need the small one's, but it would be nice to know if the larger versions are manufacturable.

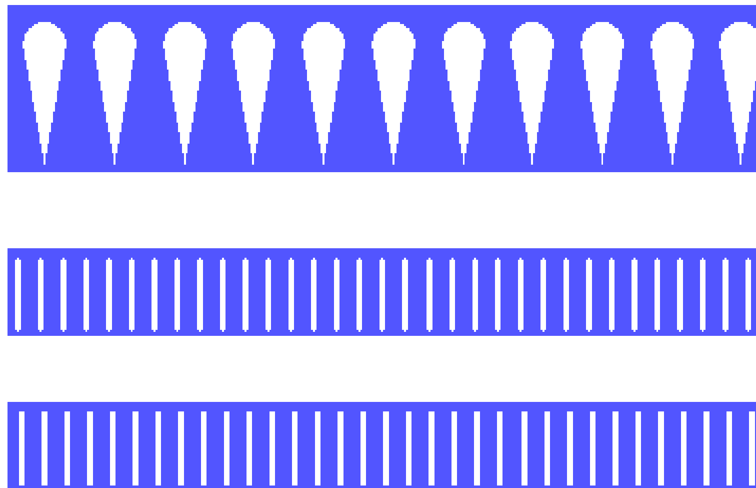

Figure E.1: Part of the electroplating mould structures.

E.0.2 Edge angle testing devices

The next thing we wished to test was how the adhesion was affected by the angle at the corners of the structure. Based on our previous microscopic investigations of the first wafers, we believe it is important, to avoid sharp edges where the stress is maximized locally. This is tested in the following droplets shown on figure E.2.

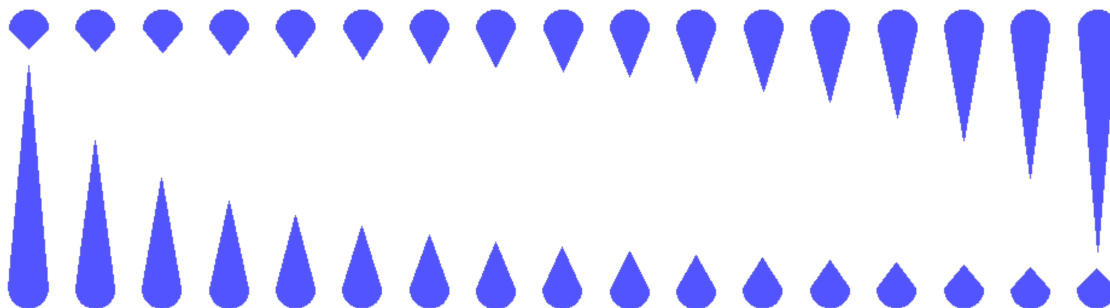

Figure E.2: Angle testing devices

These droplets are meant to test the stress related to sharp corners, but we wished to ensure that any adhesion failure would be at the sharp angle, and thus used a circular shape in the other end. The angle is varied from 10°to 90°. Note that due to space limitations on the mask design only one size of this structure was incorporated in the final design. It could be interesting in a new design to also vary the size.

Appendix F

Detailed process sequense for SU-8 test batches

F.1 First batch of SU-8 2002 for visuel inspection

1. Cleaning
   Equipment: Grammophon, Triton X-100 soap, Piranha
   The wafers are washed on both sides. The last side washed is the cleanest and is the one used for processing. The wafers are immersed in Piranha for 10 min followed by a 5 min rinse in DI-water.

2. Metal deposition
   Equipment: Leybold

Pressure	Ti	Au
1×10^{-9} Bar	300 Å	1000 Å

3. Plasma ash cleaning
   Equipment: Plasma Asher
   Recipe:

Flow O_2	Flow N_2	Power	Time
440 ml/min	40 ml/min	200 W	5 min

4. SU-8 2002 Deposition
   Equipment: KSF Spinner, SU-8 2002, Syringe
   Recipe:

Step	Acceleration (RPM/s)	End speed (RPM)	Hold time (s)
1	100	500	5
2	300	3000	30
3	-1000	0	5

5. Soft bake
   Equipment: Programmable hotplate
   Recipe:

Step	Ramp (min)	Temp (°C)	Hold (min)
1	2	65	2
2	2	95	2
3	45	17	180

After using the hotplate we discovered large amounts of SU-8 on the backside of the wafer. This had been sucked under the wafer during the spinning process, but was only discovered now. The SU-8 on the backside was removed using a clean room wipe with acetone. This is however a messy process generating many particles on the top side of the wafer.

6. SU-8 2002 exposure

   Equipment: Karl Süss Aligner, Karl Suss UV intensity meter-model 1000

   Note: By using a cover, only one sixth of the wafer is exposed

   Recipe:

Mask	Exposure Filter	Exposure Type	Lamp intensity
SU-8 Test Mask	365nm I-line filter	Constant intensity	8.9 $\frac{mW}{cm}$

   Exposure Times[1]:

Wafers	Time 1	Time 2	Time 3	Time 4	Time 5	Time 6
1+2	10 s (1x10 s)	25 s (1x25 s)	40 s (2x20 s)	50 s (2x25 s)	60 s (2x30 s)	75 s (3x25 s)
3+4	90 s (3x30 s)	104 s (4x26 s)	120 s (4x30s)	135 s (5x27 s)	150 s (5x30 s)	175 s (7x25 s)

7. Post exposure bake

   Equipment: Programmable hotplate

   Recipe:

Step	Ramp (min)	Temp (°C)	Hold (min)
1	2	65	2
2	2	100	5
3	45	15	180

8. Development

   Equipment: 3 magnetic stirrers, Fumehood, Beaker

   Recipe:

Step	Equipment	Time
1	Developer First	5 min
2	Developer Second	5 min
3	IPA	2 min
4	N_2 Gun Blow dry	30 sec
5	Dry free hanging	10 min

[1] Wait time between multiple exposures is always 30s

F.2 First batch of SU-8 2050 for visuel inspection

1. Cleaning:
   Equipment: Grammophon, Triton X-100 soap, Piranha
   The wafers are washed on both sides. The last side washed is the cleanest and is the one used for processing. The wafers are immersed in Piranha for 10 min followed by a 5 min rinse in DI-water.

2. Metal deposition:
   Equipment: Leybold

Pressure	Ti	Au
1×10^{-9} Bar	300 Å	1000 Å

3. Plasma ash cleaning:
   Equipment: Plasma Asher
   Recipe:

Flow O_2	Flow N_2	Power	Time
440 ml/min	40 ml/min	200 W	5 min

4. SU-8 2002 Deposition
   Equipment: KSF Spinner, SU-8 2002, Syringe
   Recipe:

Step	Acceleration (RPM/s)	End speed (RPM)	Hold time (s)
1	100	500	5
2	300	3000	30
3	-1000	0	5

5. Soft bake:
   Equipment: Programmable hotplate
   Recipe:

Step	Ramp (min)	Temp (°C)	Hold (min)
1	2	65	2
2	2	95	2
3	45	17	180

6. SU-8 2002 exposure:
   Equipment: Karl Süss Aligner, Karl Suss UV intensity meter-model 1000
   Recipe:

Mask	Exposure Filter	Exposure Type	Lamp intensity	Time
SU-8 Test Mask	365nm I-line filter	Constant intensity	9.0 $\frac{mW}{cm}$	25 s

7. Post exposure bake:
   Equipment: Programmable hotplate
   Recipe:

Step	Ramp (min)	Temp (°C)	Hold (min)
1	2	65	2
2	2	100	5
3	45	15	180

8. Development:
   Equipment: 3 magnetic stirrers, Fumehood, Beaker
   Recipe:

Step	Equipment	Time
1	Developer First	5 min
2	Developer Second	5 min
3	IPA	2 min
4	N_2 Gun Blow dry	30 sec
5	Dry free hanging	10 min

9. Plasma ash cleaning:
   Equipment: Plasma Asher
   Recipe:

Flow O_2	Flow N_2	Power	Time
440 ml/min	40 ml/min	200 W	5 min

10. SU-8 2050 Deposition

    Equipment: KSF Spinner, SU-8 2050, Pressure controlled syringe
    Recipe:

Step	Acceleration (RPM/s)	End speed (RPM)	Hold time (s)
1	100	500	10
2	300	3000	30
3	-1000	0	5

11. Soft bake:
    Equipment: Programmable hotplate
    Recipe:

Step	Ramp (min)	Temp (°C)	Hold (min)
1	2	65	5
2	2	100	10
3	45	15	180

12. SU-8 2050 exposure:
    Equipment: Karl Süss Aligner, Karl Suss UV intensity meter-model 1000
    Note: By using a cover, only one half of the wafer is exposed
    Recipe:

Mask	Exposure Filter	Exposure Type	Lamp intensity
SU-8 Test Mask	365nm I-line filter	Constant intensity	$8.9 \frac{mW}{cm}$

Exposure Times[2]:

Wafer	W1 Left	W1 Right	W2 Left	W2 Right	W3 Left	W3 Right	W4 Left	W4 Righ
Time	30 s (1x30 s)	60 s (2x30 s)	90 s (3x30 s)	120 s (4x30 s)	150 s (5x30 s)	200 s (8x25 s)	250 s (10x25 s)	300 s (10x30 s

13. Post exposure bake:

    Equipment: Programmable hotplate

    Recipe:

Step	Ramp (min)	Temp (°C)	Hold (min)
1	2	65	2
2	2	100	5
3	45	15	180

14. Development:

    Equipment: 3 magnetic stirrers, Fumehood, Beaker

    Recipe:

Step	Equipment	Time
1	Developer First	5 min
2	Developer Second	5 min
3	IPA	2 min
4	N_2 Gun Blow dry	30 sec
5	Dry free hanging	10 min

F.3 SU-8 2002 Test wafers Pull test

This is the process sequence that was used for the manufacturing of SU8 test wafers for the Pull test of SU-8 2002 on gold.

1. Cleaning:
   Equipment: Grammophon, Triton X-100 soap, Piranha
   The wafers are washed on both sides. The last side washed is the cleanest and is the one used for processing. The wafers are immersed in Piranha for 10 min followed by a 5 min rinse in DI-water.

2. Metal deposition:
   Equipment: Leybold

Pressure	Ti	Au
1×10^{-9} Bar	300 Å	1000 Å

3. Plasma ash cleaning:
   Equipment: Plasma Asher
   Recipe:

[2] Wait time between multiple exposures is always 30s

Flow O_2	Flow N_2	Power	Time
440 ml/min	40 ml/min	200 W	6 min

4. SU-8 2002 Deposition
   Equipment: KSF Spinner, SU-8 2002, Small plastic bottle
   Recipe:

Step	Acceleration (RPM/s)	End speed (RPM)	Hold time (s)
1	100	500	10
2	300	3000	30
3	-1000	0	5

5. Soft bake:
   Equipment: Programmable hotplate
   Recipe:

Step	Ramp (min)	Temp (°C)	Hold (min)
1	2	65	2
2	2	95	5
3	45	15	180

6. SU-8 2002 exposure:
   Equipment: Karl Süss Aligner, Karl Suss UV intensity meter-model 1000
   Recipe:

Mask	Exposure Filter	Exposure Type	Lamp intensity
SU-8 Test Mask	365nm I-line filter	Constant intensity	9.0 $\frac{mW}{cm}$

   Exposure times:

Wafer	1. Left	1. Right	2. Left	2.Right	3.Left	3.Right	4.Left	4.Right
Total (s)	10	15	20	25	25	30	35	40
As (s)	1x10	1x15	1x20	1x25	1x25	1x30	2x17.5	2x20

7. Post exposure bake:
   Equipment: Programmable hotplate
   Recipe:

Ramp (min)	Temp (°C)	Hold (min)
2	65	2
2	100	5
0	15	180

8. Development:
   Equipment: 3 magnetic stirrers, Fumehood, Beaker Recipe:

Step	Equipment	Time
1	Developer First	5 min
2	Developer Second	5 min
3	IPA	2 min
4	N_2 Gun Blow dry	30 sec
5	Dry free hanging	10 min

9. Plasma ash SU-8 monolayer removal:
   Equipment: Plasma Asher
   Recipe:

Flow O_2	Flow N_2	Power	Time
440 ml/min	40 ml/min	200 W	5 min

10. Dicing:
    The wafers are diced before the pull tests.

F.4 SU-8 2050 Test wafers Pull test

This is the process sequence that was used for the manufacturing of SU8 test wafers for the Pull test of SU-8 2050 on Su-8 2002 on gold.

1. Cleaning:
   Equipment: Grammophon, Triton X-100 soap, Piranha
   The wafers are washed on both sides. The last side washed is the cleanest and is the one used for processing. The wafers are immersed in Piranha for 10 min followed by a 5 min rinse in DI-water.

2. Metal deposition:
   Equipment: Leybold

Pressure	Ti	Au
1×10^{-9} Bar	300 Å	1000 Å

3. Plasma ash cleaning:
   Equipment: Plasma Asher
   Recipe:

Flow O_2	Flow N_2	Power	Time
440 ml/min	40 ml/min	200 W	6 min

4. SU-8 2002 Deposition
   Equipment: KSF Spinner, SU-8 2002, Small plastic bottle
   Recipe:

Step	Acceleration (RPM/s)	End speed (RPM)	Hold time (s)
1	100	500	10
2	300	3000	30
3	-1000	0	5

5. Soft bake:
   Equipment: Programmable hotplate
   Recipe:

Step	Ramp (min)	Temp (°C)	Hold (min)
1	2	65	2
2	2	95	5
3	45	15	180

6. SU-8 2002 exposure:
   Equipment: Karl Süss Aligner, Karl Suss UV intensity meter-model 1000
   Recipe:

Mask	Exposure Filter	Exposure Type	Lamp intensity	Time
SU-8 Test Mask	365nm I-line filter	Constant intensity	9.0 $\frac{mW}{cm}$	25 s

7. Post exposure bake:
   Equipment: Programmable hotplate
   Recipe:

Ramp (min)	Temp (°C)	Hold (min)
2	65	2
2	100	5
0	15	180

8. Development:
   Equipment: 3 magnetic stirrers, Fumehood, Beaker Recipe:

Step	Equipment	Time
1	Developer First	5 min
2	Developer Second	5 min
3	IPA	2 min
4	N_2 Gun Blow dry	30 sec
5	Dry free hanging	10 min

9. Plasma ash cleaning:
   Equipment: Plasma Asher
   Recipe:

Flow O_2	Flow N_2	Power	Time
440 ml/min	40 ml/min	200 W	5 min

10. SU-8 2050 Deposition
    Equipment: KSF Spinner, SU-8 2050, Pressure syringe
    Recipe:

Step	Acceleration (RPM/s)	End speed (RPM)	Hold time (s)
1	100	500	10
2	300	3000	30
3	-1000	0	5

11. Soft bake:
    Equipment: Programmable hotplate
    Recipe:

Step	Ramp (min)	Temp (°C)	Hold (min)
1	2	65	2
2	2	95	5
3	45	15	180

12. SU-8 2050 exposure:
    Equipment: Karl Süss Aligner, Karl Suss UV intensity meter-model 1000
    Recipe:

Mask	Exposure Filter	Exposure Type	Lamp intensity
SU-8 Test Mask	365nm I-line filter	Constant intensity	9.0 $\frac{mW}{cm}$

Exposure times:

Wafer	1. Left	1. Right	2. Left	2.Right	3.Left	3.Right	4.Left	4.Right
Total (s)	20	30	40	50	50	60	70	80
As (s)	1x20	1x30	2x20	2x25	2x25	2x30	3x23.3	4x20

13. Post exposure bake:
    Equipment: Programmable hotplate
    Recipe:

Ramp (min)	Temp (°C)	Hold (min)
2	65	3
2	100	7
0	15	180

14. Development:
    Equipment: 3 magnetic stirrers, Fumehood, Beaker Recipe:

Step	Equipment	Time
1	Developer First	5 min
2	Developer Second	5 min
3	IPA	2 min
4	N_2 Gun Blow dry	30 sec
5	Dry free hanging	10 min

15. Plasma ash SU-8 monolayer remowal:
    Equipment: Plasma Asher
    Recipe:

Flow O_2	Flow N_2	Power	Time
440 ml/min	40 ml/min	200 W	5 min

16. Dicing:
    The wafers are diced before the pull test.

Appendix G

Detailed process sequence for magnetophoretic chips

1. Cleaning:
   Equipment: Grammophon, Triton X-100 soap, Piranha
   The wafers are washed on both sides. The last side washed is the cleanest and is the one used for processing. The wafers are immersed in Piranha for 10 min followed by a 5 min rinse in DI-water.

2. Resist deposition:
   Equipment: KS Spinner Track 1, Photoresist AZ5214E
   Recipe: PR_1.5
   The wafers are placed in the spinner and AZ5214E. This recipe spins 1.5 μm resist on, bakes the wafers at 90 °C for 90 s, and cools off at 23 °C.

3. Exposure:
   Equipment: EVC Aligner
   Recipe:

Mask	First	Reversal Bake	Flood
#1 Gold, lift-off	7 s	2min@120°C	30 s

4. Development:
   Recipe:

Developer	Time	Temperature	Rinse DI water w. N_2
AZ5421	60s	23°C	5 min

5. Metal deposition:
   Equipment: Leybold

Pressure	Ti	Au
1×10^{-9} Bar	300 Å	1000 Å

6. Plasma ash cleaning:
   Equipment: Plasma Asher
   Recipe: Note: O_2 flow should have been 440 ml/min

Flow O_2	Flow N_2	Power	Time
220 ml/min	40 ml/min	200 W	6 min

7. SU-8 2002 Deposition
   Equipment: KSF Spinner, SU-8 2002, small plastic dispenser bottle
   Recipe:

Step	Acceleration (RPM/s)	End speed (RPM)	Hold time (s)
1	100	500	10
2	300	3000	30
3	-1000	0	5

8. Soft bake:
   Equipment: Programmable hotplate
   Recipe:

Step	Ramp (min)	Temp (°C)	Hold (min)
1	2	65	2
2	2	100	3
3	45	15	180

9. SU-8 2002 exposure:
   Equipment: Karl Süss Aligner
   Recipe: Note: The exposure time was decided from the visuel inspections of the

Mask	Exposure Filter	Exposure Type	Lamp intensity	Time
#2 SU8 Insulation/Bonding	365nm I-line filter	Constant intensity	9 $\frac{mJ}{cm}$	25 s

   ”SU-8 2002 Visuel”batch.

10. Post exposure bake:
    Equipment: Programmable hotplate
    Recipe:

11. Development:
    Equipment: 3 magnetic stirrers, Fumehood, Beaker Recipe:

Step	Ramp (min)	Temp (°C)	Hold (min)
1	2	65	2
2	2	100	5
3	45	15	180

Step	Equipment	Time
1	Developer First	5 min
2	Developer Second	5 min
3	IPA	2 min
4	N_2 Gun Blow dry	30 sec
5	Dry free hanging	10 min

12. Plasma ash cleaning:
    Equipment: Plasma Asher
    Recipe:

Flow O_2	Flow N_2	Power	Time
440 ml/min	40 ml/min	200 W	5 min

13. SU-8 2050 Deposition
    Equipment: KSF Spinner, SU-8 2050, Pressurized syringe
    Recipe:

Step	Acceleration (RPM/s)	End speed (RPM)	Hold time (s)
1	100	500	10
2	300	3000	30
3	-1000	0	5

14. Soft bake Equipment: Programmable hotplate
    Recipe:

Step	Ramp (min)	Temp (°C)	Hold (min)
1	2	60	2
2	2	100	5
3	45	15	180

15. SU-8 2050 exposure:
    Equipment: Karl Süss Aligner
    Recipe:

16. Post exposure bake Equipment: Programmable hotplate
    Recipe:

Mask	Exposure Filter	Exposure Type	Lamp intensity	Time Wafer 1+2	Time Waf
#3 SU8 Channels	365nm I-line filter	Constant intensity	9 $\frac{mJ}{cm}$	2×30 s	3×23.

Step	Ramp (min)	Temp (°C)	Hold (min)
1	2	65	5
2	2	100	10
3	45	15	180

17. Development:
    Equipment: 3 magnetic stirrers, Fumehood, Beaker Recipe:

Step	Equipment	Time
1	Developer First	5 min
2	Developer Second	5 min
3	IPA	2 min
4	N_2 Gun Blow dry	30 sec
5	Dry free hanging	10 min

18. Plasma ash SU-8 monolayer remowal:
    Equipment: Plasma Asher
    Recipe:

Flow O_2	Flow N_2	Power	Time
440 ml/min	40 ml/min	200 W	5 min

19. Electroplating
    Equipment: Electroplating Bath
    Recipe:

	Attempt 1 Wafer 3	Attempt 2 Wafer 2	Attempt 3 Wafer 1
Cycle 1: Current	0.96 A	1.92	0.96 A
Cycle 1: Duration	60 ms	60 ms	60 ms
Cycle 2: Current	-1.44 A	-2.88	-1.44 A
Cycle 2: Duration	20 ms	20 ms	20 ms
Repetions	92250	15000	30750
Total Time	2h 5m	20 m	41 m
pH before	3.58	3.44	3.49
pH after	3.60	3.48	3.56

Appendix H

Mathematica 5.0 code

In this progam code is 'widthx1' the x-position of the channel inlet and 'Nbeads' is the number of beads.

```
Pos2D = Table[{{widthx1, ((1 + 2*n)/(2*NBeads)*heigth) - widthy}}, {n,
         0, NBeads - 1}];
LastPos =
    Table[{{Pos2D[[n]][[1]][[1]], Pos2D[[n]][[1]][[2]]}}, {n, 1, NBeads}];
i = 0;
n = 0;
While[i <= K,
    If[Mod[i, TStep] == 0,
      MultipleListPlot[LastPos[[1]], LastPos[[2]], LastPos[[3]], LastPos[[4]],
         LastPos[[5]], LastPos[[6]], LastPos[[7]], LastPos[[8]], LastPos[[9]],
         LastPos[[10]], LastPos[[11]], LastPos[[12]], LastPos[[13]],
        LastPos[[14]], LastPos[[15]], LastPos[[16]], LastPos[[17]],
        LastPos[[18]], LastPos[[19]], LastPos[[20]], LastPos[[21]],
        LastPos[[22]], LastPos[[23]], LastPos[[24]], LastPos[[25]],
        LastPos[[26]], LastPos[[27]], LastPos[[2]], LastPos[[29]],
        LastPos[[30]], LastPos[[31]], LastPos[[32]], LastPos[[33]],
        LastPos[[34]], LastPos[[35]], LastPos[[36]], LastPos[[37]],
        LastPos[[38]], LastPos[[39]], LastPos[[40]], LastPos[[41]],
        LastPos[[42]], LastPos[[43]], LastPos[[44]], LastPos[[45]],
        LastPos[[46]], LastPos[[47]], LastPos[[48]], LastPos[[49]],
        LastPos[[50]], LastPos[[51]], LastPos[[52]], LastPos[[53]],
        LastPos[[54]], LastPos[[55]], LastPos[[56]], LastPos[[57]],
        LastPos[[58]], LastPos[[59]], LastPos[[60]], LastPos[[61]],
        LastPos[[62]], LastPos[[63]], LastPos[[64]], LastPos[[65]],
        LastPos[[66]], LastPos[[67]], LastPos[[68]], LastPos[[69]],
        LastPos[[70]], LastPos[[71]], LastPos[[72]], LastPos[[73]],
        LastPos[[74]], LastPos[[75]], LastPos[[76]], LastPos[[77]],
        LastPos[[78]], LastPos[[79]], LastPos[[80]], LastPos[[81]],
```

```
    LastPos[[82]], LastPos[[83]], LastPos[[84]], LastPos[[85]],
    LastPos[[86]], LastPos[[87]], LastPos[[88]], LastPos[[89]],
    LastPos[[90]], LastPos[[91]], LastPos[[92]], LastPos[[93]],
    LastPos[[94]], LastPos[[95]], LastPos[[96]], LastPos[[97]],
    LastPos[[98]], LastPos[[99]], LastPos[[100]],
    PlotLabel ->
      StyleForm["t=" <> ToString[i*t0] <> " seconds", FontSize -> 16],
    SymbolStyle -> {Hue[.1], Hue[.2], Hue[.3], Hue[.4], Hue[.5], Hue[.6],
        Hue[.7], Hue[.8], Hue[.9], Hue[1]},
    SymbolShape -> {PlotSymbol[Box, 3]},
    PlotRange -> {{widthx1, widthx2 + cont*w}, {-widthy, widthy}},
    AxesOrigin -> {widthx1, -widthy}];
  If[n >= NBeads, Break[];];
  LastPos = {};
  ];
i = i + 1;
j = 0;
n = 0;
While[j < NBeads,
  j = j + 1;
  posx = Last[Pos2D[[j]]][[1]];
  posz = Last[Pos2D[[j]]][[2]];
  calculated = 0;
  If[posx > cont*w + widthx2 || posz < widthy - heigth || posz > widthy,
    calculated = 1;
    n = n + 1;
    vxtmp = 0;
    vztmp = 0;
    ];
  If[calculated == 0,
    vxtmp =
      Fmagx2[posx, posz]/(3*Pi*Viscosity*dBeads) +
        VCF*v[.5, (posz - widthy + heigth)/heigth];
    vztmp = Fmagy2[posx, posz]/(3*Pi*Viscosity*dBeads);
    ];
  posx = posx + vxtmp*t0;
  posz = posz + vztmp*t0;
  AppendTo[Pos2D[[j]], {posx, posz}];
  If[Mod[i, TStep] == 0,
    AppendTo[LastPos, {{posx, posz}}]
    ];
  ];
];
```

Bibliography

[1] Microchem, NANO^{TM} Negative Tone Photoresist Formulations 2002-2025, http://www.microchem.com/products/pdf/SU8_ 2002-2025.pdf

[2] Microchem, NANO^{TM} Negative Tone Photoresist Formulations 2035-2100, http://www.microchem.com/products/pdf/SU8_ 2035-2100.pdf

[3] M. Shaw, D. Nawrocki, R. Hurditch and D. Johnson: *Improving the Process Capability of SU-8*, Microchem Corp. www.microchem.com

[4] Robert C. O'Handley: *Modern Magnetic Materials, Principles and Applications*. John Wiley & Sons, Inc. 2000.

[5] Benny Lautrup: *Physics of Continuous Matter, Exotic and everyday phenomena in the macroscopic world*, The Niels Bohr Institute, Copenhagen, Denmark. January 22 2004

[6] Kristian Smistrup: *Integrated Micromachined Magnetic Bead Seperator*, MIC, Lyngby, Denmark, December 2003